

# X-ray Spectroscopy of the O Supergiant $\zeta$ Puppis Indicates Surprising Variation in the Wind Mass-loss Rate on Years Timescales

A THESIS PRESENTED  
BY  
JIAMING WANG  
TO  
THE DEPARTMENT OF PHYSICS AND ASTRONOMY  
  
IN PARTIAL FULFILLMENT OF THE REQUIREMENTS  
FOR THE DEGREE OF  
BACHELOR OF ARTS  
IN THE SUBJECT OF  
ASTROPHYSICS  
  
SWARTHMORE COLLEGE  
SWARTHMORE, PENNSYLVANIA  
MAY F2022

# X-ray Spectroscopy of the O Supergiant $\zeta$ Puppis Indicates Surprising Variation in the Wind Mass-loss Rate on Years Timescales

## ABSTRACT

We apply two mass-loss rate diagnostics described in the thesis on *Chandra* and *XMM-Newton* X-ray spectroscopic measurements of  $\zeta$  Pup, one of the most luminous stars in the Milky Way and one of the closest O stars to Earth. Emission line profile analysis from new long *Chandra* grating observations taken during 2018 and 2019 indicates a significant 40% increase in  $\zeta$  Pup's wind mass-loss rate as compared to data taken in *Chandra*'s first observation cycle in 2000. Broadband spectral modeling of 20 years of *XMM* observations also reveal non-periodic wind mass-loss rate variation at a 40% level on timescales of months to years. These results are surprising as the mass-loss rates of massive stars are predicted to be constant.

# Contents

o	INTRODUCTION	I
o.o	Overview . . . . .	I
o.o	The Wind of $\zeta$ Puppis . . . . .	4
o.o	X-ray Formation in the Winds . . . . .	9
i	EMISSION LINE ANALYSIS OF THE MASS-LOSS RATE OF $\zeta$ PUPPIS	21
i.i	Introduction . . . . .	21
i.2	Modeling the Emission Lines . . . . .	23
i.3	Observations and Data . . . . .	33
i.4	Model Fitting . . . . .	35
i.5	Results . . . . .	42
i.6	Discussion . . . . .	42
2	TIME VARIABILITY ANALYSIS OF THE <i>XMM</i> OBSERVATIONS	49
2.1	Introduction . . . . .	49
2.2	Observations and Data . . . . .	50
2.3	Flux Integration . . . . .	53
2.4	Statistics and Period Search Results . . . . .	57
2.5	Discussion and Conclusions . . . . .	60
3	BROADBAND SPECTRAL MODELING OF 20 YEARS OF <i>XMM</i> OBSERVATIONS	64
3.1	Introduction . . . . .	64
3.2	The Models . . . . .	65
3.3	Grouping and Fitting the Data . . . . .	77
3.4	Results . . . . .	80
3.5	Discussion and Conclusions . . . . .	85
4	CONCLUSIONS	90
4.1	Results . . . . .	90

4.2 Discussion . . . . . 92

REFERENCES 100

# Listing of figures

- 1 A radial slice of a radiation-driven wind from the 2D hydrodynamical simulation, showing the density (left) and radial velocity (right) structures. The red curves represent instantaneous values, and the black curves represent time-averaged values. Values have cgs units, i.e., density is in grams per centimeter squared, and radial velocity is in centimeters per second (Sundqvist et al. 2018, Figure 5). . . . . 14
- 2 The top panel shows an example X-ray spectrum model with a typical absorption model for  $\zeta$  Pup (with super-solar nitrogen abundance and sub-solar carbon and oxygen abundances) in black. We compare it with a spectrum with an absorption model of solar opacity (in red), and a spectrum with no absorption (in blue). The bottom panel shows the corresponding typical opacity in black, and solar opacity in red. The spectra are modeled with a multi-temperature emission model (Foster et al. 2012, *bvapec*) paired with an absorption model (Leutenegger et al. 2010, *vwindtab*) which we discuss in Chapter 3. . . . . 19
- 1.I Visualization for the  $u_{\text{crit}} = R_*/R_{\text{crit}}$  derivation. The white circle represents the star, the grey ring represents the volumes below the onset radius  $R_o$  with no X-ray emission, and the grey dotted lines represent the boundary of wind occultation, assuming the observer is on the far left. The angle between  $R_{\text{crit}}$  and  $R_x$  is  $\pi - \theta$ . . . . . 29



1.7	The cycle 19 to cycle 1 line flux ratios with error bars showing 68% confidence limits propagated from the cycle 19 and cycle 1 emission line fit results. The red line indicates a horizontal best-fit at 1.13, representing a 13% flux increase from cycle 1 to cycle 19. This increase has some modest wavelength dependence. . . . .	44
1.8	The emission lines and line complexes (in black solid dots) with their surrounding continuum regions (in black hollow dots bounded by vertical dotted lines) are shown in MEG and HEG pairs. The red dashed lines show the best-fit flat power-law model to the continuum, and the grey hollow dots show nearby emission lines that are excluded while fitting the continuum. Error bars on the data points represent 68% uncertainties by Poisson distributions. Data from the 21 new cycle 19 observations are combined in all figures. . . . .	46
1.9	The emission lines (in black solid dots) and their best-fit line profile models (in red solid histograms) on top of the continuum models (in red dashed lines) are shown in MEG and HEG pairs. The continuum models are the same as in Figure 1.8. The dark grey vertical dashed line indicates the rest wavelength of each line, and the light grey vertical dashed lines indicate the Doppler shifted wavelengths corresponding to the wind terminal velocity of $2250 \text{ km s}^{-1}$ . Error bars on the data points represent 68% uncertainties by Poisson distributions. Data from the 21 new cycle 19 observations are combined in all figures. . . . .	47
1.10	Same as Figure 1.9 but for cycle 1. . . . .	48
2.1	Count rate (top panel), effective area (middle panel), and flux (bottom panel which is the count rate divided by the effective area) of the first and second <i>XMM-Newton</i> observations (ObsID 0095810301, 0095810401). Blue-shaded regions are common wavelength regions with nonzero effective area in all observations, across which we integrate to get the total effective area $\sum A_{\text{eff}}$ and the total flux $\sum(\text{data}/A_{\text{eff}})$ . We show only the RGS1 spectra for this demonstration. . . . .	54
2.2	Blue-shaded regions show the common wavelengths covered by all observations, across which we integrate to get the total flux. RGS1 wavelength coverage is shown on the left, and RGS2 on the right. The RGS1 regions are identical to the ones in Figure 2.1. . . . .	57

2.3	Total RGS <sub>1</sub> +RGS <sub>2</sub> X-ray flux for each of the 28 <i>XMM-Newton</i> observations, integrated from 0.9 to 2 keV but only over the wavelength intervals for which there is data in each observation, i.e., the blue bands in Figure 2.2. Grey bands indicate the periods when the <i>Chandra</i> cycle 1 and cycle 19 data were taken. The weighted mean of RGS <sub>1</sub> +RGS <sub>2</sub> flux is shown in green dotted line, and the linear fit is shown in purple dashed line. . . . .	57
2.4	Left panel shows Kuiper statistics for RGS <sub>1</sub> data (grey) and RGS <sub>2</sub> data (blue), which give nearly identical results, from frequencies $f_0 = 1.05 \times 10^{-9} \text{ s}^{-1}$ to $3.5 \times 10^{-8} \text{ s}^{-1}$ . The horizontal dashed line indicates a Kuiper statistic of 0.3, arbitrarily determined to filter high Kuiper statistic frequency regions. Vertical dashed lines indicate three frequencies ( $0.21, 2.13, 3.17 \times 10^{-8} \text{ s}^{-1}$ ) with relatively high Kuiper statistics. No dominant period is found. Right panel shows the reduced chi-square values of RGS <sub>1</sub> and RGS <sub>2</sub> data fitted with sine waves, with test frequencies that have Kuiper statistic values above 0.3. . . . .	61
2.5	Individual sine wave fits to RGS <sub>1</sub> and RGS <sub>2</sub> data, with fixed frequencies at 0.21 (top panel), 2.13 (middle panel), and $3.17 \times 10^{-8} \text{ s}^{-1}$ (bottom panel), corresponding to periods of around 15.1, 1.5, and 1.0 years. RGS <sub>1</sub> data points are shown in black and fits are shown in pink dashed curves. RGS <sub>2</sub> data points are shown in blue and fits are shown in red dashed curves. All fits are statistically bad, indicating low likelihood of these frequencies. . . . .	63
3.1	Quantity in equation 3.6 as a function of temperature of multiple ions calculated from ATOMDB. The curves can be interpreted as emissivities scaled by elemental and ion abundances, where the elemental abundances are assumed to be solar. Only line emission is taken into account. The vertical dashed lines intersecting almost all peaks of the emissivity curves represent the six temperatures we chose to approximate the shock-heated plasma.(Cohen et al. 2021, Figure 3) . . . . .	71
3.2	Transmission curves derived from the <i>windtabs</i> model according to equation 3.15 (black solid line), the exospheric model (dashed line), and the slab model (dotted line). Values of $\beta = 1$ and $R_o = 1.5R_*$ are adopted (Leutenegger et al. 2010, Figure 5). . . . .	75
3.3	The opacity $\kappa_\lambda$ with He II photoionization taken into account, assuming $\zeta$ Pup's best-fit elemental abundances with enhanced nitrogen and depleted carbon and oxygen (in dashed black line), and solar abundances (in dashed red line). The solid lines show the corresponding $\kappa_\lambda$ without He II photoionization, and are identical to the lines shown in Figure 2. . . . .	77

3.4	The grouped RGS1 (top panel) and RGS2 (bottom panel) spectra of the first <i>XMM</i> observation (ObsID 0095810301). The effect of groupings can be observed by comparing the ungrouped spectra (light grey) with the grouped spectra (black). The gap in the RGS2 spectrum is due to degradation in the CCD assembly (see Section 2.3). . . . .	78
3.5	Broadband spectral modeling of <i>XMM</i> RGS1 spectra with ObsID 0561380101 (top left), 0810870201 (top right), 0095810301 (middle left), 0810870101 (middle right), 0157161101 (bottom left), 0159360701 (bottom right). Black curves show the data, and red curves enhanced by grey shadings show the models. . . . .	80
3.6	Emission measure as a function of plasma temperature for the 28 observations (each in a different color) and their mean weighted by the observations' exposure times (in black). The emission measures at the two low-temperature components have been averaged together due to degeneracy between the two temperature components, and those at the highest temperature component are omitted since they are found to be consistently zero. The temperatures are evenly spaced at 0.23 dex logarithmic intervals ( $\Delta \log T = 0.23$ ), and the differential emission measures have units of per dex K. . . . .	83
3.7	Time variability of mass-loss rate (top panel) and total emission measure (bottom panel). Each data point represent an <i>XMM</i> observation. Grey bands indicate the periods when the <i>Chandra</i> cycle 1 and cycle 19 data were taken. . . . .	84
3.8	The correlations between the mass-loss rate and the total emission measure (left panel), the mass-loss rate and the total flux (middle panel), and the total flux and the total emission measure (right panel). The Pearson correlation coefficients from left to right are 0.90, 0.13, and 0.32, respectively. . . . .	85
3.9	Pseudo-spectrum produced from isothermal <i>bvapec</i> models at the six chosen temperatures, assuming solar elemental abundances, norms of unity, and no wind absorption. We note that emission at long wavelengths comes from relatively low-temperature plasma. . . . .	86
3.10	Differential emission measures (DEM) from the <i>Chandra</i> cycle 1 (blue) and cycle 19 (red) observations on $\zeta$ Pup (left panel, from G. Rak's 2022 KNAC symposium poster), and from <i>Chandra</i> observations on a set of O and early B stars (right panel, from Cohen et al. (2021, Figure 4)). . . . .	87

TO MY PARENTS

# Acknowledgments

I express my deepest appreciation to my advisor David Cohen for his continuous support. His profound knowledge and passion for astrophysics have motivated me through my research. I thank Véronique Petit and Maurice A. Leutenegger, who provided invaluable guidance and advice on my research. I also thank Eric Jensen, who provided helpful feedback on my thesis.

I thank my classmates and friends Gwendolyn Rak, Winter Parts, Lamiaa Dakir, and Chloe Mayhue, who contributed to my enjoyable research experience. I also thank Kyra Roepke from Swarthmore Writing Center, who helped me with my writing.

Finally, I want to thank my family for their unconditional love, and for their understanding and support in the many decisions I made in life.

# 0

## Introduction

### 0.1 OVERVIEW

A massive star can lose up to half of its mass during its lifetime in the form of a stellar wind. The stellar wind, which is the continuous outflow of particles from the stellar atmosphere, plays an important role in the star's evolution and interacts with the neighboring interstellar medium, enriching its chemical abundances and affecting its kinematics.

Stellar winds are induced through different mechanisms. The wind of our Sun is a coronal wind driven by gas pressure at high temperature, and the Sun loses mass at a rate of about  $10^{-14} M_{\odot} \text{ yr}^{-1}$  (1 part in 100 trillion of its own mass every year). However, the Sun is far from being massive. The subject of this thesis,  $\zeta$ Puppis, has its wind driven by its high luminosity: the photospheric photon momentum exerts a large radiation force on the ions in the wind that overcomes gravity and pushes them away from the star. As we will discuss in Section 0.2.1, this driving mechanism is made possible and efficient by the velocity gradient in the wind, and  $\zeta$ Pup achieves a mass-loss rate on the order of  $10^{-6} M_{\odot} \text{ yr}^{-1}$  (Lamers & Cassinelli 1999).

The massive star  $\zeta$ Pup is an O<sub>4</sub> blue supergiant with a mass of about 25 solar masses and a luminosity of 450,000 solar luminosities (Howarth & van Leeuwen 2019). As one of the most luminous stars in the Milky Way and one of the closest O stars to Earth,  $\zeta$ Pup has been a target of observations and studies for decades (refer to Blomme et al. (2003) for studies in the radio band, Harries & Howarth (1996) in the H $\alpha$  emission line, Eversberg et al. (1998) in the He II 4686 Å emission line, Reid & Howarth (1996) in the optical band, Prinja & Howarth (1986) in the UV band, Cassinelli et al. (2001) in the X-ray band, and many others). Table 1 summarizes the basic properties of  $\zeta$ Pup.

Table 1: Properties of  $\zeta$ Pup

HD#	Spectral type	Distance (pc)	$T_{\text{eff}}$ (kK)	$R_*$ ( $R_{\odot}$ )	$\log L_{\text{bol}}$ ( $L_{\odot}$ )	$v_{\infty}$ (km s $^{-1}$ )
66811	O <sub>4</sub> I(n)fp <sup>a</sup>	$332 \pm 11^b$	$40 \pm 1^c$	$18.9^d$ ( $13.50 \pm 0.52^e$ )	$5.65 \pm 0.06^c$	2250 <sup>e</sup>

References: <sup>a</sup>Sota et al. (2014); <sup>b</sup>van Leeuwen (2007); <sup>c</sup>Howarth & van Leeuwen (2019);

<sup>d</sup>Najarro et al. (2011); <sup>e</sup>Puls et al. (2006). We use  $R_* = 18.9 R_{\odot}$  in this thesis although another value of  $13.5 \pm 0.52 R_{\odot}$  is reported. Since the mass-loss rate is linearly proportional to the stellar radius, the derived mass-loss rates in the following chapters can be easily scaled up or down to match up with an updated value of the stellar radius.

O-type stars have been known to be powerful X-ray sources since the observations of the early *Einstein Observatory* (Harnden et al. 1979). Initially, little differentiation was made on the X-ray emission processes between the massive stars and our Sun. The Sun emits X-rays in the solar corona, where the hot, X-ray emitting zones are confined by the surface magnetic loops. It was not until 1999, with the launches of two high resolution X-ray satellites *Chandra* and *XMM-Newton*, that people realized from the spectrally resolved, Doppler-broadened X-ray emission lines that the X-rays of massive stars come from throughout the stellar winds rather than the stellar surfaces (Cassinelli et al. 2001; Kahn et al. 2001). X-ray diagnostics of the stellar wind properties have been developed since then.

The X-rays in massive stars are generated through three possible mechanisms (Cohen et al. 2011): (1) embedded wind shocks (EWS) from the intrinsic instabilities in the radiation-driven wind (Lucy & White 1980; Owocki et al. 1988; Feldmeier et al. 1997), (2) colliding wind shocks (CWS) from the colliding winds of two stars in a binary system (Stevens et al. 1992), and (3) magnetically confined wind shocks (MCWS) from the colliding wind clumps following the magnetic field lines of stars as strong magnetic dipoles (ud-Doula & Owocki 2002). Because  $\zeta$ Pup is neither in a binary system nor has a strong magnetic field, the X-rays from its wind must be produced through the EWS mechanism. Section 0.2.1 discusses how instabilities arise from radiation-driven winds and produce X-rays.

It is known that  $\zeta$ Pup is a variable star. A periodicity of 1.78 days in optical data has been identified by several authors (Howarth & Stevens 2014; Nichols et al. 2021) that might correlate with the rotational period of the star. Changes in the shape of emission lines in the UV and optical data have also been reported (Baade 1991; Howarth et al. 1995; Berghoef et al. 1996). Nevertheless, the mass-loss rate of  $\zeta$ Pup is neither observed nor expected in

theory to change substantially. This thesis will present two separate, independent ways of determining the mass-loss rate of  $\zeta$  Pup from the X-ray data: one from analyzing individual emission lines, and the other from the broadband spectra. We find a surprising mass-loss rate variation of as high as 40% over timescale of months to years, and a correlation between the mass-loss rate and the amount of X-ray emitting gas.

My advisor's research group has been developing and applying these mass-loss rate diagnostics on data from the cycle 1 *Chandra* observation taken in 2000 (Cohen et al. 2010; Leutenegger et al. 2013; Cohen et al. 2021). I started my project with the aim of better constraining  $\zeta$  Pup's mass-loss rate given a new set of long cycle 19 *Chandra* observations taken in 2018 and 2019 (discussed in Chapter 1). With an exciting discovery of mass-loss rate increase by 40% from cycle 1 to cycle 19, I then analyzed data from the *XMM* observations and confirmed  $\zeta$  Pup's X-ray flux and mass-loss variation (discussed in Chapters 2 and 3).

## 0.2 THE WIND OF $\zeta$ PUPPIS

In this section, we will discuss the driving mechanism of the wind of  $\zeta$  Pup, and introduce two fundamental parameters, the mass-loss rate and the terminal wind velocity, that characterize the wind.

### 0.2.1 THE RADIATION-DRIVEN WIND

The massive star  $\zeta$  Pup can be approximated as a 40,000 K blackbody that radiates primarily in the ultraviolet band. These UV photons interact with the ions in the wind through line scattering and transfer photon momentum to the ions in the wind. In a line scattering process, a bound electron undergoes photo-excitation followed by de-excitation to the same

original level, emitting a photon with almost the same energy as the one absorbed but moving in another direction<sup>1</sup>. Since the photo-excitation process is radially outward from the star and the re-emission is isotropic (the same in all directions), a radially outward net force is exerted on the material in the wind.

We can perform a simple, back-of-the-envelope calculation to convince ourselves that a radially outward radiative force in the wind can overcome gravity. Suppose an ion at distance  $r$  interacts with a specific narrow range of photons with energies centered at  $E$  corresponding to wavelength  $\lambda$ , and these photons are not absorbed on their path from the stellar photosphere to the ion. We will later explain why these assumptions are reasonable. The photons have a momentum  $p = E/c$  where  $c$  is the speed of light, and exert on the ion a radiative force

$$F_{\text{rad}} = \frac{dp}{dt} = \frac{1}{c} \frac{dE}{dt} = \frac{F_\lambda \sigma_\lambda}{c}, \quad (1)$$

where  $F_\lambda$  is the flux received by the ion due to the star's radiation at wavelength  $\lambda$ , in units of energy per second per unit area. Here  $\sigma_\lambda$  is the line scattering cross section of the ion at wavelength  $\lambda$ . We can calculate  $F_\lambda$  from the inverse square law,  $F_\lambda = L_\lambda / 4\pi r^2$ , where  $L_\lambda$  is the luminosity of the star at wavelength  $\lambda$ . Then the radiative force on the ion is

$$F_{\text{rad}} = \frac{L_\lambda \sigma_\lambda}{4\pi r^2 c}. \quad (2)$$

The force of gravity on the ion is  $F_{\text{grav}} = GMm/r^2$  where  $m$  is the mass of the ion,  $M$  is the mass of the star, and  $G$  is the gravitational constant. We thus define the Eddington factor

---

<sup>1</sup>We thus use the words “scatter” and “absorb” interchangeably in this section.

to be the ratio of the radiative to the gravitational force,

$$\Gamma = \frac{F_{\text{rad}}}{F_{\text{grav}}} = \frac{L_\lambda \sigma_\lambda}{4\pi c G M m} = \frac{L_\lambda \kappa_\lambda}{4\pi c G M}. \quad (3)$$

We define  $\kappa_\lambda \equiv \sigma_\lambda/m$  to be the opacity (or absorption coefficient) of the wind at wavelength  $\lambda$ , in units of area per mass. Notice that the explicit radial dependences of both forces cancel each other, and  $\Gamma$  appears to be independent of  $r$ . However, since ions at different layers interact with photons with different wavelengths,  $\Gamma$  implicitly varies with distance. We note that when  $\Gamma > 1$  in the surrounding neighborhood of the star, then ions move away from the star, inducing a stellar wind. If  $\Gamma > 1$  within the stellar photosphere, then the star is no longer stable. For any massive star like  $\zeta$  Pup with a radiation-driven wind,  $\Gamma$  must be below unity inside the star and above unity in the wind.

We now explain the two assumptions we made, that ions at different distances interact with photons of different energies, and that these photons are not absorbed by other ions closer to the star. Suppose species of ions are evenly distributed throughout the wind<sup>2</sup>. If the wind is static, each species of ions at all distances absorbs photons within a fixed Maxwell-Boltzmann energy distribution centered at its energy level transition<sup>3</sup>. In a dense, optically thick wind, only the lower layers of the wind absorb these photons, as the upper layers are shielded even though not all photons are effectively absorbed. However, the winds of massive stars are not static but have a velocity gradient where the wind speed is higher farther away

<sup>2</sup>This is not true for helium or other light elements that can easily be fully ionized by UV photons, but it is true for most of the ions that interact with photons through line scattering, such as the hydrogen- or helium-like carbon, nitrogen, and oxygen ions.

<sup>3</sup>If a single ion is static, then it absorbs photons at a single wavelength. Random thermal motions in a static wind dictates that a group of identical ions will follow a Maxwell-Boltzmann velocity distribution, and thus will absorb photons at slightly different wavelengths.

from the star. This velocity gradient is capable of two things: (1) It redshifts the photospheric photons with respect to ions at different distances to different extents. By the Doppler shift equation  $(\lambda - \lambda_0)/\lambda_0 = v/c$ , an ion with a speed  $v$  that naturally scatters photons at wavelength  $\lambda_0$  now scatters those emitted at a shorter wavelength  $\lambda$ , so that these photons can be redshifted to wavelength  $\lambda_0$  when reaching the ion. Therefore, ions at different layers in the wind can scatter photospheric photons of different wavelengths that are only slightly attenuated when passing through the lower layers with smaller wind velocities. (2) The velocity gradient exposes the otherwise shielded ions, so now the overall number of photons scattered at each wavelength increases, and so does the opacity  $\kappa_\lambda$ . We note that effect (1) sustains the wind driving mechanism throughout the wind, and effect (2) makes the driving mechanism efficient.

The story is different inside the star. There is no velocity gradient, and thus the Doppler deshadowing effect no longer exists. The environment is optically thick near the stellar center, and thus photons created from fusion reactions at the stellar center are severely attenuated. The Eddington factor does not exceed unity, and the star is held together by gravity.

Indeed,  $\zeta$ Pup appears to be a stable star. We assume that electron scattering dominates within the star with an opacity of  $\kappa \approx 0.034 \text{ m}^2 \text{ kg}^{-1}$  independent of wavelength. We use the bolometric luminosity  $L \approx 10^{5.65} L_\odot$  from Table 1 and estimate the stellar mass to be  $25 M_\odot$  (Howarth & van Leeuwen 2019). The Eddington factor under the stellar photosphere is therefore

$$\Gamma_{\text{star}} = \frac{(10^{5.65} L_\odot)(0.034 \text{ m}^2 \text{ kg}^{-1})}{4\pi c G (25 M_\odot)} = 0.46, \quad (4)$$

which is less than unity but only by a modest amount. As a comparison, the Eddington factor for our Sun is around  $2.6 \times 10^{-5}$ .

In the wind of  $\zeta$ Pup, the interaction cross section of line scattering is wavelength-dependent and is much greater than that of electron scattering. Although the effective luminosity at a given deshadowed radius for a given line-scattering atom is less than the bolometric luminosity, the Eddington parameter can easily exceed unity and sustain a radiation-driven stellar wind.

### 0.2.2 MASS CONTINUITY AND VELOCITY LAW

The winds of massive stars embody the fundamental concept of mass conservation, i.e., mass is neither created nor destroyed. If  $\zeta$ Pup has a mass-loss rate  $\dot{M}$ , mass continuity implies that at any point in the wind with density  $\rho$  and velocity  $v$ ,

$$\dot{M} = 4\pi\rho(r)v(r)r^2, \quad (5)$$

where we assume that the wind is spherically symmetric and radially flowing outward.

We next model the wind velocity as a function of distance away from the star. For a stellar wind ion, the force of gravity is inversely related to the distance squared, and so is the force of radiation (equation 2), assuming no photon attenuation in the wind below. The net acceleration of a stellar wind ion can thus be written as  $a = kr^{-2}$  where  $k$  is a constant. Since acceleration is  $a = dv/dt = v dv/dr$ , we solve the first order differential equation  $kr^{-2} = v dv/dr$ . The solution is

$$\frac{1}{2}v^2 = -\frac{k}{r} + C, \quad (6)$$

where  $C$  depends on a boundary condition. Supposing that the velocity at the base of the

wind is zero, we have  $v(R_*) = 0$  and thus  $C = k/R_*$ . Solving for  $v(r)$ , we get

$$v(r) = k' \left(1 - \frac{R_*}{r}\right)^{1/2}, \quad (7)$$

where  $k'$  contains the related constants from previous equations. Equation 7 is the prototype of the  $\beta$ -velocity law. We note that if the wind has a greater-than-zero attenuation on the radiative force,  $v(r)$  will increase with  $r$  at a rate slower than expected. But despite the rate of increase,  $v(r)$  should approach some terminal velocity  $v_\infty$  as  $r$  approaches infinity. We can now write down the  $\beta$ -velocity law of winds,

$$v(r) = v_\infty \left(1 - \frac{R_*}{r}\right)^\beta. \quad (8)$$

In equation 8 above,  $\beta$  is usually greater than 0.5 and is typically 1 for O stars. A larger  $\beta$  corresponds to a slower increase in velocity with respect to distance, that is, a faster fall-off in radiative force in the wind. Thus, O stars with dense winds and strong absorption tend to have large  $\beta$  values. The P Cygni profiles (a Doppler-broadened line profile in the ultraviolet band showing distinct emission and absorption features) of  $\zeta$  Pup show a terminal velocity of  $2250 \text{ km s}^{-1}$ .

### o.3 X-RAY FORMATION IN THE WINDS

The previous section describes the ultraviolet line scattering in the wind of  $\zeta$  Pup. In this section, we will discuss the origin of X-rays, and the X-ray emission and absorption mechanisms in the wind.

### 0.3.1 X-RAY FROM INSTABILITY AND SHOCKS

The X-rays come from an inherent instability, the line-deshadowing instability (LDI), in any radiation-driven wind (Lucy & White 1980; Owocki et al. 1988; Feldmeier et al. 1997). The smooth, steady-state velocity law in equation 8 requires an equally smooth acceleration of  $a(r) = kr^{-2}$  multiplied by an attenuation factor  $2\beta(1 - R_*/r)^{2\beta-1}$ , made possible by the Doppler deshadowing effect<sup>4</sup>. The instability arises once an ion in the wind travels slightly faster than its neighbors, exposing itself to more photospheric photons and radiative acceleration, and shielding the photons from the ions at a layer further away from the star. The collisions between the fast-moving wind regions and the slow-moving ones generate supersonic shock waves and heat up the shocked gas to above a million degrees, the condition for X-ray radiation. The wind collisions can be described in terms of shock jump conditions, related to the physics of shocks. We briefly discuss relevant concepts in the following paragraphs.

An important characteristic of the wind is the sound speed, which is the speed at which wind particles communicate information about the temperature, pressure, and density. If a wave travels subsonically through the wind, the perturbed regions will quickly calm into steady-state. And if a wave travels supersonically, preshock regions are not “warned” by the upcoming wave and so are significantly compressed and heated as the wave passes by. We find the sound speed by imagining what happens if the wind is slightly disturbed.

A small disturbance in the wind is like a push on a pendulum from its equilibrium steady-state. Let  $\rho$  be the density and  $P$  be the pressure of the wind. A small disturbance means  $\rho(x, t) = \rho_0 + \rho_1(x, t)$  and  $P(x, t) = P_0 + P_1(x, t)$ , where  $\rho_0, P_0$  are the steady-state values and

---

<sup>4</sup>The attenuation factor is derived from differentiating equation 8 with respect to  $r$ .

$\rho_1, P_1$  represent density and pressure fluctuations. Assuming  $\rho_1 \ll \rho_0$  and  $P_1 \ll P_0$ , we can use the conservation of mass (equation of continuity), momentum (acceleration equation), and energy (equation of energy) to model the perturbation by a wave equation,

$$\frac{\partial^2 \rho_1}{\partial t^2} = \left( \frac{\partial P}{\partial \rho} \right)_0 \frac{\partial^2 \rho_1}{\partial x^2}. \quad (9)$$

The wave equation has a typical wave solution

$$\rho_1 \propto e^{i(kx - \omega t)}, \quad \omega^2 = k^2 \left( \frac{\partial P}{\partial \rho} \right)_0, \quad (10)$$

where  $\omega$  and  $k$  are two constants constrained by some given conditions, and are referred to as the angular frequency and wavenumber, respectively. The sound speed of the wind is thus  $c_s = \omega/k$ . If the wind is adiabatic, then  $c_s = [(\partial P / \partial \rho)_0]^{1/2} = (\gamma k T_0 / m)^{1/2}$  by the ideal gas law, where  $m$  is the mass (or the weighted mean mass) of a wind particle and  $\gamma$  is the ratio of specific heats at constant pressure and constant volume.

Note that the wave solution satisfies  $\rho_1(x, 0) = \rho_1(x + c_s t, t)$ , which translates into the preservation of shape of the wave as it propagates. This no longer holds true when the disturbance is large and  $\rho_1$  is comparable to  $\rho_0$ . When a wave travels at speed greater than  $c_s$ , the wind becomes so perturbed that a region emerges where the gradients of density, pressure, and volume are infinite; and each side of the shock front (the postshock gas and the ambient gas) can still be characterized by their respective wind sound speeds  $c_1$  and  $c_2$ .

Although we do not know what happens to the functions of state at the shock front, we can relate the shocked and the ambient gas with the shock jump conditions. We first introduce the Mach number  $M \equiv u_1/c_1$ , where  $u_1$  is the speed of the shock front with respect to

the ambient gas, so that  $M$  measures the shock strength. Let  $u_2$  be the speed of the shocked gas with respect to the shock front. The Rankine-Hugoniot relations can be derived from the conservation of mass, momentum, and energy to be

$$\rho_1 u_1 = \rho_2 u_2, \quad (11)$$

$$P_1 + \rho_1 u_1^2 = P_2 + \rho_2 u_2^2, \quad (12)$$

$$e_1 + \frac{1}{2} u_1^2 + \frac{P_1}{\rho_1} = e_2 + \frac{1}{2} u_2^2 + \frac{P_2}{\rho_2}. \quad (13)$$

The subscripts 1 and 2 in the three equations above represent the ambient and the shocked regions, respectively. And  $e$  is the energy per unit mass of the wind particles. From thermodynamics,  $e = C_V T$  where  $C_V$  is the specific heat capacity (heat capacity per unit mass), and  $C_V = k/m(\gamma - 1)$ . We substitute these relations, the ideal gas law, and the equation of sound speed  $c_s = \gamma k T / m$  into equations 11, 12, and 13 to get the jump conditions,

$$\frac{\rho_1}{\rho_2} = \frac{u_2}{u_1} = \frac{\gamma - 1}{\gamma + 1} + \frac{2}{M^2(\gamma + 1)}, \quad (14)$$

$$\frac{P_2}{P_1} = \frac{2\gamma M^2}{\gamma + 1} - \frac{\gamma - 1}{\gamma + 1}, \quad (15)$$

$$\frac{T_2}{T_1} = \frac{c_2^2}{c_1^2} = \frac{P_2 \rho_1}{P_1 \rho_2} = \left( \frac{2\gamma M^2}{\gamma + 1} - \frac{\gamma - 1}{\gamma + 1} \right) \left( \frac{\gamma - 1}{\gamma + 1} + \frac{2}{M^2(1 + \gamma)} \right). \quad (16)$$

The Rankine-Hugoniot relations and the jump conditions relate the density, pressure, energy, and temperature of the shocked and the ambient sides of the wind (derivations are from Harvard University Astronomy 145 class notes spring 1990).

The sound speed of  $\zeta$ Pup is around  $20 \text{ km s}^{-1}$ , assuming  $\gamma = 5/3$ ,  $T \approx 40 \text{ kK}$  based on the effective temperature of the star, and  $m \approx m_H = 1.67 \times 10^{-27} \text{ kg}$ . This is much smaller than the speed of shock waves, which is several hundred kilometers per second near the base of the wind from the hydrodynamical simulations discussed in the following paragraph (Sundqvist et al. 2018). We therefore conclude that  $M^2 \gg 1$ , and thus  $P_2 \gg P_1$  and  $T_2 \gg T_1$ . We use  $P_2 = P_1 + \rho_1 u_1^2 - \rho_2 u_2^2 \approx \rho_1 u_1^2 - \rho_2 u_2^2$  from equation 12 and  $\rho_1/\rho_2 = u_2/u_1 = 1/4$  from equation 14 to get  $P_2 = (3/16)\rho_2 u_1^2$ . We then use the ideal gas law to derive the shock speed necessary for X-ray production,

$$T_2 = \frac{mP_2}{k\rho_2} \approx \frac{3m_H}{16k} u_1^2 \approx 2.3 \times 10^{-5} u_1^2. \quad (17)$$

Equation 17 indicates that a shock jump velocity of slightly more than  $200 \text{ km s}^{-1}$  can produce a shocked wind region with temperature above a million Kelvin. Assuming  $(3/2)kT = h\nu$ , then the million-degree gas can produce soft X-ray photons of around  $100 \text{ \AA}$ . Indeed, the *XMM* observations show emission lines of  $\zeta$ Pup from  $5 \text{ \AA}$  to  $35 \text{ \AA}$ , corresponding to the existence of two- to twenty-million-degree shock-heated plasma. More details of the temperature dependence of the X-ray spectrum will be discussed in Chapter 3.

Sundqvist et al. (2018) performed 2D hydrodynamical simulations of a radiation-driven wind, and showed the formation of complex wind structures due to the line-deshadowing instability. Figure 1 shows a radial slice of the simulated wind, revealing both the instantaneous (red curves) and the time-averaged (black curves) density and radial velocity behaviors. The

peaks of the radial velocity curve represent shock fronts, and are followed by small-scale wind clumps with high density and temperature. The high temperature leads to an increase in the rate of collisional excitation of the wind particles, and these shocks quickly cool by radiation as the excited states spontaneously decay, emitting photons that result in energy loss.

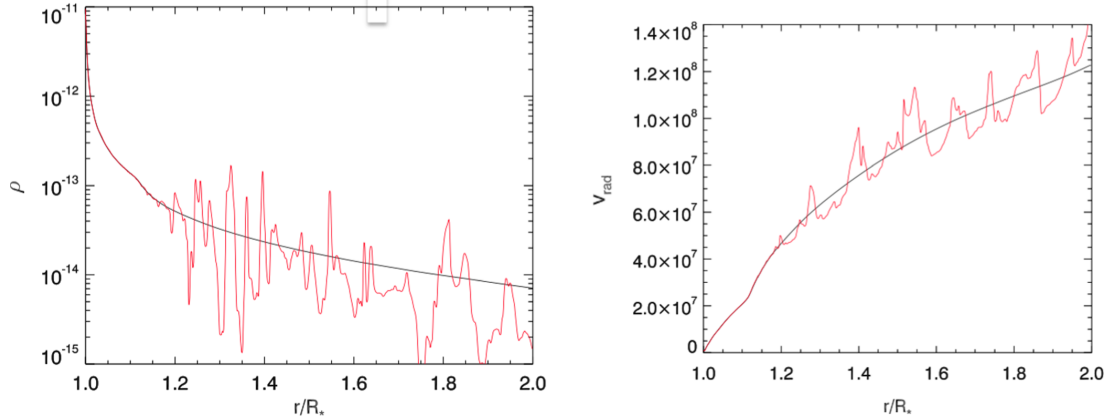


Figure 1: A radial slice of a radiation-driven wind from the 2D hydrodynamical simulation, showing the density (left) and radial velocity (right) structures. The red curves represent instantaneous values, and the black curves represent time-averaged values. Values have cgs units, i.e., density is in grams per centimeter squared, and radial velocity is in centimeters per second (Sundqvist et al. 2018, Figure 5).

Note that shocks form not at the base of the wind, but at around 1.2 stellar radii, and the earlier shocks are not strong enough to produce X-rays. As discussed, X-ray emission only happens when the temperature of the shock-heated region is above a million Kelvin, corresponding to an X-ray onset radius at around  $1.5 R_*$  (Runacres & Owocki 2002; Sundqvist et al. 2018). We explore this quantity in detail in Chapter 1.

The black curves of Figure 1 generally demonstrate the shapes of the mass continuity equation and the  $\beta$ -velocity law. In particular, hydrodynamical simulations show that preshock regions generally have velocities above the  $\beta$ -velocity law but slow down as they pass through

the shock fronts, and the postshock regions which are the X-ray emitting plasma follow the  $\beta$ -velocity law well. Readers will find in later chapters that we use these time-averaged, smooth models to explain the X-ray emission and absorption features, although the X-rays themselves come from the time-dependent, inhomogeneous wind structures. This is because the shock lifetime from radiative cooling is very small, much shorter than a *Chandra* or *XMM* observation. Additionally, as we observe the wind of  $\zeta$  Pup, we are collecting X-ray data from a large number of clumps at various stages<sup>5</sup>, as if the structures in the wind are averaged over time.

### 0.3.2 X-RAY LINE AND CONTINUUM EMISSION

The previous section explains the theoretical origin of X-rays in stellar winds. In terms of observational data from *Chandra* or *XMM*, the X-ray spectra consist of emission lines on top of continuum emission, both attenuated in some wavelength-dependent fashion. A typical model of the X-ray spectrum is shown in the top panel of Figure 2.

The X-ray line emission comes from collisional excitations of ions followed by spontaneous de-excitations. As an ion collides with a free electron, the free electron transforms some of its original kinetic energy into exciting the ion, typically from the ground state. And as the ion de-excites, a photon is emitted with energy that corresponds to the energy level transition. In the local winds of O stars, hydrogen and helium atoms are fully photoionized by UV radiation from the star, and thus we do not observe their emission lines<sup>6</sup>. We mostly observe the  $n = 2$  to  $n = 1$  transitions of hydrogen- or helium-like ions (one-electron and

---

<sup>5</sup>This is supported by the modeling of clump density based on the X-ray flux variability in [Nazé et al. \(2013\)](#), and the LDI simulation in [Sundqvist et al. \(2018\)](#) showing a huge number of small shock-heated regions.

<sup>6</sup>Fully ionized helium atoms may recombine into He II ions (helium with 1 electron) at above  $5 R_*$  from the star, and serve as an important source of absorption.

two-electron particles, respectively) from carbon to sulfur, that emit in the X-ray band.

The X-ray continuum emission is mainly produced through two mechanisms: free-free emission (often referred to as Bremsstrahlung emission) and radiative recombination. Free-free emission involves the interaction of two charged particles, usually a free electron and a much heavier ion. As the free electron comes close to the ion, it is deflected through Coulomb force and emits a photon, as charged particles radiate under acceleration according to the Larmor formula. The energy of the emitted photon roughly corresponds to the change in kinetic energy of the free electron. Since the free electron remains free after the interaction, this process is referred to as “free-free”. And since the change in kinetic energy does not have discrete values, free-free emission produces a continuum.

The radiative recombination process involves a free electron colliding into an ion and recombining with it. Consequently, a photon is emitted with an energy equal to the initial kinetic energy of the electron plus the binding energy between the electron and the ion. Since the initial kinetic energy of the electron is not quantized, radiative recombination forms a continuum with an edge at the long-wavelength side that corresponds to the binding energy.

### 0.3.3 X-RAY ABSORPTION

Understanding absorption is as essential as understanding emission as we try to model the observed X-ray data. Studies show that only 1% of  $\zeta$  Pup’s wind is shock-heated to emit X-rays, and the heated plasma is embedded approximately evenly throughout the cold X-ray absorbing bulk of the wind (Runacres & Owocki 2002). More than 90% of the X-rays between 18 and 25 Å from  $\zeta$  Pup are absorbed (Cohen et al. 2021), and the X-ray hardness (more emission towards shorter wavelengths) trend in the spectra of O and B stars discov-

ered by Walborn et al. (2009) is now considered an absorption effect (Cohen et al. 2021; Leutenegger et al. 2010). Indeed, the absorbing mechanism is both efficient and wavelength-dependent. The two mass-loss rate diagnostics we present in this thesis both require close examination of absorption; one (in Chapter 1) is based on the natural geometry of absorption contours that attenuates the long-wavelength sides of individual spectral lines, while the other (in Chapter 3) is based on the wavelength dependence of absorption that hardens the broadband spectrum.

The primary absorption mechanism in the winds of massive stars is bound-free absorption, also known as photoionization. A bound-free process involves a photon ionizing (removing an electron from) a wind atom. The photon must have an energy higher than the ionization energy of the atom, and the resulting free electron has kinetic energy that equals the original photon energy minus the ionization energy. This process results in a continuum absorption with an edge at the long-wavelength side that corresponds to the ionization energy.

The strength of absorption at any point in the stellar wind is modeled by  $I_\lambda = I_{\lambda,0}e^{-\tau_\lambda}$ , where  $I_{0,\lambda}$  is the wavelength-dependent initial X-ray intensity attenuated by a unitless absorption factor  $e^{-\tau_\lambda}$ , and  $I_\lambda$  is the observed intensity. The exponent in the absorption factor is referred to as the optical depth, and expressed as  $\tau_\lambda = \int_0^\infty \kappa_\lambda \rho dz$ . Here,  $\rho$  is the density and  $\kappa_\lambda$  is the absorption coefficient, or opacity, of the absorbing medium along the line of sight of an observer infinitely far away from the point of interest<sup>7</sup>. This is the conventional model of absorption, as the change in intensity of a light ray should be proportional to its original intensity, the distance it travels, and the absorption coefficient as well as the density of the ab-

---

<sup>7</sup>The opacity  $\kappa_\lambda$  here is identical to the definition of opacity in Section 0.2.1. In this section, we use opacity to model X-ray absorption, while in Section 0.2.1, we use opacity to model UV line scattering.

sorbing medium it travels through, which mathematically translates into  $dI_\lambda = -\kappa_\lambda \rho I_\lambda dz$ .

Modeling absorption thus comes down to modeling the wavelength-dependent opacity. For a given atom, the opacity due to photoionization from a given quantum state follows the proportionality  $\kappa_\lambda \propto \lambda^3$  if  $\lambda$  is less than a threshold wavelength that corresponds to the atom's ionization energy, and is otherwise zero. A model of the overall opacity is the sum of opacities from all atomic species multiplied by their abundances. And the abundance of an atomic species must be calculated from its elemental abundance and the ionization balance of the element.

In reality, due to the complexities involved in calculating opacity, the opacity information is stored as a tabulation that can be quickly applied to absorption models used to fit X-ray spectra. Studies show that the X-rays in the winds of O stars like  $\zeta$  Pup tend to only perturb the ionization balance by a small amount (Macfarlane et al. 1994), and the ionization balance is constant in the wind. Additionally, no strong X-ray emission lines fall in between the closely spaced photoionization edges of any given element, so the opacity tabulation use the approximation of a fixed ionization balance for all O star winds (Leutenegger et al. 2010).

We show an opacity model assuming solar elemental abundances (Asplund et al. 2009) as the red curve in the bottom panel of Figure 2, where we see prominent wavelength threshold of each photoionization continuum. The winds of O stars have non-solar elemental abundances due to the CNO cycle (a chain reaction in charge of fusing hydrogen into helium that uses carbon, nitrogen, and oxygen as catalysts) inside the star, and we plot a typical opacity curve with altered abundances on the same plot in black. The top panel of Figure 2 shows an X-ray spectrum of  $\zeta$  Pup in black, modeled with the corresponding opacity. Assuming constant intrinsic X-ray emission, the red curve on the same plot indicates what the spectrum

would look like if solar opacity is assumed, and the blue curve indicates a spectrum with no absorption.

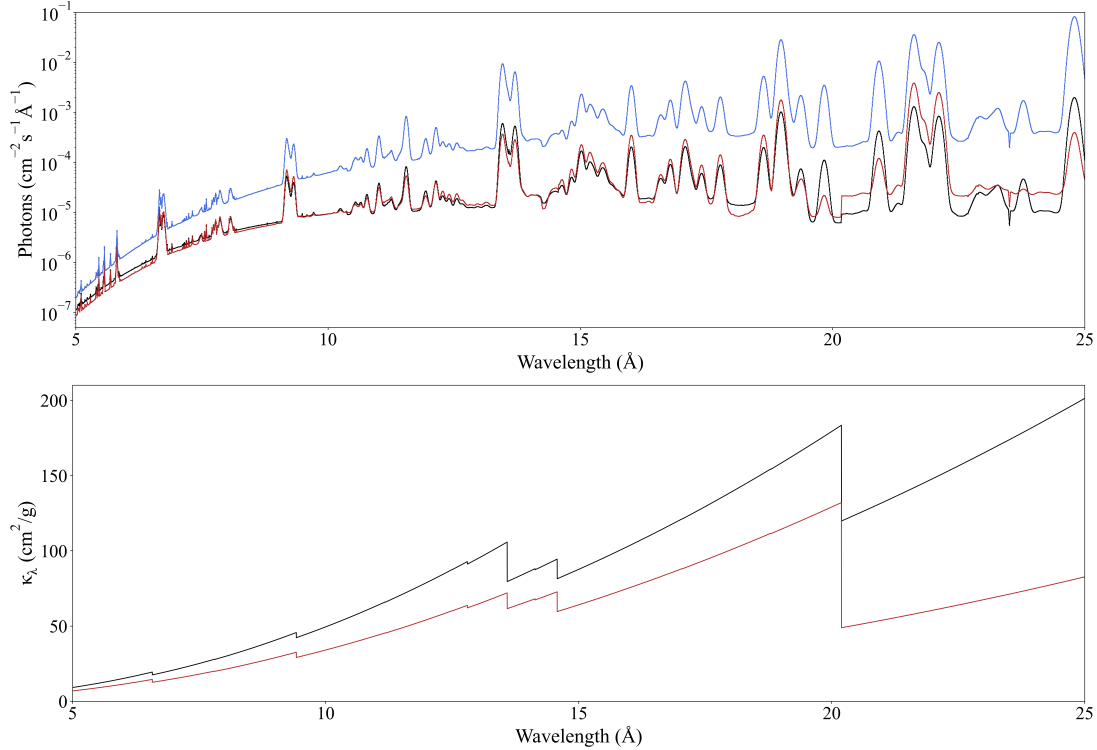


Figure 2: The top panel shows an example X-ray spectrum model with a typical absorption model for  $\zeta$  Pup (with super-solar nitrogen abundance and sub-solar carbon and oxygen abundances) in black. We compare it with a spectrum with an absorption model of solar opacity (in red), and a spectrum with no absorption (in blue). The bottom panel shows the corresponding typical opacity in black, and solar opacity in red. The spectra are modeled with a multi-temperature emission model (Foster et al. 2012, *bvapec*) paired with an absorption model (Leutenegger et al. 2010, *vwindtab*) which we discuss in Chapter 3.

There are two interesting features in Figure 2. (1) The photoionization edges in the black opacity curve indicate dominant absorbing atomic species in the wind of  $\zeta$  Pup. We can trace the edges of Si, Mg, Ne, Fe, and O in the plot from left to right, with the underlying continuum absorption from C and N whose edges are not shown off the right side of the plot.

(2) At longer wavelengths, the opacity is higher and thus the absorption is more significant. This is due to the high carbon and oxygen abundances in the wind (due to the CNO cycle) as well as the rapid falloff in opacity  $\kappa_\lambda$  with wavelength shortward of each photoionization threshold.

We leave the detailed modeling of X-ray absorption, using the opacity tabulation, to later chapters. Chapter 1 will have a section dedicated to calculating the absorption at each point in the wind. Chapter 3 will discuss the average amount of absorption as a function of distance from the star.

We outline the thesis here. Chapter 1 presents the mass-loss rate diagnostic based on individual line profile shapes and our discovery of a surprising 40% mass-loss rate increase from *Chandra* cycle 1 (taken in 2000) to cycle 19 (taken in 2018, 2019), as well as a 13% X-ray flux increase. Chapter 2 explores the X-ray flux variation among 28 *XMM* observations (taken from 2000 to 2021), where we find a flux variation of as high as 16%, but no periodic behaviors or overall increasing or decreasing long-term trend. Chapter 3 presents the mass-loss rate diagnostic based on the broadband X-ray absorption features, and a preliminary result of correlation between the mass-loss rate and the amount of X-ray emitting gas from the *XMM* observations. We summarize the thesis in Chapter 4.

# 1

## Emission Line Analysis of the Mass-Loss Rate of $\zeta$ Puppis

### 1.1 INTRODUCTION

As discussed in Chapter 0, massive stars like  $\zeta$  Pup are known to be powerful X-ray sources due to shocks in their stellar winds. Massive star winds are radiation-driven: ultraviolet pho-

ton momentum exceeds gravity and pushes photospheric plasma away from the star, inducing stellar mass loss. The driving process is prone to an instability that creates small-scale structure and shock-associated heating, which is the source of the observed X-rays (Owocki et al. 1988; Feldmeier et al. 1997).

Two-dimensional hydrodynamical simulations of the line-driven instability suggested a large number of small-scale shocks and clumps dispersed throughout the wind (Dessart & Owocki 2005). Nazé et al. (2013) found short-term X-ray flux variation to be small, suggesting the presence of more than 100,000 small hot X-ray emitting zones in the wind. The small scale and high fragmentation of the wind structures justify our application of a smooth, time-independent model to analyze the X-ray data.

As mentioned in Section 0.3, an X-ray spectrum is dominated by emission lines from highly ionized metals in the shock-heated wind plasma with temperatures over a million Kelvin. Thus the X-ray emission line shapes carry information about wind properties. Specifically, emission lines tend to be asymmetric due to differential absorption of the red-shifted photons from the rear hemisphere of the wind and the blue-shifted photons from the front hemisphere, and the degree of asymmetry is related to the wind column density and thus to the stellar mass-loss rate. In this chapter, we fit an emission line profile model to 10 emission lines from the long *Chandra* grating observations taken during 2018 and 2019 to derive  $\zeta$  Pup’s mass-loss rate, and compare our result with that from *Chandra*’s first observation cycle in 2000.

We describe the form of our emission line model in Section 1.2. Section 1.3 presents the data, Section 1.4 presents our statistical methods to analyze the data, and Section 1.5 presents the results. Section 1.6 discusses the significance of the results and some related ongoing

analysis to independently confirm the mass-loss rate changes and explore the timescale over which they occurred.

## 1.2 MODELING THE EMISSION LINES

In this section, we derive an emission line profile model that we use to fit all emission lines in a spectrum. There are three components we consider in constructing a smooth, time-independent line profile model (Owocki & Cohen 2001): (1) emission lines are generated from the shock-heated wind plasma with emissivity proportional to the wind density squared, (2) they are Doppler-broadened due to high wind speed that follows the  $\beta$ -velocity law  $v = v_\infty(1 - R_*/r)^\beta$  with  $\beta$  set to unity, where  $v_\infty$  is the terminal wind speed and  $R_*$  is the stellar radius (see equation 8), and (3) they are absorbed or attenuated by the cool bulk of the wind by a factor  $e^{-\tau}$ , where the optical depth  $\tau$  at each point in the wind is linearly related to both the wind opacity and the wind mass column density with respect to a distant observer (see Section 0.3.3). Therefore, to model luminosity as a function of the Doppler-shifted wavelength (i.e., the emission line profile), we calculate emission and absorption at every spatial point in the wind, then integrate their product at each wavelength over the entire wind volume.

We naturally adopt the spherical polar coordinate system  $(r, \varphi, \theta)$ , where  $\theta \in [0, \pi]$  is the angle away from the  $z$ -axis that points at the observer (or the *Chandra* observatory), to describe emission in the local wind. We define the scaled Doppler-shifted wavelength,  $x \equiv (\lambda/\lambda_0 - 1)c/v_\infty = -v(r) \cos \theta/v_\infty$  with  $x \in [-1, 1]$ . The X-ray luminosity per wavelength, or the line profile, is

$$L_x = \int \eta_x(r, \varphi, \theta) e^{-\tau(r, \varphi, \theta)} dV d\Omega, \quad (1.1)$$

where the integration is over the total wind volume and solid angle  $\Omega$ ,  $\eta_x$  is the X-ray emis-

sivity per unit volume of the wind in units of energy per time per volume per solid angle per wavelength, and  $e^{-\tau}$  is a unitless absorption factor. Notice that both  $\eta_x$  and  $\tau$  are functions of  $x$  since all three quantities are dependent on  $r$  and  $\theta$ , and  $\eta_x$  represents emissivity at only the locations in the wind with a specific Doppler shift and nowhere else.

We perform the integration over a total of  $4\pi$  steradians and over the  $\varphi$  coordinate, since emission and absorption are independent of  $\varphi$ . The integral can thus be expanded as

$$L_x = 8\pi^2 \int_0^\pi \int_{R_*}^\infty \eta_x(r, \theta) e^{-\tau(r, \theta)} r^2 \sin \theta dr d\theta. \quad (1.2)$$

### 1.2.1 THE EMISSION

X-ray line emission originates from the portions of the wind that are shock-heated to above  $10^6$  K, when the thermal energy of free electrons is high enough to collisionally excite hydrogen- or helium-like metals, as well as some ionized irons (mostly Fe XVII), that populate the wind. X-ray photons are emitted as these excited-state electrons spontaneously decay. We note that X-ray emission comes from carbon to iron ions, while hydrogen and helium atoms are fully ionized by the UV radiation from the star. Since each collisional excitation process that results in emission requires the interaction of a free electron and an ion, the emissivity should be proportional to the densities of both the free electrons and the ions.

In fact, in the reference frame of a free electron colliding with a moving ion, the interaction rate per unit volume is precisely  $n_e n_i v_i \sigma_i$ , where  $n_e$ ,  $n_i$  are the number densities of the free electrons and the ions,  $v_i$  is the relative speed of the ions and the free electrons, and  $\sigma_i$  is the cross section of the ions. Since hydrogen constitutes approximately 90% of all atoms in  $\zeta$  Pup's wind (Martins et al. 2015) and are almost fully ionized as the source of free electrons,

the number density of free electrons can be approximated as the number density of the stellar wind. So we can approximate emissivity at any point in the wind as

$$\eta(r, \theta) = C\rho(r)^2 f(r). \quad (1.3)$$

Notice that in equation 1.3, since we care more about modeling the shape of emission lines rather than its absolute intensity, we introduce an emission normalization constant  $C$  that absorbs atomic physics parameters such as the ion abundance, the collisional cross section, and the spontaneous emission rate. Based on our assumption that the emitting plasma is smoothly distributed throughout the wind with spherical symmetry, we introduce a volume filling factor  $f(r)$ , which could be a function of  $r$  but is assumed to be constant throughout the wind here. The wind density  $\rho$  is also radially dependent, given by the mass continuity equation,  $\rho(r) = \dot{M}/4\pi r^2 v(r)$  (see equation 5). Therefore, the emissivity demonstrates symmetry in the  $\theta$  coordinate.

### 1.2.2 THE ABSORPTION

Despite the prominent emission features we observe in the X-ray band, less than 1% of the mass of the stellar wind is shock-heated to a temperature high enough to produce X-rays. The remaining 99% of the wind is cold and X-ray absorbing, and makes a significant impact on the shape of the emission lines.

In the process of modeling absorption, we note that unlike emission, which is local to the star and demonstrates spherical symmetry around the star, absorption has a directionality associated with the position of the observer and demonstrates cylindrical symmetry around the line of sight of the observer. We thus model the absorption term  $e^{-\tau}$  using cylindrical

$(p, z)$  coordinates, where  $p = r \sin \theta$  and  $z = r \cos \theta$ . By our standard expression for optical depth, incorporating the mass continuity equation and the  $\beta$ -velocity law,

$$\tau(p, z) = \int_z^\infty \kappa_\lambda \rho(p, z') dz' = \frac{\kappa_\lambda \dot{M}}{4\pi v_\infty} \int_z^\infty \frac{dz'}{(p^2 + z'^2)(1 - R_*/\sqrt{p^2 + z'^2})^\beta}. \quad (1.4)$$

Here  $z'$  is the dummy variable of integration and  $z$  is the point we integrate from along a given line of sight towards the observer. The opacity  $\kappa_\lambda$ , as introduced in Section 0.3.3, is constant across a given line profile, though its value varies from line to line in the spectrum. We use the mass continuity equation and the  $\beta$ -velocity law for the second equality.

From the point of view of the observer, the cylindrical volume behind the star is blocked by the star itself, and thus contributes neither absorption nor emission to the line profile. We take this wind occultation effect into account by setting the optical depth to infinity in the proper regions,

$$\tau(p, z) = \begin{cases} \infty, & p \leq R_*; z \leq \sqrt{R_*^2 - p^2}, \\ \tau_* \int_z^\infty \frac{R_* dz'}{(p^2 + z'^2)(1 - R_*/\sqrt{p^2 + z'^2})^\beta}, & \text{otherwise.} \end{cases} \quad (1.5)$$

In equation 1.5, we collect constants in front of the original optical depth integral, which defines the characteristic wind optical depth

$$\tau_* \equiv \frac{\kappa_\lambda \dot{M}}{4\pi v_\infty R_*}. \quad (1.6)$$

When fitting the final line profile model to the observed X-ray emission lines, a fit for  $\tau_*$  would provide information about the mass-loss rate by the relation above.

We notice that the cylindrical coordinate, or any purely spatial coordinate, does not satisfy our goal of expressing luminosity in wavelength space. We therefore transform the coordinates  $(p, z)$  to  $(x, u)$ , where  $x = -v(r) \cos \theta / v_\infty$  and  $u \equiv R_*/r$ , the inverse distance from the star to simplify integration. To express  $z$  in terms of  $x$  and  $u$ , notice  $z = r \cos \theta = -rxv_\infty/v(r)$ . Using the  $\beta$ -velocity law, we get

$$z = -\frac{xR_*}{u(1-u)^\beta}. \quad (1.7)$$

To express  $p$  in terms of  $(x, u)$ , notice  $p = r \sin \theta$  where  $\theta = \arccos(z/r) = \arccos(-x/(1-u)^\beta)$ .

We perform a trigonometric conversion to get

$$p = \frac{R_* \sqrt{(1-u)^{2\beta} - x^2}}{u(1-u)^\beta}. \quad (1.8)$$

Now, when we perform the optical depth integral (equation 1.5, but expressed in terms of  $u$  and  $x$  based on equations 1.7 and 1.8), the result will be a function of  $u$  and  $x$ . The full luminosity integral (equation 1.2) will be performed over  $u$  through a change of variable, and thus the result will be a line profile that is explicitly a function of the independent variable,  $x$ . We show the line profile explicitly below.

### 1.2.3 DETERMINING THE RADIAL INTEGRATION LIMIT

Before we compute the final line profile, we must define the radial lower boundary of integration in equation 1.2 with some careful thoughts. As discussed in Section 0.3.1, X-ray emission does not occur at the base of the wind near the star, but rather starting at an onset radius  $R_o$ . Additionally, for a given Doppler-shift  $x$  contour, not all radii contribute to

the overall luminosity at that wavelength. We consider three effects when determining the boundary of integration: (1) the wind kinematics as they relate to a given Doppler shift, (2) the X-ray onset radius, and (3) the stellar occultation.

For a negative radial velocity contour between the observer and the star, the integration should stop at the inverse distance  $u_x$  that corresponds to the smallest distance from the star on a given  $x$  contour. For some radial velocity contour that extends beyond the onset radius of X-ray emission  $R_o$ , the integration should stop at  $u_o = R_*/R_o$ . For a positive radial velocity contour behind the star, the integration should stop at the boundary of wind occultation  $u_{\text{crit}}$ , if not at  $u_o$ <sup>1</sup>. See Figure 1.1 for a graphical depiction of these three different quantities.

We obtain a mathematical expression of  $u_x$  at a given  $x$  by noticing the location where the radial velocity equals the total velocity,  $v(u_x) = v_r(u_x) = v_\infty(1 - u_x)^\beta$ . Therefore

$$u_x = 1 - |x|^{1/\beta}. \quad (1.9)$$

To find  $u_{\text{crit}}$ , we recall from definition that  $x = -v(R_{\text{crit}}) \cos \theta / v_\infty$ , where  $\theta$  is the angle between  $R_{\text{crit}}$  and the  $z$ -axis pointing at the observer (see Figure 1.1). By substituting  $v(R_{\text{crit}}) = v_\infty(1 - u_{\text{crit}})^\beta$  from the  $\beta$ -velocity law and  $\cos(\pi - \theta) = (R_{\text{crit}}^2 - R_*^2)^{1/2} / R_{\text{crit}}$  from trigonometry,  $u_{\text{crit}}$  can be expressed as a function of  $x$ ,

$$(1 - u_{\text{crit}})^\beta \sqrt{1 - u_{\text{crit}}^2} = x. \quad (1.10)$$

The term  $u_{\text{crit}}$  in equation 1.10 cannot be isolated analytically. But as the final luminosity equation is implemented in Python, a numerical solution of  $u_{\text{crit}}$  can be found for every pos-

---

<sup>1</sup>In Owocki & Cohen (2001),  $u_x$  is defined as the minimum of  $u_o$  and  $u_x$ , but in this document, we use the two distinct labels.

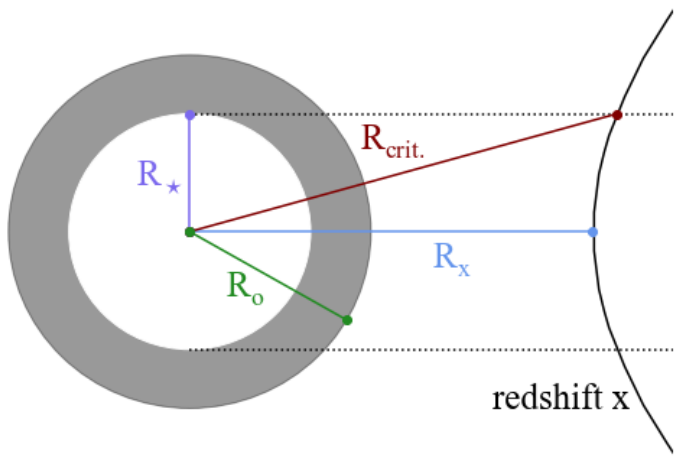


Figure 1.1: Visualization for the  $u_{\text{crit}} = R_*/R_{\text{crit}}$  derivation. The white circle represents the star, the grey ring represents the volumes below the onset radius  $R_o$  with no X-ray emission, and the grey dotted lines represent the boundary of wind occultation, assuming the observer is on the far left. The angle between  $R_{\text{crit}}$  and  $R_x$  is  $\pi - \theta$ .

itive  $x$ . We summarize our choice of integration bounds below,

$$u_{\text{bound}} = \begin{cases} \min(u_o, u_x), & x < 0, \\ \min(u_o, u_{\text{crit}}), & x \geq 0. \end{cases} \quad (1.11)$$

#### 1.2.4 THE LINE PROFILE MODEL

We finally have all the pieces we need to write down the line profile model. We notice that although equation 1.2 is a two-dimensional integral, it should essentially be one-dimensional as there exists a one-to-one correspondence between  $\theta$  and  $x$  at any given distance  $r$  away from the star. We therefore multiply  $\eta_x(r)$ , the emissivity at a certain radial velocity contour, with a Dirac delta function  $\delta(x' - x) = \delta(\theta' - \theta)$  that picks out the corresponding  $\theta$  at a given  $x$  (here  $x'$  and  $\theta'$  are dummy variables of integration). Substituting equations 1.3 and 1.11 into equation 1.2 and performing change of variables, we get

$$L_x = \frac{C\dot{M}^2}{2v_\infty^2 R_*} \int_0^\pi \int_0^{u_{\text{bound}}} \frac{f(u)}{(1-u)^{2\beta}} e^{-\tau(u,\theta')} \delta(\theta' - \theta) \sin \theta' du d\theta'. \quad (1.12)$$

We simplify equation 1.12 by differentiating the expression  $x' = -v(u) \cos \theta' / v_\infty = (1-u)^\beta \cos \theta'$ , which returns  $dx' = -(1-u)^\beta \sin \theta' d\theta'$ . So that at any fixed  $u$ ,

$$\int \delta(\theta' - \theta) \sin \theta' d\theta' = \int \frac{\delta(x' - x) dx'}{(1-u)^\beta} = \frac{1}{(1-u)^\beta}. \quad (1.13)$$

Substituting equation 1.13 together with equation 1.5 into equation 1.12, we arrive at the

final form of the line profile model,

$$L_x = \frac{C\dot{M}^2}{2v_\infty^2 R_*} \int_0^{u_{\text{bound}}} du \frac{f(u)}{(1-u)^{3\beta}} e^{-\tau_* \int_z^\infty \frac{R_* dz'}{(p^2 + z'^2)(1-R_*/\sqrt{p^2 + z'^2})^\beta}}, \quad (1.14)$$

where  $p$  is given by equation 1.8 and  $z$  is given by equation 1.7. Notice the result of the optical depth integral will be a function of  $u$  and  $x$ , and the full luminosity integral over  $u$  will thus lead to a line profile explicitly in terms of  $x$ .

Three important free parameters we study by fitting this model to the observed emission lines are  $R_o$ ,  $\tau_*$ , and the total line flux. Figure 1.2 shows how the wind features differ when  $R_o$  and  $\tau_*$  are varied. Notice that a bigger  $R_o$  leads to a broader line because the radii that only contribute to the emission with small absolute Doppler shifts (at wavelengths close to the center of the emission line) now do not emit any X-rays. A bigger  $\tau_*$  leads to more absorption especially in the red wing so the line is more asymmetric with the peak more blue-shifted in this case.

For  $\zeta$ Pup, previous analysis of the cycle 1 data showed an X-ray onset radius  $R_o \approx 1.5R_*$  and a mass-loss rate  $1.76_{-0.12}^{+0.13} \times 10^{-6} M_\odot \text{ yr}^{-1}$  (Cohen et al. 2014). We fit the same model to the new long cycle 19 dataset with an updated statistical method, aiming to put a tighter constraint on the mass-loss rate. While  $R_o$  remains approximately the same in the new dataset, we find, to our surprise, a significant increase in the mass-loss rate and the line flux, as we describe in the next section.

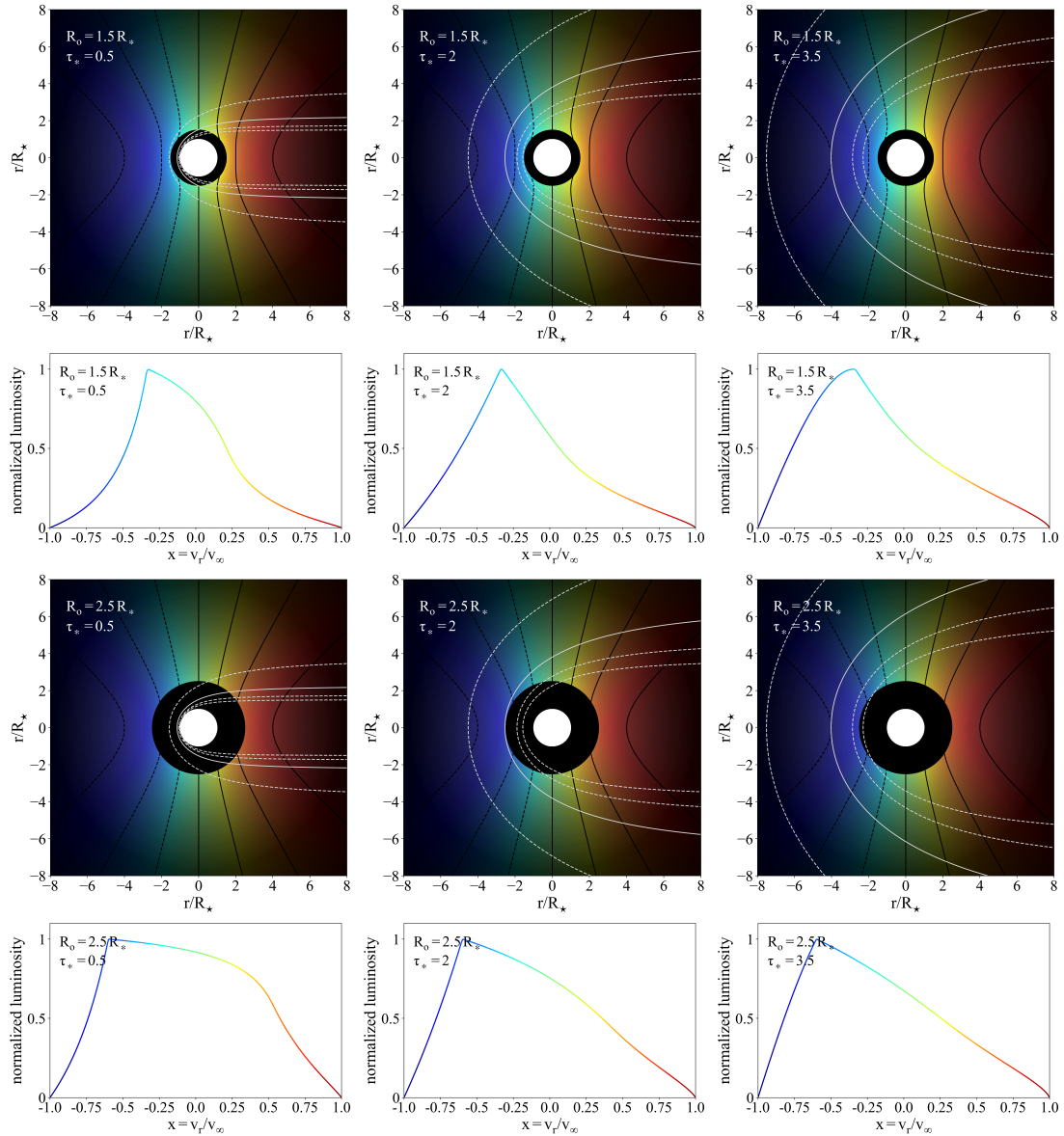


Figure 1.2: The first and third rows are spatial representations of the wind. The white circles represent the star, and the black rings represent the volumes below the onset radius  $R_o$  with no X-ray emission. Doppler shifts are shown as colored contours enhanced by black contour lines, optical depth as white contour lines (the solid white line shows where  $\tau = 1$ , the dotted lines are  $\tau = 0.5, 1.5$ , and  $2$ ), and X-ray emissivity as brightness. The observer is to the far left. Note  $\tau$  reaches infinity behind the star due to stellar occultation. The parameters  $R_o$  and  $\tau_*$  are specified on each plot. The second and fourth rows show normalized luminosity over scaled wavelength, the line profile, corresponding to the spatial model above each one.

Table 1.1: *Chandra* observing log for  $\zeta$ Pup

ObsID	Observation date and start time	Exposure time (ks)	Cycle number
640	2000 Mar 28 13:30:37	67.74	1
21113	2018 Jul 1 20:17:41	17.72	19
21112	2018 Jul 2 22:56:46	29.70	19
20156	2018 Jul 3 16:05:29	15.51	19
21114	2018 Jul 5 16:59:27	19.69	19
21111	2018 Jul 6 4:59:00	26.86	19
21115	2018 Jul 7 3:16:02	18.09	19
21116	2018 Jul 8 2:19:49	43.39	19
20158	2018 Jul 30 22:35:31	18.41	19
21661	2018 Aug 3 11:41:37	96.88	19
20157	2018 Aug 8 23:31:26	76.43	19
21659	2018 Aug 22 2:12:21	86.35	19
21673	2018 Aug 24 18:51:02	14.95	19
20154	2019 Jan 25 3:20:26	46.97	19
22049	2019 Feb 1 0:54:17	27.69	19
20155	2019 Jul 15 0:03:29	19.69	19
22278	2019 Jul 16 16:19:28	30.51	19
22279	2019 Jul 17 14:51:31	26.05	19
22280	2019 Jul 20 6:44:22	25.53	19
22281	2019 Jul 21 21:12:20	41.74	19
22076	2019 Aug 1 0:46:25	75.12	19
21898	2019 Aug 17 3:14:58	55.70	19
Total		812.98	19

### 1.3 OBSERVATIONS AND DATA

The *Chandra X-ray Observatory* carried out 21 separate pointings with a total of nearly 813 ks exposure on  $\zeta$ Pup during cycle 19, between 2018 and 2019. We include an observation log in Table 1.1, together with the long cycle 1 observation on  $\zeta$ Pup taken 18 years earlier.

*Chandra* has two high resolution spectrometers optimized for different energy ranges. We use data from the High-Energy Transmission Grating Spectrometer (HETGS) that covers the

energy range  $0.4 - 10.0$  keV, corresponding to a wavelength range of  $1.2 - 30$  Å (Canizares et al. 2005). The HETGS further consists of two sets of grating arrays: the Medium Energy Grating (MEG) designed to be sensitive in the energy range  $0.4 - 5.0$  keV ( $2.5 - 31$  Å) with a spectral resolution of  $\Delta\lambda(FWHM) = 0.023$  Å, and the High Energy Grating (HEG) sensitive in the range  $0.8 - 10.0$  keV ( $1.2 - 15$  Å) with a spectral resolution of  $\Delta\lambda(FWHM) = 0.012$  Å. Therefore, the spectral resolving power of HETGS, given by  $\lambda/\Delta\lambda$ , is up to 1000 over its effective wavelength range, and tends to be higher towards longer wavelengths<sup>2</sup>. This works in our favor, as at longer wavelengths, the wind opacity  $\kappa_\lambda$  is also higher and thus the asymmetry of the emission lines is more prominent.

Each MEG or HEG grating array consists of two first-order ( $m \pm 1$ ) spectra, dispersed on either side of the zeroth-order image (Canizares et al. 2005). We co-add the  $\pm 1$  spectra and perform our analysis on the 21 observations from cycle 19 with a total of 42 spectra. We do not combine these spectra, but rather analyze them simultaneously. A typical strong spectral line has approximately 500 counts (detected photons) per pixel at its peak wavelength, resulting in a signal-to-noise ratio of around 20.

The data were retrieved from the archive in November 2019 and reduced using standard CIAO pipeline (v. 4.11) with CALDB (v. 4.8.5) (Cohen et al. 2020). My research advisor David H. Cohen and our research collaborator M. Leutenegger (Goddard Spaceflight Center) performed data reduction on the first-order spectra for both the MEG and HEG, producing the pulse height amplitude files (PHAs) that record counts in each spectral channel - the spectra themselves, the response matrix files (RMFs) that map incident photon energy to channels based on the detectors' spectral resolution, and the auxiliary response files

---

<sup>2</sup>The Chandra Proposers' Observatory Guide contains detailed information about HETG in Chapter 8, available at <https://cxc.harvard.edu/proposer/POG/html/chap8.html>.

(ARFs) that record the effective area information. The effective area is the actual area of the telescope multiplied by the wavelength-dependent quantum efficiency, i.e., the fraction of incident photons that the detector can record. When analyzing the data, we do not subtract a background because it is extremely low.

We show the co-added ( $\pm 1$  order) MEG and HEG spectra in Figure 1.3, with the cycle 1 observation in the top panel and the combined cycle 19 observations in the middle panel. We also show the wavelength-dependent effective area in the bottom panel. The decrease in count rates in the cycle 19 data as compared to cycle 1 does not indicate an overall X-ray flux decrease in  $\zeta$ Pup, but instead can be attributed to the lowering of the effective area as a result of the continual build-up of contamination onto the filters of the X-ray imager ACIS used in conjunction with HETG (Marshall et al. 2004). As we show in the next two sections, the X-ray flux of  $\zeta$ Pup has actually increased by 13% from cycle 1 to cycle 19.

#### 1.4 MODEL FITTING

We identify 10 strong emission lines barely contaminated by surrounding spectral features (to be exact, 7 emission lines and 3 helium-like complexes listed in Table 1.2), and use XSPEC v. 12.9 (Dorman & Arnaud 2001) to analyze them in all 42 spectra simultaneously. We summarize our model fitting procedure here: (1) for each emission line, we model the continuum regions on either side of the line with a flat spectrum which is then taken into account in the line fitting, (2) we fit the line using the line profile model (equation 1.14)<sup>3</sup> with C-statistic minimization (Cash 1979), (3) we calculate a probability density distribution on  $\tau_*$  using  $\Delta C$  values, and (4) we finally derive the mass-loss rate from the ensemble of lines, using their

---

<sup>3</sup>To implement equation 1.14, we use the custom model *windprofile* within XSPEC, available at <https://heasarc.gsfc.nasa.gov/xanadu/xspec/models/windprof.html>.

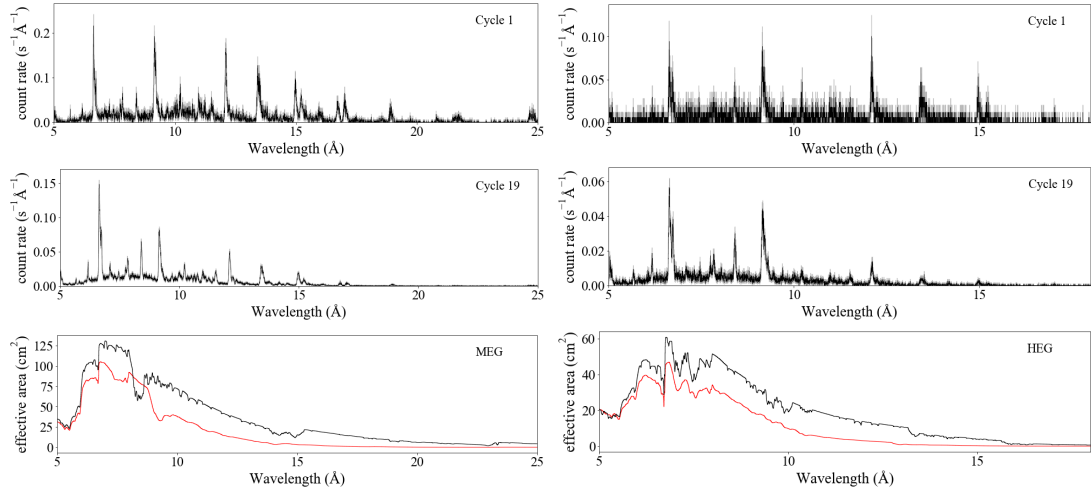


Figure 1.3: The co-added ( $\pm 1$  order) MEG (left) and HEG (right) spectra for cycle 1 are shown in the top panel, and those for the combined cyle 19 observations are shown in the middle panel. The bottom panel shows the effective area at the time of observation of MEG (left) and HEG (right), with cycle 1 in black and cycle 19 in red. The cycle 19 effective area is an average effective area weighted by the exposure time of each observation.

probability distributions and equation 1.6 with a model of the wavelength-dependent wind opacity.

We use forward modeling in steps (1) and (2). The line profile model is broadened through the response matrix files and multiplied by the effective area in the auxiliary response files before being fit to the emission line data.

#### 1.4.1 FITTING THE CONTINUUM REGIONS

For each emission line or line complex, we carefully choose its continuum regions on either side and model them with a flat power-law model (Cohen et al. 2010). The choices of these pseudo-continuum regions are listed in Table 1.2 and illustrated in Figure 1.8.

Table 1.2: Emission line pseudo-continuum regions

ion	line wavelength (Å)	continuum ranges (Å)
S xv	5.04, 5.07, 5.10	4.60-4.70, 4.76-4.95, 5.25-5.38, 5.43-5.60
Si xiv	6.18	6.05-6.09, 6.23-6.26, 6.33-6.40
Si xiii	6.65, 6.69, 6.74	6.30-6.50, 6.83-7.00
Mg xii	8.42	8.15-8.32, 8.64-8.80
Mg xi	9.17, 9.23, 9.31	8.60-8.80, 8.83-8.93, 9.00-9.04, 9.50-9.61
Ne x	10.24	9.73-9.93, 10.12-10.15, 10.345-10.39
Ne ix	11.54	11.32-11.39, 11.65-11.83
Ne x	12.13	11.94-12.03, 12.315-12.345
Fe xvii	15.01	14.63-14.90
Fe xvii	16.78	16.45-16.60, 16.89-16.90

The power-law model in XSPEC is defined as a function of photon energy<sup>4</sup>,

$$A(E) = KE^{-\alpha}, \quad (1.15)$$

where  $\alpha$  is a dimensionless photon index and  $K$  is the photon  $\text{keV}^{-1} \text{cm}^{-2} \text{s}^{-1}$  at 1 keV from the observed continuum. Since our data as well as the line profile model are in terms of wavelength, we perform change of variables to equation 1.15,

$$A(\lambda) = A(E) \frac{dE}{d\lambda} = K(bc)^{1-\alpha} \lambda^{\alpha-2} \equiv K' \lambda^{\alpha-2}. \quad (1.16)$$

Here  $K'$  is another constant in units of photon  $\text{\AA}^{-1} \text{cm}^{-2} \text{s}^{-1}$ . Based on our assumption of a flat power-law model in the wavelength-space, we set  $\alpha = 2$  and derive a value of  $K'$  for each line that represents the flux from the continuum. We show our best-fit continuum model for

---

<sup>4</sup>We use the custom model *pow* within XSPEC, available at <https://heasarc.gsfc.nasa.gov/xanadu/xspec/manual/node212.html>.

each line in Figure 1.8.

#### 1.4.2 FITTING THE EMISSION LINES

We fit the line profile model together with the power-law model (with fixed continuum flux determined from Section 1.4.1) to each of the 10 emission lines using C-statistics minimization (Cash 1979) via the *fit* task in XSPEC, and derive the best-fit  $\tau_*$ ,  $R_o$ , and the total line flux. When implementing equation 1.14, we adopt  $R_* = 18.9 R_\odot$  (Najarro et al. 2011) and  $v_\infty = 2250 \text{ km s}^{-1}$  (Puls et al. 2006), and set  $\beta = 1$  for typical O stars (Puls et al. 1996). We assume  $f(u)$  is a constant independent of  $u$  so that the emissivity  $\gamma$  is proportional to the wind density squared throughout the wind above the onset radius  $R_o$ . Thus the line flux that incorporates all the constants in front of the integral characterizes the strength of each emission line, and  $R_o$  and  $\tau_*$  control the shape of the emission line. The best-fit parameters are listed in Table 1.3, with error bars representing the 68% confidence intervals determined from each parameter’s probability distribution. We will present our method of determining these confidence limits in the next section. The corresponding best-fit models are shown in Figure 1.9.

To compare the cycle 19 emission line shapes, and eventually the mass-loss rate, with those from the cycle 1 data, we fit the cycle 1 observation with the same procedure and using the same continuum regions, and show the best-fit models in Figure 1.10. The refitted cycle 1 mass-loss rate result is within the 68% confidence interval of the published value  $1.76^{+0.13}_{-0.12} \times 10^{-6} M_\odot \text{ yr}^{-1}$  in Cohen et al. (2014), and the difference may be due to the different continuum choices, the lack of data and therefore analysis on the long-wavelength emission lines, and the newly developed statistical technique which we describe below.

Table 1.3: Emission line parameters

ion	lab wavelength (Å)	$\tau_*$	$R_o$ ( $R_*$ )	line flux ( $10^{-5}$ ph cm $^{-2}$ s $^{-1}$ )
S xv	5.04, 5.07, 5.10	$0.12^{+0.11}_{-0.08}$	$1.48^{+0.06}_{-0.05}$	$3.28^{+0.10}_{-0.10}$
Si xiv	6.18	$0.55^{+0.17}_{-0.14}$	$1.34^{+0.05}_{-0.05}$	$1.06^{+0.04}_{-0.04}$
Si xiii	6.65, 6.69, 6.74	$0.66^{+0.06}_{-0.05}$	$1.60^{+0.02}_{-0.02}$	$15.4^{+1}_{-1}$
Mg xii	8.42	$1.01^{+0.12}_{-0.11}$	$1.54^{+0.04}_{-0.04}$	$3.95^{+0.08}_{-0.08}$
Mg xi	9.17, 9.23, 9.31	$0.80^{+0.07}_{-0.07}$	$1.77^{+0.03}_{-0.03}$	$23.5^{+3}_{-3}$
Ne x	10.24	$2.59^{+0.19}_{-0.16}$	$1.01^{+0.41}_{-0.01}$	$4.13^{+0.15}_{-0.14}$
Ne ix	11.54	$1.54^{+0.29}_{-0.25}$	$1.73^{+0.10}_{-0.11}$	$7.44^{+0.25}_{-0.24}$
Ne x	12.13	$3.10^{+0.13}_{-0.12}$	$1.01^{+0.18}_{-0.01}$	$30.1^{+6}_{-5}$
Fe xvii	15.01	$2.40^{+0.34}_{-0.30}$	$1.87^{+0.14}_{-0.16}$	$60.2^{+1.5}_{-1.5}$
Fe xvii	16.78	$3.87^{+0.73}_{-0.65}$	$1.46^{+0.22}_{-0.46}$	$32.4^{+1.7}_{-1.8}$

#### 1.4.3 CALCULATING THE PROBABILITY DENSITY DISTRIBUTIONS ON $\tau_*$ AND $R_o$

In this section, we present our method of deriving a probability density distribution on each fit parameter ( $\tau_*$  or  $R_o$ ), and determining its 68% confidence interval based on the distribution.

From a given best-fit model with a minimized  $C$  value, we find the  $\Delta C$  values for a finely spaced grid of  $R_o$  and  $\tau_*$  around the best-fit, with the total line flux free to vary<sup>5</sup>. We transform  $\Delta C$  to probability density using the relationship  $P(x) = e^{-\Delta C(x)/2}$  (Cash 1979) and produce a probability density distribution for each  $x = \tau_*$  or  $R_o$ . The probability density distribution is thus a histogram with each point occupying a nonzero and equal bin width. Finding the probability of the  $x$  value lying in between two boundaries does not require an integration, but rather a simple addition of rectangular areas. Figure 1.4 shows some of the example distributions with determined 68% confidence intervals.

The 68% confidence boundaries ( $x_a, x_b$ ) are defined as two values of the same probability

<sup>5</sup>We use the *steppar* command in XSPEC to compute the  $\Delta C$  values.

$P_0$  around the mode that encloses 68% of the total area under the distribution. Each  $x_n$  with  $a < n < b$  (i.e., within the confidence interval) either has  $P(x) > P_0$  or is surrounded by some points  $(x'_a, x'_b)$  on both sides with  $a < a' < n$  and  $n < b' < b$  that has  $P(x_{a'}), P(x_{b'}) > P_0$ . For Gaussian distributions,  $(x_a, x_b) = (\mu - \sigma, \mu + \sigma)$  where  $\mu$  is the mode and  $\sigma$  is the standard deviation. This definition of confidence bounds works equally well for arbitrary distributions, such as the ones shown in Figure 1.4.

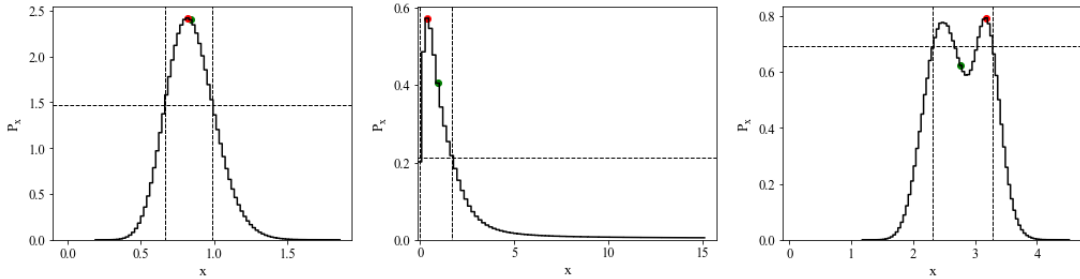


Figure 1.4: Three sample probability density distributions. The first one on the left is almost Gaussian, the second is skewed, and the third has more than one local maximum. The green dots show the medians and the red show the modes. The vertical dashed lines show the boundary of the 68% confidence region with identical likelihood indicated by the horizontal dashed line.

Using this method, we derive the 68% confidence bounds for each of the  $R_o$  and  $\tau_*$  in Table 1.3. The probability density distributions on line flux are nearly Gaussian, so their confidence bounds correspond to values with  $\Delta C = 1$ . To visualize how emission line shape changes from cycle 1 to cycle 19, we compare the Fe xvii line at 15.01 Å in Figure 1.5, together with the probability density distributions of  $\tau_*$  shown next to the profiles. Notice that the line is more asymmetric in cycle 19 than in cycle 1, agreeing with an overall rightward shift of the distribution.

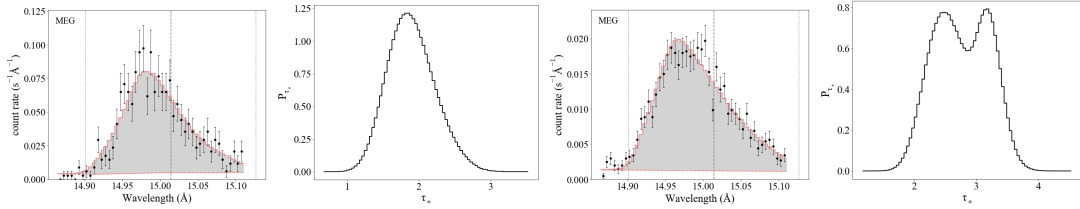


Figure 1.5: We compare the Fe XVII at 15.01 Å fit between cycle 1 (top panel) and cycle 19 (bottom panel). For the emission line plots (on the left), black data points represent the observed count rate, error bars represent 68 per cent uncertainties by Poisson distributions, and red histograms represent the best-fit emission line model. Panels next to the emissions lines show the corresponding  $\tau_*$  probability density distributions.

#### 1.4.4 DERIVING THE MASS-LOSS RATE

We fit equation 1.6, with an opacity model  $\kappa_\lambda$  assuming solar abundances (see Figure 2), to the ensemble of  $\tau_*$  probability density distributions to derive  $\zeta$ Pup's mass-loss rate. Given distributions  $P_1(\tau_*), P_2(\tau_*), \dots, P_{10}(\tau_*)$ , we derive a mass-loss rate probability density distribution from

$$P(\dot{M}) = P_1\left(\frac{\kappa_\lambda \dot{M}}{4\pi v_\infty R_*}\right) P_2\left(\frac{\kappa_\lambda \dot{M}}{4\pi v_\infty R_*}\right) \cdots P_{10}\left(\frac{\kappa_\lambda \dot{M}}{4\pi v_\infty R_*}\right). \quad (1.17)$$

The probabilities of the 10  $\tau_*$  at every mass-loss rate value are multiplied together to give an overall probability. The maximum of the distribution  $P(\dot{M})$  is the best-fit, or the most likely, mass-loss rate. A 68% confidence interval can be calculated given the distribution using the method presented in Section 1.4.3.

## 1.5 RESULTS

We show in Figure 1.6 our main result. Assuming  $R_* = 18.9 R_\odot$  and  $v_\infty = 2250 \text{ km s}^{-1}$ , the mass-loss rate derived from cycle 19 is  $\dot{M} = 2.47_{-0.09}^{+0.09} \times 10^{-6} M_\odot \text{ yr}^{-1}$ , which is a significant 40% increase from the published cycle 1 value,  $\dot{M} = 1.76_{-0.12}^{+0.13} \times 10^{-6} M_\odot \text{ yr}^{-1}$ . For the sake of comparison, we reanalyzed the cycle 1 data using the same 10 lines and found a mass-loss rate of  $1.88_{-0.14}^{+0.13} \times 10^{-6} M_\odot \text{ yr}^{-1}$ , which is within  $1\sigma$  of the old result. Since we adopt solar abundances for the opacity model  $\kappa_\lambda$  in both the cycle 1 and the cycle 19 analysis, the 40% increase of the mass-loss rate is still significant despite systematic errors in the absolute values. As shown in Figure 2, the solar opacity is slightly lower than a modeled opacity for  $\zeta$  Pup, which we explain in Chapter 3. But the two models are comparable below 17 Å.

Accompanying changes in the mass-loss rate, an average 13% emission line flux increase is observed, with the increase more noticeable at shorter wavelengths, where there is lower wind opacity. We show this result in Figure 1.7.

## 1.6 DISCUSSION

The simplest interpretation of the results we have presented is that the mass-loss rate increase causes the luminosity to increase by approximately the same amount because the fraction of the wind that is shock heated to temperatures high enough to emit X-rays stays constant. But due to the wavelength-dependent absorption, the amount of flux increase at shorter wavelengths is more than that at longer wavelengths.

Due to the 18-year time gap between cycle 1 and 19, we are uncertain whether this change is sudden, steady, or periodic. Thus, we also study observations with the *XMM-Newton*

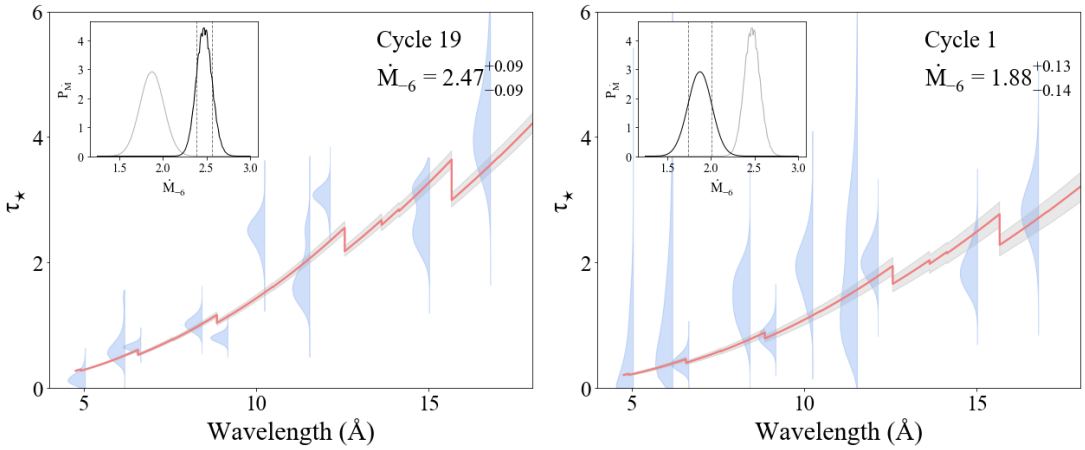


Figure 1.6: The cycle 19 (left panel) and cycle 1 (right panel) mass-loss rate fitting result derived from an ensemble of  $\tau_*$  probability distributions. The distribution at each spectral line wavelength is shown in light blue, extending out to  $\pm 5\sigma$  of the best-fit  $\tau_*$ . The red lines show the  $\tau_*$  model based on the best-fit mass-loss rate. The insets show the probability density distributions of the mass-loss rate with vertical dashed lines indicating the same 68% confidence regions indicated by the grey band surrounding the red, best-fit mass-loss rate.

X-ray telescope that span 20 years to explore the X-ray time-variability of  $\zeta$ Pup. Chapter 2 explores the change of  $\zeta$ Pup’s broadband X-ray flux over time, where we find a flux variation of 10% to 20% that seems random on years timescales. The *Chandra* cycle 19 observations were taken at some of the highest X-ray flux times during the 20 years and the *Chandra* cycle 1 observations were slightly prior to the start of the *XMM-Newton* observations, as we show in Chapter 2.

Since the wind characteristic optical depth  $\tau_*$  increases with wavelength (due to its dependence on the opacity  $\kappa_\lambda$ ) and is scaled by the mass-loss rate, a mass-loss rate can also be derived from a broadband analysis of X-ray absorption features in the *XMM-Newton* spectra. In Chapter 3, we use a thermal plasma emission model (Cohen et al. 2021) together with a broadband wind absorption model (Leutenegger et al. 2010) to fit the temperature distri-

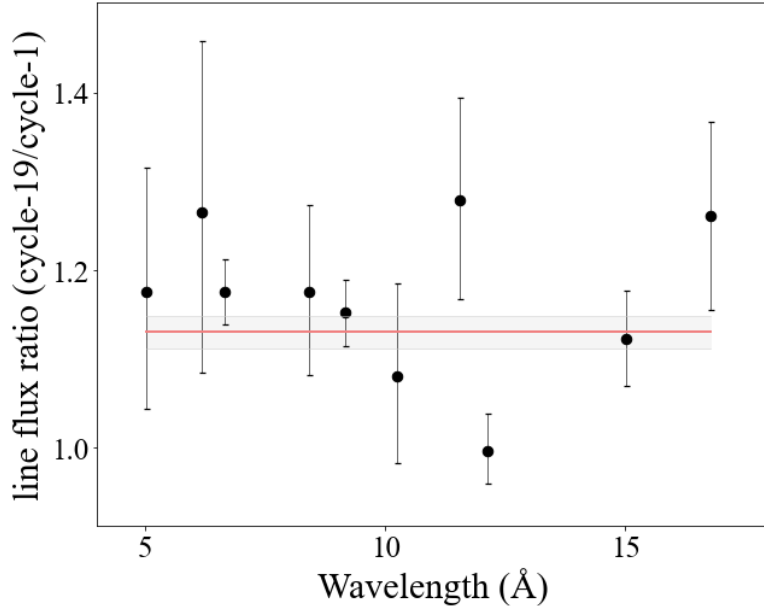


Figure 1.7: The cycle 19 to cycle 1 line flux ratios with error bars showing 68% confidence limits propagated from the cycle 19 and cycle 1 emission line fit results. The red line indicates a horizontal best-fit at 1.13, representing a 13% flux increase from cycle 1 to cycle 19. This increase has some modest wavelength dependence.

bution, ion abundances, and wind absorption column density closely related to the mass-loss rate. Preliminary analysis indicates that there exists a strong correlation between  $\zeta$ Pup's mass-loss rate and its emission measure, i.e., the total volume of X-ray emitting gas in the wind.

The X-ray emission line modeling is an effective diagnostic of the mass-loss rate since absorption scales with the wind density to the first order. Other diagnostics - UV, H $\alpha$ , and radio - that have been used to measure  $\zeta$ Pup's mass-loss rate are proportional to the wind density squared and sensitive to wind clumping, so their results cannot be reliably compared to the X-ray determined mass-loss rate at a 40% level (Puls et al. 2006). Additionally since the other diagnostics were implemented over a decade before the *Chandra* cycle 19 observations, their use in confirming our result is limited. The ongoing broadband analysis of the *XMM*-

*Newton* dataset will provide more information about how the mass-loss rate and the X-ray flux have changed over the past 20 years.

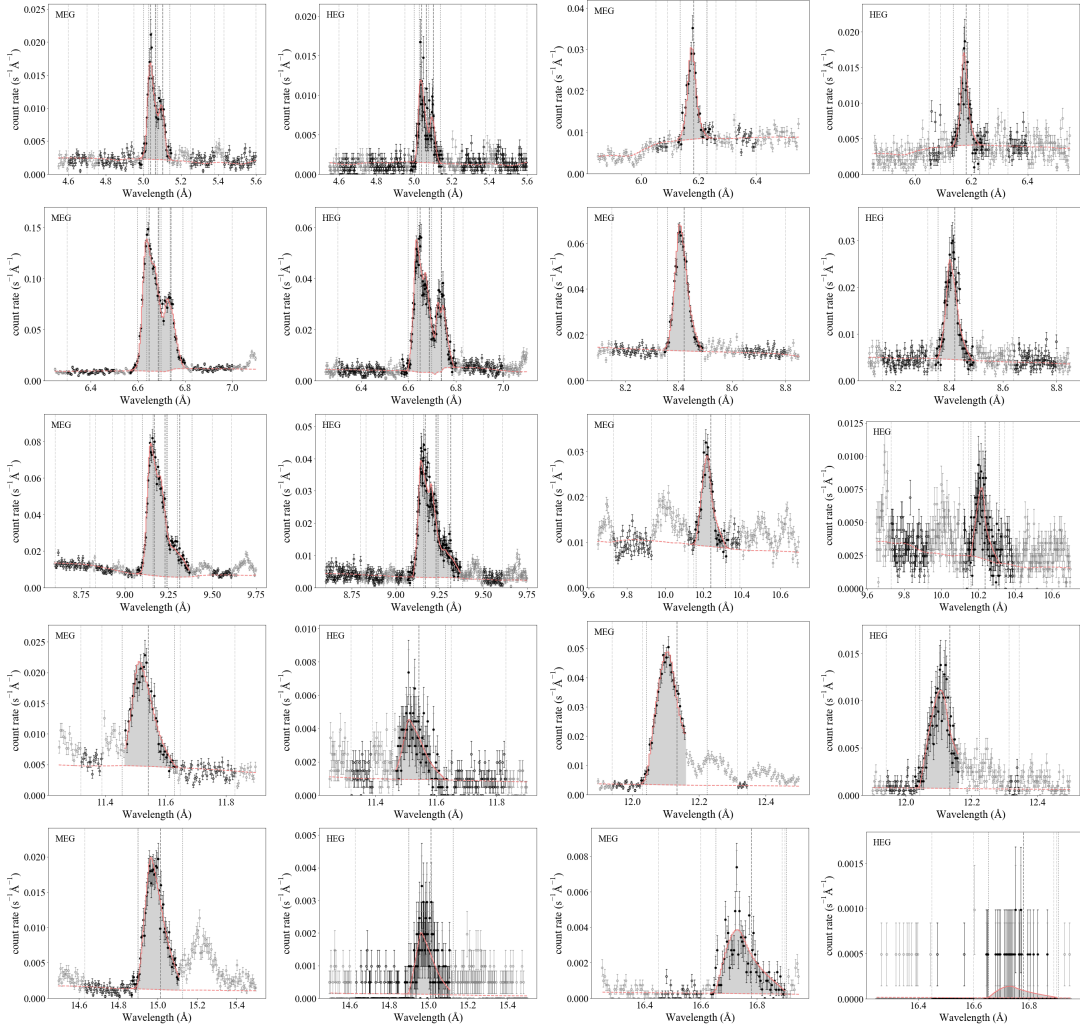


Figure 1.8: The emission lines and line complexes (in black solid dots) with their surrounding continuum regions (in black hollow dots bounded by vertical dotted lines) are shown in MEG and HEG pairs. The red dashed lines show the best-fit flat power-law model to the continuum, and the grey hollow dots show nearby emission lines that are excluded while fitting the continuum. Error bars on the data points represent 68% uncertainties by Poisson distributions. Data from the 21 new cycle 19 observations are combined in all figures.

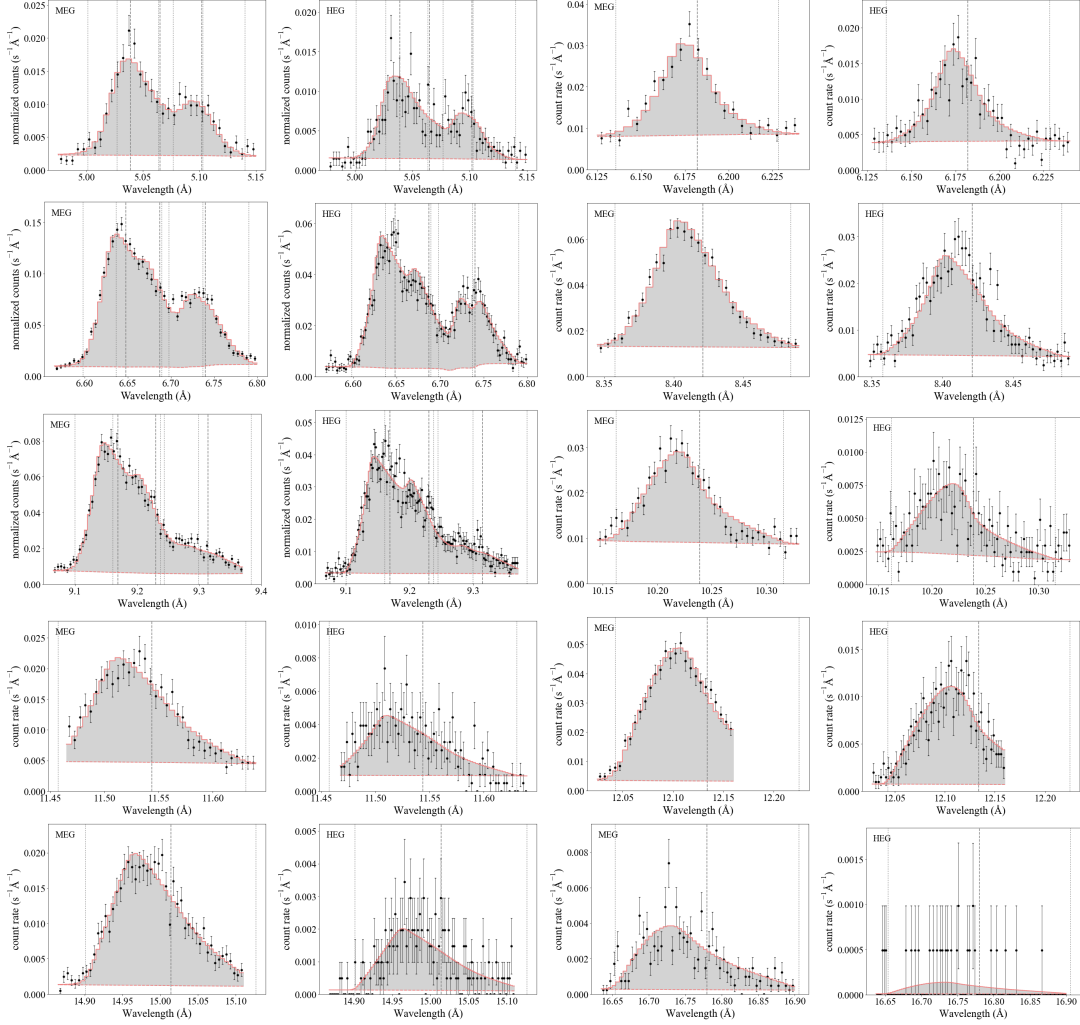


Figure 1.9: The emission lines (in black solid dots) and their best-fit line profile models (in red solid histograms) on top of the continuum models (in red dashed lines) are shown in MEG and HEG pairs. The continuum models are the same as in Figure 1.8. The dark grey vertical dashed line indicates the rest wavelength of each line, and the light grey vertical dashed lines indicate the Doppler shifted wavelengths corresponding to the wind terminal velocity of 2250 km s<sup>-1</sup>. Error bars on the data points represent 68% uncertainties by Poisson distributions. Data from the 21 new cycle 19 observations are combined in all figures.

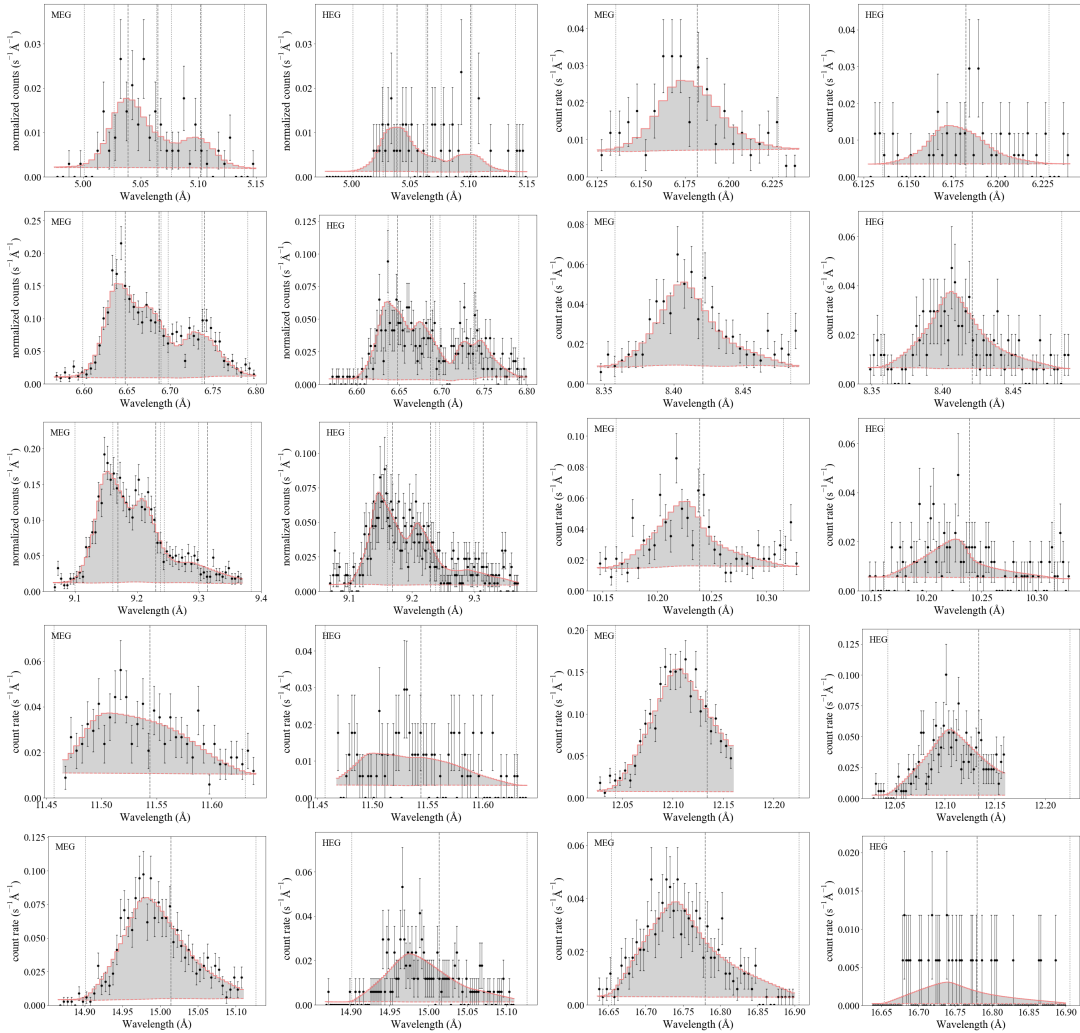


Figure 1.10: Same as Figure 1.9 but for cycle 1.

# 2

## Time Variability Analysis of the *XMM* Observations

### 2.1 INTRODUCTION

Emission line analysis of the *Chandra* data indicates a significant 40% mass-loss rate increase of  $\zeta$ Pup over the past 18 to 19 years, correlated with a wavelength-dependent X-ray line flux

increase of around 13% on average as described in Chapter 1. But due to the 18-year time gap between the *Chandra* cycle 1 and 19 data, we are uncertain whether this change is sudden, steady, or periodic. We therefore study data taken with the *XMM-Newton Observatory* that span 20 years, which fills in the gap between the *Chandra* observations, to further explore the X-ray time-variability of  $\zeta$  Pup.

We present the *XMM* data in Section 2.2, and our exact procedure of finding the total flux in each observation and generating the light curve in Section 2.3. Section 2.4 describes the statistics we apply to the light curve with the conclusion that no dominant X-ray periodicity of  $\zeta$  Pup is found. In Section 2.5, we discuss our results and summarize the identified periods and variability of  $\zeta$  Pup in the literature.

## 2.2 OBSERVATIONS AND DATA

The *XMM-Newton Observatory* carried out 36 observations of  $\zeta$  Pup from 2000 to 2021, using two identical Reflection Grating Spectrometers (RGS1 and RGS2) with a total effective exposure time of almost 3 Ms. The RGS instruments have high resolving power  $\lambda/\Delta\lambda(FWHM) = 100 - 500$ , and the spectra extend from 6 to 38 Å in the soft X-ray band with a photon-detection efficiency peak at around 15 Å (den Herder et al. 2001). Compared with the *Chandra* HETG spectra, the RGS spectra extend to longer wavelengths and thus reveal important spectral lines such as the N VII Lyman  $\alpha$  line at 24.8 Å and the N VI helium-like complex near 28.8 Å.

Out of the 36 *XMM* observations, four (ObsID 0159360401, 159361501, 561380801, and 561381201) are made for instrumental calibration and four (ObsID 0159360801, 0159361001, 0159361201, and 0159361401) are taken with zero exposure time and thus are empty. We

analyze the first order data of the remaining 28 observations, listed in Table 2.1. Research collaborator M. Leutenegger (Goddard Spaceflight Center) performed the data reduction using the standard pipeline in XMM SAS 11.0.0, producing the source and background spectra, the response, and the effective area files for each observation.

Various instrumental constraints, including photon scattering on the mirrors and the gratings as well as the proper alignment of the mirror and the grating responses, lead to small systematic shifts of the wavelength scale. These shifts skew the spectrum towards a certain direction with an rms deviation of  $\sigma = 8 \text{ m}\text{\AA}$ , mimicking a Doppler shift effect. The amount and direction of this shift is different for each observation, so we cannot effectively calibrate the data to eliminate this source of uncertainty (den Herder et al. 2001; Leutenegger et al. 2013). These systematic shifts of individual spectral lines obscure the degree of Doppler line shift and asymmetry, which is critical to the mass-loss rate measurement described in Chapter 1. So we cannot apply the same analysis to the RGS data.

However, we can still deduce useful information from the broadband X-ray emission and absorption properties of the RGS spectra. In this chapter, we calculate the model-independent total flux from each observation and perform analysis of the flux variability of  $\zeta$  Pup, which is expected to correlate with the star's mass-loss rate variability. In the next chapter, we fit the spectra with a thermal plasma emission model (Cohen et al. 2021) together with a broadband wind absorption model (Leutenegger et al. 2010) as an independent diagnostic of the mass-loss rate.

Table 2.1: *XMM-Newton* observing log for  $\zeta$ Pup

ObsID	Observation date and start time	RGS1 exposure time (ks)	RGS2 exposure time (ks)
0095810301	2000 Jun 8 01:33:58	52.55	50.90
0095810401	2000 Oct 15 01:05:37	39.88	38.53
0157160401	2002 Nov 10 17:55:40	41.55	40.22
0157160501	2002 Nov 17 01:05:00	38.74	38.73
0157160901	2002 Nov 24 14:27:37	43.50	43.50
0157161101	2002 Dec 15 00:08:42	27.80	27.76
0159360101	2003 May 30 09:29:28	66.24	66.23
0163360201	2003 Dec 6 18:11:07	41.62	41.61
0159360301	2004 Apr 12 08:48:09	26.89	26.88
0159360501	2005 Apr 16 05:52:48	34.52	34.51
0159360701	2005 Oct 15 04:11:24	23.49	23.43
0159360901	2005 Dec 3 17:02:34	48.27	48.24
0159361101	2006 Apr 17 14:15:05	42.46	42.43
0414400101	2007 Apr 9 14:05:18	58.34	58.32
0159361301	2008 Oct 13 16:10:03	61.16	61.23
0561380101	2009 Nov 3 21:29:24	64.06	64.15
0561380201	2010 Oct 7 12:37:17	76.65	76.72
0561380301	2011 Nov 9 19:47:26	63.70	63.75
0561380501	2012 Nov 2 17:54:41	60.47	60.48
0561380601	2013 Oct 8 01:51:06	67.56	67.56
0561380701	2015 Apr 28 00:24:33	55.01	55.04
0561380901	2016 Apr 4 22:04:18	67.90	67.98
0561381001	2017 Apr 4 04:35:42	59.22	59.27
0561381101	2018 Apr 16 19:20:51	64.45	64.52
0810870101	2019 Apr 14 13:47:55	86.13	86.24
0810870201	2019 Nov 5 23:27:37	43.75	43.78
0810871301	2020 Apr 15 18:35:14	64.24	64.32
0810871401	2021 Apr 17 09:26:22	65.68	65.76
Total		1485.83	1482.09

## 2.3 FLUX INTEGRATION

The RGS spectra are essentially measurements of count rate ( $s^{-1} \text{Å}^{-1}$ ) as a function of wavelength (Å). At each wavelength, we recover the flux from the count rate by dividing it by the effective area, which is the actual area of the telescope multiplied by the wavelength-dependent quantum efficiency, i.e. the fraction of incident photons that can be recorded by the detector. The effective area as a function of wavelength is different for each observation, and may drop to zero at certain wavelength regions in some later observations as the detectors degrade. For example, photons with wavelength from approximately 11 Å to 14 Å were detected in the first observation RGS1 spectrum, but not in the second or later RGS1 spectra (Figure 2.1) due to electronic problems in the CCD assembly RGS1 CCD7. Similar problems also occurred in RGS2 CCD4, corresponding to wavelengths from approximately 20 Å to 24 Å. Consistent narrow drops of the effective area curves are the result of instrumental absorption due to contamination layers on top of the CCDs<sup>1</sup>. Notice that the wavelength regions with zero effective area are also expected to have zero count rate.

To fairly compare the X-ray flux of  $\zeta$  Pup among the observations, we identify the wavelength regions with nonzero effective area in all observations and integrate the flux over these common regions, shaded in blue in Figure 2.1. We do not integrate across the whole spectrum because this will bias against observations, especially the later ones, with more zero-effective-area wavelength gaps. The common wavelength regions for the RGS1 and the RGS2 spectra are identified separately and displayed in Figure 2.2 (also in Figure 2.1 for RGS1), so we do not anticipate the RGS1 and RGS2 integrated fluxes to be comparable. Rather, any differ-

---

<sup>1</sup>The XMM-Newton Calibration Technical Note contains detailed information about CCD detector sensitivity, available at <http://xmmweb.esac.esa.int/docs/documents/CAL-TN-0030.pdf>.

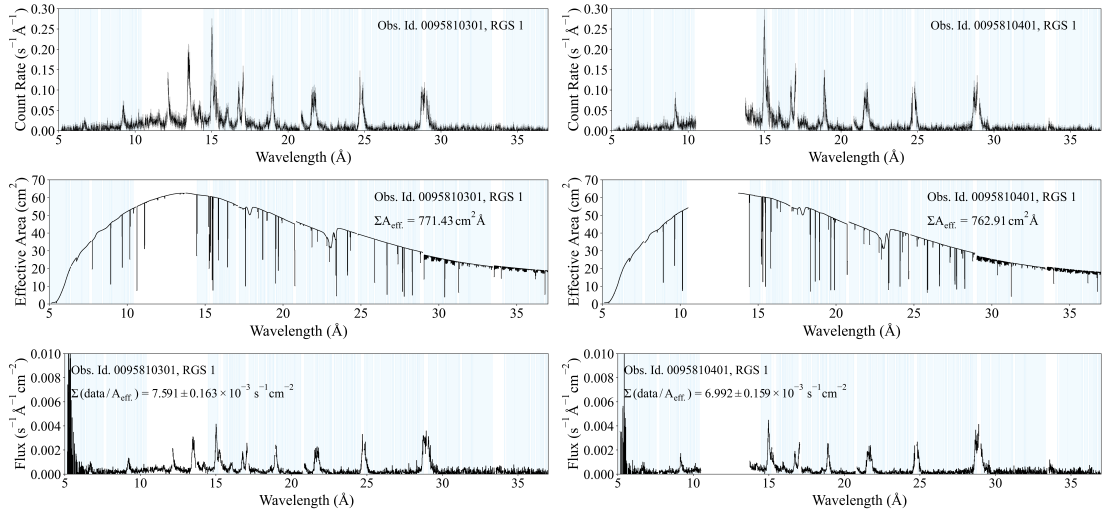


Figure 2.1: Count rate (top panel), effective area (middle panel), and flux (bottom panel which is the count rate divided by the effective area) of the first and second *XMM-Newton* observations (ObsID 0095810301, 0095810401). Blue-shaded regions are common wavelength regions with nonzero effective area in all observations, across which we integrate to get the total effective area  $\sum A_{\text{eff.}}$  and the total flux  $\sum (\text{data}/A_{\text{eff.}})$ . We show only the RGS1 spectra for this demonstration.

ences in flux between RGS1 and RGS2 could be attributed to the different effective areas between the two (which would lead to different common wavelength regions) instead of different numbers of incident photons.

We also break down the data into energy bands: soft band S = 0.3 – 0.6 keV, medium band M = 0.6 – 1.2 keV, hard band H = 1.2 – 4.0 keV, and Berghöfer band = 0.9 – 2 keV (Nazé et al. 2013; Berghofer et al. 1996). The Berghöfer band roughly matches the cycle 19 *Chandra* HETG effective wavelength range. The integrated fluxes over these bands are listed in Table 2.2 and Table 2.3, with errors in the subscript solely from the Poisson errors of the count rates.

Table 2.2: Wavelength-integrated fluxes ( $10^{-2} \text{ s}^{-1} \text{ cm}^{-2}$ ) over S, M, H energy bands

ObsID	0.3 – 0.6 keV flux		0.6 – 1.2 keV flux		1.2 – 4.0 keV flux	
	RGS <sub>1</sub>	RGS <sub>2</sub>	RGS <sub>1</sub>	RGS <sub>2</sub>	RGS <sub>1</sub>	RGS <sub>2</sub>
0095810301	0.336 <sub>0.005</sub>	0.302 <sub>0.004</sub>	0.210 <sub>0.003</sub>	0.478 <sub>0.004</sub>	0.214 <sub>0.015</sub>	0.280 <sub>0.023</sub>
0095810401	0.324 <sub>0.005</sub>	0.329 <sub>0.005</sub>	0.205 <sub>0.003</sub>	0.502 <sub>0.005</sub>	0.170 <sub>0.015</sub>	0.183 <sub>0.018</sub>
0157160401	0.335 <sub>0.006</sub>	0.318 <sub>0.005</sub>	0.216 <sub>0.003</sub>	0.501 <sub>0.005</sub>	0.139 <sub>0.013</sub>	0.191 <sub>0.019</sub>
0157160501	0.322 <sub>0.006</sub>	0.331 <sub>0.006</sub>	0.217 <sub>0.003</sub>	0.496 <sub>0.005</sub>	0.173 <sub>0.014</sub>	0.283 <sub>0.026</sub>
0157160901	0.323 <sub>0.005</sub>	0.323 <sub>0.005</sub>	0.223 <sub>0.003</sub>	0.515 <sub>0.004</sub>	0.153 <sub>0.012</sub>	0.181 <sub>0.017</sub>
0157161101	0.331 <sub>0.007</sub>	0.299 <sub>0.006</sub>	0.221 <sub>0.004</sub>	0.489 <sub>0.005</sub>	0.159 <sub>0.016</sub>	0.212 <sub>0.023</sub>
0159360101	0.354 <sub>0.005</sub>	0.308 <sub>0.004</sub>	0.218 <sub>0.003</sub>	0.487 <sub>0.004</sub>	0.156 <sub>0.010</sub>	0.192 <sub>0.015</sub>
0163360201	0.359 <sub>0.007</sub>	0.333 <sub>0.007</sub>	0.212 <sub>0.004</sub>	0.461 <sub>0.005</sub>	0.090 <sub>0.003</sub>	0.099 <sub>0.005</sub>
0159360301	0.373 <sub>0.008</sub>	0.332 <sub>0.007</sub>	0.220 <sub>0.004</sub>	0.486 <sub>0.006</sub>	0.267 <sub>0.026</sub>	0.373 <sub>0.037</sub>
0159360501	0.327 <sub>0.006</sub>	0.301 <sub>0.006</sub>	0.200 <sub>0.003</sub>	0.437 <sub>0.005</sub>	0.192 <sub>0.017</sub>	0.247 <sub>0.025</sub>
0159360701	0.401 <sub>0.009</sub>	0.397 <sub>0.009</sub>	0.218 <sub>0.004</sub>	0.519 <sub>0.006</sub>	0.377 <sub>0.039</sub>	0.600 <sub>0.056</sub>
0159360901	0.338 <sub>0.006</sub>	0.314 <sub>0.005</sub>	0.218 <sub>0.003</sub>	0.488 <sub>0.004</sub>	0.158 <sub>0.014</sub>	0.209 <sub>0.018</sub>
0159361101	0.342 <sub>0.006</sub>	0.297 <sub>0.005</sub>	0.208 <sub>0.003</sub>	0.440 <sub>0.004</sub>	0.185 <sub>0.017</sub>	0.204 <sub>0.020</sub>
0414400101	0.320 <sub>0.005</sub>	0.287 <sub>0.005</sub>	0.211 <sub>0.003</sub>	0.454 <sub>0.004</sub>	0.151 <sub>0.011</sub>	0.251 <sub>0.020</sub>
0159361301	0.305 <sub>0.005</sub>	0.281 <sub>0.005</sub>	0.211 <sub>0.003</sub>	0.470 <sub>0.004</sub>	0.142 <sub>0.009</sub>	0.167 <sub>0.014</sub>
0561380101	0.291 <sub>0.005</sub>	0.282 <sub>0.005</sub>	0.197 <sub>0.002</sub>	0.437 <sub>0.003</sub>	0.116 <sub>0.008</sub>	0.155 <sub>0.013</sub>
0561380201	0.305 <sub>0.004</sub>	0.285 <sub>0.004</sub>	0.196 <sub>0.002</sub>	0.448 <sub>0.003</sub>	0.131 <sub>0.008</sub>	0.202 <sub>0.015</sub>
0561380301	0.330 <sub>0.005</sub>	0.290 <sub>0.005</sub>	0.217 <sub>0.003</sub>	0.489 <sub>0.004</sub>	0.138 <sub>0.010</sub>	0.166 <sub>0.015</sub>
0561380501	0.294 <sub>0.005</sub>	0.271 <sub>0.005</sub>	0.195 <sub>0.002</sub>	0.444 <sub>0.004</sub>	0.134 <sub>0.009</sub>	0.160 <sub>0.013</sub>
0561380601	0.290 <sub>0.005</sub>	0.275 <sub>0.004</sub>	0.195 <sub>0.002</sub>	0.447 <sub>0.003</sub>	0.130 <sub>0.009</sub>	0.127 <sub>0.010</sub>
0561380701	0.316 <sub>0.005</sub>	0.268 <sub>0.005</sub>	0.202 <sub>0.003</sub>	0.445 <sub>0.004</sub>	0.153 <sub>0.011</sub>	0.245 <sub>0.020</sub>
0561380901	0.298 <sub>0.005</sub>	0.277 <sub>0.005</sub>	0.205 <sub>0.002</sub>	0.446 <sub>0.003</sub>	0.133 <sub>0.008</sub>	0.161 <sub>0.012</sub>
0561381001	0.290 <sub>0.005</sub>	0.261 <sub>0.005</sub>	0.197 <sub>0.003</sub>	0.457 <sub>0.004</sub>	0.129 <sub>0.008</sub>	0.150 <sub>0.013</sub>
0561381101	0.294 <sub>0.005</sub>	0.258 <sub>0.004</sub>	0.214 <sub>0.003</sub>	0.466 <sub>0.004</sub>	0.155 <sub>0.011</sub>	0.148 <sub>0.011</sub>
0810870101	0.298 <sub>0.004</sub>	0.259 <sub>0.004</sub>	0.220 <sub>0.002</sub>	0.489 <sub>0.003</sub>	0.136 <sub>0.007</sub>	0.159 <sub>0.011</sub>
0810870201	0.324 <sub>0.006</sub>	0.267 <sub>0.006</sub>	0.213 <sub>0.003</sub>	0.474 <sub>0.004</sub>	0.170 <sub>0.014</sub>	0.184 <sub>0.016</sub>
0810871301	0.305 <sub>0.005</sub>	0.266 <sub>0.005</sub>	0.220 <sub>0.003</sub>	0.488 <sub>0.004</sub>	0.149 <sub>0.009</sub>	0.189 <sub>0.015</sub>
0810871401	0.308 <sub>0.005</sub>	0.258 <sub>0.004</sub>	0.216 <sub>0.003</sub>	0.482 <sub>0.004</sub>	0.146 <sub>0.009</sub>	0.160 <sub>0.013</sub>

Table 2.3: Wavelength-integrated flux ( $10^{-2} \text{ s}^{-1} \text{ cm}^{-2}$ ) over Berghöfer energy band and total integrated flux

ObsID	0.9 – 2 keV flux		total flux	
	RGS <sub>1</sub>	RGS <sub>2</sub>	RGS <sub>1</sub>	RGS <sub>2</sub>
o095810301	0.091 <sub>0.002</sub>	0.245 <sub>0.003</sub>	0.76 <sub>0.02</sub>	1.06 <sub>0.02</sub>
o095810401	0.091 <sub>0.002</sub>	0.262 <sub>0.004</sub>	0.70 <sub>0.02</sub>	1.01 <sub>0.02</sub>
o157160401	0.084 <sub>0.002</sub>	0.263 <sub>0.004</sub>	0.69 <sub>0.01</sub>	1.01 <sub>0.02</sub>
o157160501	0.085 <sub>0.002</sub>	0.262 <sub>0.004</sub>	0.71 <sub>0.02</sub>	1.11 <sub>0.03</sub>
o157160901	0.091 <sub>0.002</sub>	0.265 <sub>0.003</sub>	0.70 <sub>0.01</sub>	1.02 <sub>0.02</sub>
o157161101	0.085 <sub>0.003</sub>	0.261 <sub>0.004</sub>	0.71 <sub>0.02</sub>	1.00 <sub>0.02</sub>
o159360101	0.081 <sub>0.002</sub>	0.245 <sub>0.003</sub>	0.73 <sub>0.01</sub>	0.99 <sub>0.02</sub>
o163360201	0.086 <sub>0.003</sub>	0.237 <sub>0.004</sub>	0.66 <sub>0.01</sub>	0.89 <sub>0.01</sub>
o159360301	0.086 <sub>0.003</sub>	0.248 <sub>0.004</sub>	0.86 <sub>0.03</sub>	1.19 <sub>0.04</sub>
o159360501	0.086 <sub>0.003</sub>	0.235 <sub>0.004</sub>	0.72 <sub>0.02</sub>	0.98 <sub>0.03</sub>
o159360701	0.089 <sub>0.003</sub>	0.267 <sub>0.005</sub>	1.00 <sub>0.04</sub>	1.52 <sub>0.06</sub>
o159360901	0.081 <sub>0.002</sub>	0.261 <sub>0.003</sub>	0.71 <sub>0.02</sub>	1.01 <sub>0.02</sub>
o159361101	0.078 <sub>0.002</sub>	0.227 <sub>0.003</sub>	0.73 <sub>0.02</sub>	0.94 <sub>0.02</sub>
o414400101	0.083 <sub>0.002</sub>	0.237 <sub>0.003</sub>	0.68 <sub>0.01</sub>	0.99 <sub>0.02</sub>
o159361301	0.081 <sub>0.002</sub>	0.236 <sub>0.003</sub>	0.66 <sub>0.01</sub>	0.92 <sub>0.01</sub>
o561380101	0.069 <sub>0.002</sub>	0.224 <sub>0.003</sub>	0.60 <sub>0.01</sub>	0.87 <sub>0.01</sub>
o561380201	0.081 <sub>0.002</sub>	0.231 <sub>0.002</sub>	0.63 <sub>0.01</sub>	0.93 <sub>0.02</sub>
o561380301	0.081 <sub>0.002</sub>	0.254 <sub>0.003</sub>	0.68 <sub>0.01</sub>	0.95 <sub>0.02</sub>
o561380501	0.079 <sub>0.002</sub>	0.237 <sub>0.003</sub>	0.62 <sub>0.01</sub>	0.87 <sub>0.01</sub>
o561380601	0.077 <sub>0.002</sub>	0.233 <sub>0.003</sub>	0.62 <sub>0.01</sub>	0.85 <sub>0.01</sub>
o561380701	0.083 <sub>0.002</sub>	0.227 <sub>0.003</sub>	0.67 <sub>0.01</sub>	0.96 <sub>0.02</sub>
o561380901	0.081 <sub>0.002</sub>	0.238 <sub>0.003</sub>	0.64 <sub>0.01</sub>	0.89 <sub>0.01</sub>
o561381001	0.080 <sub>0.002</sub>	0.237 <sub>0.003</sub>	0.62 <sub>0.01</sub>	0.87 <sub>0.01</sub>
o561381101	0.088 <sub>0.002</sub>	0.249 <sub>0.003</sub>	0.66 <sub>0.01</sub>	0.87 <sub>0.01</sub>
o810870101	0.089 <sub>0.002</sub>	0.256 <sub>0.002</sub>	0.65 <sub>0.01</sub>	0.91 <sub>0.01</sub>
o810870201	0.093 <sub>0.002</sub>	0.257 <sub>0.003</sub>	0.71 <sub>0.02</sub>	0.92 <sub>0.02</sub>
o810871301	0.086 <sub>0.002</sub>	0.257 <sub>0.003</sub>	0.67 <sub>0.01</sub>	0.94 <sub>0.02</sub>
o810871401	0.094 <sub>0.002</sub>	0.257 <sub>0.003</sub>	0.67 <sub>0.01</sub>	0.90 <sub>0.01</sub>

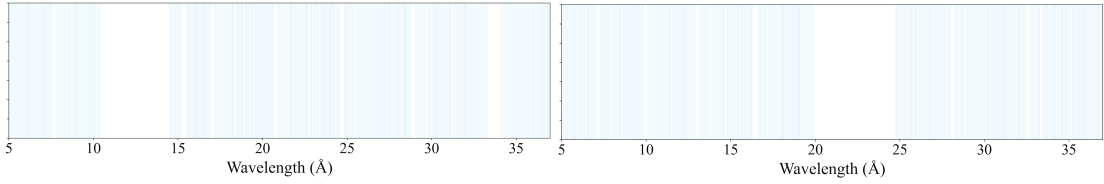


Figure 2.2: Blue-shaded regions show the common wavelengths covered by all observations, across which we integrate to get the total flux. RGS1 wavelength coverage is shown on the left, and RGS2 on the right. The RGS1 regions are identical to the ones in Figure 2.1.

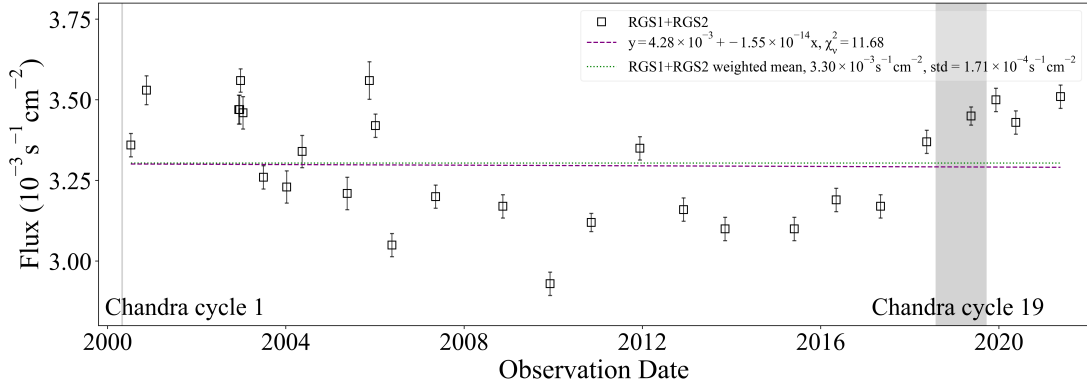


Figure 2.3: Total RGS1+RGS2 X-ray flux for each of the 28 *XMM-Newton* observations, integrated from 0.9 to 2 keV but only over the wavelength intervals for which there is data in each observation, i.e., the blue bands in Figure 2.2. Grey bands indicate the periods when the *Chandra* cycle 1 and cycle 19 data were taken. The weighted mean of RGS1+RGS2 flux is shown in green dotted line, and the linear fit is shown in purple dashed line.

#### 2.4 STATISTICS AND PERIOD SEARCH RESULTS

To analyze the X-ray flux variation over time so that we can relate it to the variations observed in the *Chandra* data, we focus on the fluxes integrated across the Berghöfer band. We add the RGS1 and RGS2 fluxes for each observation and plot them versus the observation date in Figure 2.3. We compute a mean RGS1+RGS2 flux weighted by each observation's exposure time of  $3.30 \times 10^{-3}$  counts  $s^{-1} cm^{-2}$ , with a standard deviation of  $1.71 \times 10^{-4} s^{-1} cm^{-2}$

representing roughly 5% fluctuation from the weighted mean. We then fit the fluxes with a linear model and found an almost zero slope with a reduced chi-squared of 11.68. This high reduced chi-squared value indicates that variability is significant. The weighted mean and the linear model are also shown in Figure 2.3.

#### 2.4.1 KUIPER STATISTICS

We use Kuiper's test (Paltani 2004), a variant Kolmogorov-Smirnov's (KS) test, to search for possible year-timescale periodicities in RGS1 and RGS2 data separately. Kuiper's test is a statistic that assesses the goodness of fit of a model distribution to the cumulative probability distribution of a set of data. Because of the uneven time gaps in between the *XMM* observations, the Kuiper's test is especially useful in this study as it makes no assumption about the sampling or binning of the data set. We explain the mathematical form of the Kuiper's test and how it is adjusted to analyze our data below.

Let  $\{x_i\}$ ,  $i = 1, \dots, N$ , be the set of sample data with  $a \leq x_i \leq b$ . We define the empirical cumulative distribution  $S(x) = \#(x_i \leq x)/N$ , which is the number of data points less or equal to  $x$  divided by the total number of data points  $N$ . Assume the data follow a distribution  $\varphi(x)$  with cumulative distribution  $\Phi(x) = \int_a^x \varphi(x') dx'$ , the KS test is defined as the maximum deviation between the postulated and the empirical cumulative distributions. The Kuiper variant sums the maximum deviations between the distributions in both the negative and the positive directions, making it a more suitable test for periodic variability. The mathematical expression of the Kuiper statistic is

$$V^\Phi(\{x_i\}) = \max_{a \leq x \leq b} (S(x) - \Phi(x)) + \max_{a \leq x \leq b} (\Phi(x) - S(x)). \quad (2.1)$$

To apply Kuiper's test to our data, we make the following assumptions: (1) the RGS<sub>1</sub>+RGS<sub>2</sub> flux scales as the number of photons arriving at each observation date, and (2) the postulated distribution  $\varphi(x)$  is a constant distribution with no periodicity, so that  $\Phi(x)$  is roughly linear with minor variations due to the uneven sampling of the observations. For each tested frequency  $f_0$  and period  $P_0 = 1/f_0$ , we phase-fold the 28 observation dates  $\{t_i\}$  with their corresponding RGS<sub>1</sub> or RGS<sub>2</sub> fluxes  $\{b_i\}$  using the function

$$\psi_i(f_0) = \text{Frac} \left( \frac{t_i - t_0}{P_0} \right), \quad i = 1, \dots, 28, \quad (2.2)$$

where  $\text{Frac}(x)$  returns the fractional part of  $x$  (the phase) and  $t_0$  is an arbitrary zero point that does not impact the calculation of the Kuiper statistic. We thus define the empirical cumulative distribution  $S(\psi)$  and the postulated constant distribution  $U(\psi)$  as

$$S(\psi) = \frac{\#(\psi_i \leq \psi) \times b_i}{\sum_{i=1}^{28} b_i}, \quad (2.3)$$

$$U(\psi) = \int_{t_0}^{\psi+t_0} d\psi' = \psi. \quad (2.4)$$

The Kuiper statistic is then

$$V^U(\psi_i(f_0)) = \max_{t_0 \leq \psi_i \leq t_0 + P_0} (S(\psi) - U(\psi)) + \max_{t_0 \leq \psi_i \leq t_0 + P_0} (U(\psi) - S(\psi)). \quad (2.5)$$

Therefore, a high Kuiper statistic at a given frequency indicates low correlation between the data and the postulated distribution, thus a high likelihood of that frequency.

We search for roughly year-timescale periods from  $f_0 = 1.05 \times 10^{-9} \text{ s}^{-1}$  to  $3.5 \times 10^{-8} \text{ s}^{-1}$ ,

corresponding to around 0.9 to 30 years. We cannot properly transform the Kuiper statistic to an absolute statistical significance due to the adjustments we make to apply the Kuiper's test to our data. Thus we present the relative significance of these frequencies in the left panel of Figure 2.4. No noticeable peaks on the Kuiper statistics are found except for the rapid increase on the low-frequency side, corresponding to a period longer than the span of the data.

We further examine narrow frequency ranges near local Kuiper statistic peaks, as shown in the left panel of Figure 2.4. To test these possible periods, we fit a sine wave model to the RGS1 and RGS2 data, allowing the test frequencies to fluctuate within each frequency range and evaluating the fits with chi-squared statistics. The results are in the right panel of Figure 2.4. We also show individual sine wave fits with fixed frequencies at 0.21, 2.13, and  $3.17 \times 10^{-8} \text{ s}^{-1}$  (around 15.1, 1.5, and 1.0 years) in Figure 2.5. The high reduced chi-squared statistics for all peak frequencies, in both RGS1 and RGS2, confirm that the *XMM* observations do not demonstrate clear periodicity.

## 2.5 DISCUSSION AND CONCLUSIONS

This model-independent analysis of the RGS data suggests that the X-ray flux variation from the wind of  $\zeta$  Pup is random, with a standard deviation of around 5% from the weighted mean and with no overall increasing or decreasing long-term trend. This long observing campaign with *XMM* reveals that the cycle 19 *Chandra* observations were indeed taken at some of the highest X-ray flux times during the 20 years, with observation 0810870101 (2019 Apr 14) being within the top 33% of the 28 observations and having a flux that is 4.5% above the weighted mean. While a 19% flux difference exists between observations (ObsID

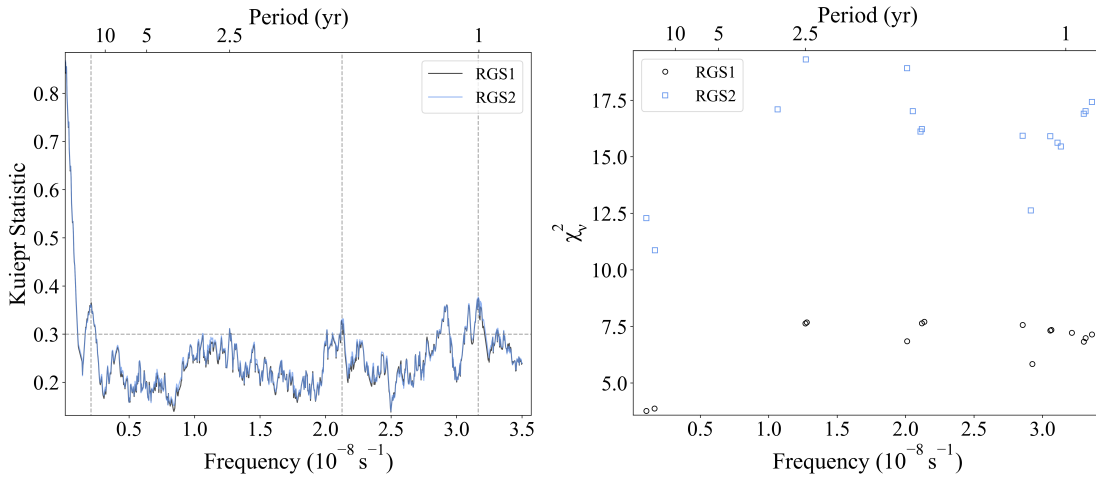


Figure 2.4: Left panel shows Kuiper statistics for RGS1 data (grey) and RGS2 data (blue), which give nearly identical results, from frequencies  $f_0 = 1.05 \times 10^{-9} \text{ s}^{-1}$  to  $3.5 \times 10^{-8} \text{ s}^{-1}$ . The horizontal dashed line indicates a Kuiper statistic of 0.3, arbitrarily determined to filter high Kuiper statistic frequency regions. Vertical dashed lines indicate three frequencies ( $0.21, 2.13, 3.17 \times 10^{-8} \text{ s}^{-1}$ ) with relatively high Kuiper statistics. No dominant period is found. Right panel shows the reduced chi-square values of RGS1 and RGS2 data fitted with sine waves, with test frequencies that have Kuiper statistic values above 0.3.

0157160901 and 0159360701; 2002 Nov 24 and 2005 Oct 15) with the highest flux and the one (ObsID 0561380101; 2009 Nov 3) with the lowest flux, the flux in the first observation (ObsID 0095810301; 2000 Jun 8), taken slightly after the cycle 1 *Chandra* observation, differs from the observation (ObsID 0810870101; 2019 Apr 14) within the cycle 19 *Chandra* observation band by only 2.6%. We will see in the following chapter that observations with high fluxes also have high emission measures and mass-loss rates, derived from a broadband emission and absorption model.

Various types of variability in  $\zeta$ Pup's X-ray spectra have been studied and periodicities reported. Berghofer et al. (1996) discovered the presence of a  $1.44 \text{ day}^{-1}$  frequency (16.7 hour period) in the *ROSAT* 0.9 – 2.0 keV data using period folding techniques. More recently,

Nazé et al. (2013) generated light curves of different time bins on the scale of kiloseconds using 18 early *XMM* exposures, revealing more significant variability towards longer timescales and a lack of short-term (< 1 day) variability. This suggested large-scale slow-moving structures superimposed on a stellar wind with highly fragmented absorbing and emitting material. No coherent, systematic periodicity was identified in these light curves (Nazé et al. 2013). After Howarth & Stevens (2014) identified a period of 1.78 days in the optical band, Nazé et al. (2018) further analyzed 26 *XMM* exposures but found no consistent correlation between the X-ray and the optical data. Phase-folding X-ray light curves from the *Chandra* cycle 19 HETGS observations, Nichols et al. (2021) identified the same 1.78 d period with 6% peak-to-valley amplitude and a phase lag of approximately 0.45 from the optical data, and marginally detected a secondary period of 5 to 6 days. Nichols et al. (2021) concluded that the 1.78 d period is most likely the rotation period of  $\zeta$ Pup, with the time lag between the X-ray and the optical data potentially due to a pair of hot spots on the star. In summary, no period of  $\zeta$ Pup has been identified on the timescale of years while long-term variability likely exists, consistent with the results in this chapter. More detailed analyses of the variability of  $\zeta$ Pup might reveal interesting features in the wind as well as connections between the stellar and wind properties.

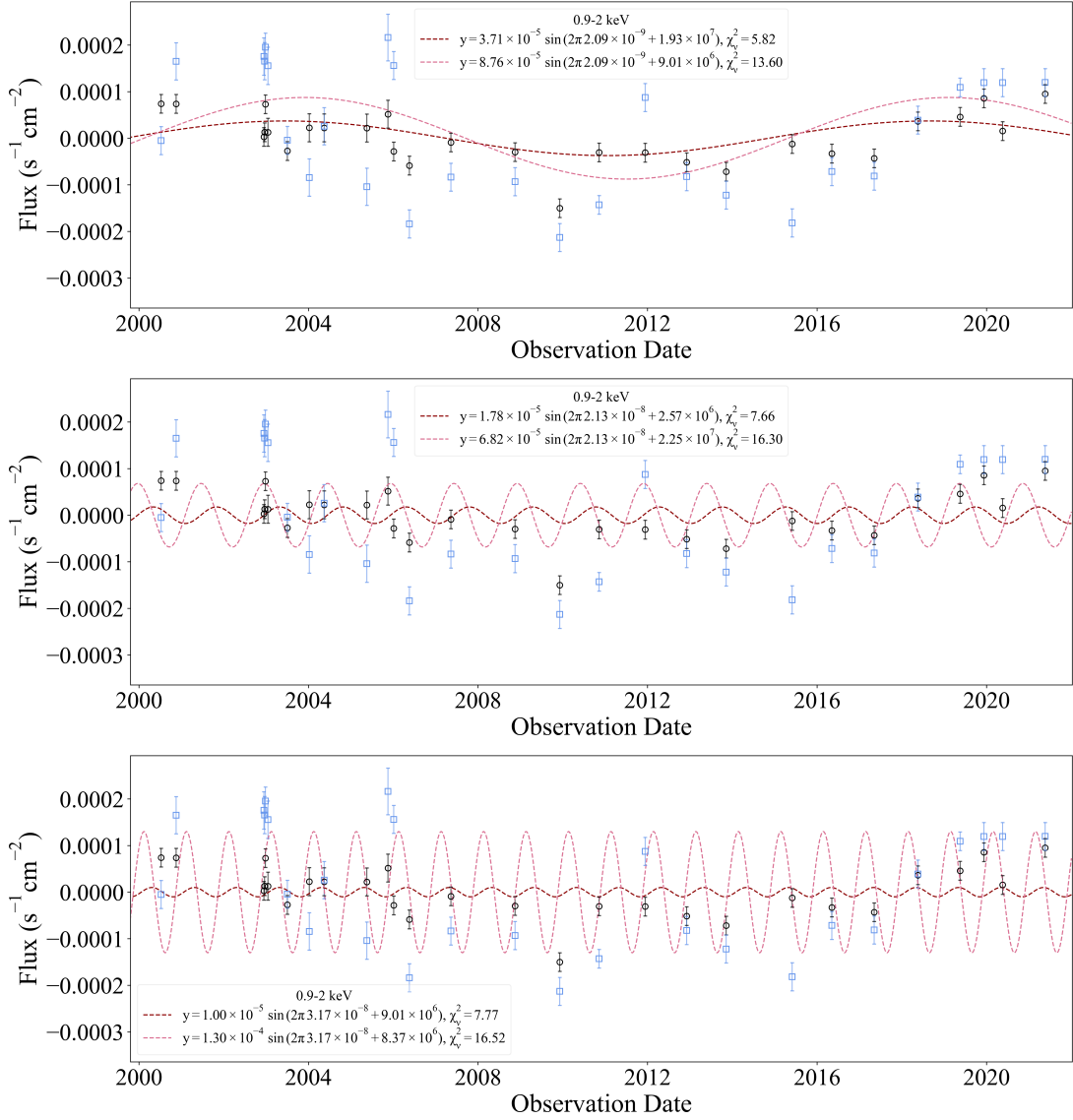


Figure 2.5: Individual sine wave fits to RGS1 and RGS2 data, with fixed frequencies at 0.21 (top panel), 2.13 (middle panel), and  $3.17 \times 10^{-8} \text{ s}^{-1}$  (bottom panel), corresponding to periods of around 15.1, 1.5, and 1.0 years. RGS1 data points are shown in black and fits are shown in pink dashed curves. RGS2 data points are shown in blue and fits are shown in red dashed curves. All fits are statistically bad, indicating low likelihood of these frequencies.

# 3

## Broadband Spectral Modeling of 20 Years of *XMM* Observations

### 3.1 INTRODUCTION

In this chapter, we derive the wind mass-loss rate of  $\zeta$ Puppis, along with the elemental abundances in its wind and the temperature distribution of its shock-heated wind plasma, from

each of the 28 *XMM-Newton* observations (see Section 2.2 for details of the data) to study the change of these physical wind properties over 20 years. Due to the systematic shifts of the wavelength scale which obscures the emission line shapes in these data (den Herder et al. 2001; Leutenegger et al. 2013), we cannot use the mass-loss rate diagnostics described in Chapter 1. However, since the mass-loss rate scales the wavelength-dependent opacity  $\kappa_\lambda$  in the expression of the characteristic wind optical depth  $\tau_*$  of each spectral line (see Figure 1.6), its value affects the differential wind absorption across the X-ray spectrum.

We use an absorption model described in Leutenegger et al. (2010) paired with a plasma emission model (Foster et al. 2012) to fit the whole spectrum, as described in Cohen et al. (2021). The fit from each observation will give us the temperature distribution of the shock-heated plasma and the elemental abundances in the wind, as well as a mass column density from the absorption model from which the mass-loss rate can be derived. We give detailed explanations of these models in Section 3.2. Section 3.3 presents the grouping and the fitting of the data. Section 3.4 presents preliminary results in correlations between the mass-loss rate, the amount of X-ray emitting plasma, and the X-ray flux. Section 3.5 discusses the preliminary results and relevant future work.

At the time of writing this thesis, I have not yet completed a full error analysis on the best-fit model parameters for each of the 28 *XMM* observations. This chapter thus present only preliminary results and discuss their possible implications.

## 3.2 THE MODELS

As discussed in Sections 0.3.2 and 0.3.3, an X-ray spectrum of  $\zeta$ Pup consists of three components: (1) line emission from collisional excitation followed by spontaneous decay, (2) con-

tinuum emission from free-free radiation and radiative recombination, and (3) absorption from photoionization in the cold, unshocked wind component.

The emission originates from the shock-heated plasma that constitutes less than 1% of the wind’s mass, and the emission power is determined by the elemental abundances and the temperature distribution of the shock-heated plasma. We use *bvapec*<sup>1</sup> (Foster et al. 2012) implemented in XSPEC (Dorman & Arnaud 2001) to model the amount of emission at each fixed temperature. The overall emission that spans a continuous range of temperatures is approximated by a sum of six *bvapec* models fixed at evenly spaced logarithmic intervals from around  $10^6$  K to  $18 \times 10^6$  K (Cohen et al. 2021). We describe the *bvapec* model, along with our choice of temperatures based on Figure 3.1, in Section 3.2.1.

As explained in Section 0.3.3, the amount of X-ray absorption locally in the wind is proportional to both the elemental abundances and the optical depth  $\tau_\lambda$  as a function of wavelength. We use *vwindtab*, a version of *windtab*<sup>2</sup> developed by Leutenegger et al. (2010), implemented in XSPEC (Dorman & Arnaud 2001) to model the wind absorption. The *vwindtab* model can be multiplied with the six *bvapec* models to reproduce the entire X-ray spectrum. The elemental abundances essential to both models are tied together and fitted simultaneously. We present a theoretical derivation of the *vwindtab* model and discuss its implementation in Section 3.2.2.

To account for absorption in the interstellar medium (ISM), we use the model *TBabs*<sup>3</sup>

<sup>1</sup>The installed XSPEC model *bvapec* is available at <https://heasarc.gsfc.nasa.gov/xanadu/xspec/manual/node136.html>. The “*b*” in *bvapec* stands for Gaussian “broadened” emission lines, and the “*v*” stands for “variable” elemental abundances.

<sup>2</sup>The custom local model *windtab* is available at <https://heasarc.gsfc.nasa.gov/xanadu/xspec/models/windprof.html>. The “*v*” in “*vwindtab*” stands for “variable” elemental abundances just like the “*v*” in “*bvapec*”.

<sup>3</sup>The installed XSPEC model *TBabs* is available at <https://heasarc.gsfc.nasa.gov/xanadu/xspec/xspec11/manual/node42.html>.

(Wilms et al. 2000), which is based on the conventional  $I = I_0 e^{-\tau}$  absorption formalism where  $I$  is the intensity of light observed,  $I_0$  is the intensity of light emitted, and  $\tau$  is the optical depth in the ISM. Suppose  $\sigma_{ISM}$  is the absorption cross section weighted by the total hydrogen number density in units of  $\text{cm}^2$ ,<sup>4</sup> and  $N_H = \int_0^\infty n_H dz$  is the column density of hydrogen atoms with units  $\text{cm}^{-2}$ , then  $\tau = \int_0^\infty \kappa \rho dz = \int_0^\infty \sigma n dz = \sigma_{ISM} N_H$  (see discussion of  $\tau$  in Section 0.3.3 and definition of  $\kappa$  in Section 0.2.1). We use  $\log N_H (\text{cm}^{-2}) = 20.00 \pm 0.05$  (corresponding to  $N_H = 1.0 \pm 0.12 \times 10^{20} \text{ cm}^{-2}$ ) for  $\zeta$ Pup, measured from the Lyman- $\alpha$  absorption assuming neutral hydrogen atoms in the ISM (Fruscione et al. 1994). The quantity  $\sigma_{ISM}$  is wavelength-dependent and is computed in Wilms et al. (2000) and stored in  $TBabs$ . The ISM absorption hardly affects the spectrum of  $\zeta$ Pup, as ignoring it increases the observed luminosity at 20 Å by 5%. We do not describe the model since the physics of the ISM is beyond the scope of this thesis.

We note that while modeling the broadband spectrum, we no longer focus on the exact shapes of the individual spectral lines. Indeed, we group the data in the observed spectra into bins each including at least 40 counts (with the aim to increase the signal-to-noise ratio per bin and de-emphasize the continuum), which obscures the line shapes. For this reason and for the sake of computational simplicity, the emission model assumes Gaussian emission lines, and the absorption model calculates the overall absorption for a given line and thus ignores the differential Doppler shift within the line.

---

<sup>4</sup>In Wilms et al. (2000),  $\sigma_{ISM}$  is defined as the absorption cross section weighted by the total hydrogen number density. So  $\sigma_{ISM}$  equals the absorption cross section of the ISM particles multiplied by the factor  $(n_{ISM}/n_H)$ , where  $n$  represents the number density in the ISM.

### 3.2.1 THE EMISSION MODEL *bvapec*

Readers may have noticed that all X-ray emission mechanisms involve the interaction of a free electron and an ion, thus modeling the emission spectrum comes down to studying the interaction rate of free electrons and ions in the wind. Since each species of ion emits at its signature wavelengths, our goal in this section is to solve for the emitted luminosity per wavelength, i.e., the power density  $\eta_\lambda$ , from a given species of ions.

Let  $n_{\text{ion}}$  and  $n_e$  be the number densities of the ion and free electrons, respectively. Then their rate of interaction per volume is  $n_e n_{\text{ion}} v \sigma$ , where  $v$  is the speed of the free election and  $\sigma$  is its interaction cross section. Technically, the free electrons do not have a single fixed velocity  $v$ , but rather demonstrate a Maxwell-Boltzmann speed distribution

$$N(v) dv = \left( \frac{m}{2\pi k T} \right)^{3/2} 4\pi v^2 e^{-mv^2/2kT} dv \quad (3.1)$$

centered at some velocity due to thermal motions. So  $v\sigma$  is essentially  $\int_0^\infty v\sigma(v) N(v) dv$ . Let  $E_\lambda$  be the photon energy emitted per wavelength for each interaction<sup>5</sup>, which for line emission peaks at different wavelengths for different ions. The intrinsic luminosity per wavelength is

$$\eta_\lambda(T) = \int_V n_e n_{\text{ion}} \int_0^\infty v\sigma(v) N(v) E_\lambda dv dV, \quad (3.2)$$

where the outer integration is over the entire volume of the wind that is shock-heated to a temperature  $T$ . For line emission, the interaction cross section  $\sigma(v)$  is zero if the relative velocity between the free electron and the ion corresponds to a kinetic energy less than the

---

<sup>5</sup>For collisional excitation followed by spontaneous de-excitation,  $E_\lambda$  has a specific value corresponding to the energy level transition. For Bremsstrahlung emission,  $E_\lambda$  is a function of the relative velocity between the interacting electron and ion, as well as the impact parameter.

ion's energy level transition.

We now aim to break equation 3.2 into two multiplicative terms: one containing thermal statistics and the physics of interaction mechanisms, and the other dependent on the wind environment. We note that the value of  $n_{\text{ion}}$  is related to the abundance of its element, as well as the temperature that controls the ionization balance in the shock-heated regions. Let  $C_H^Z = n_Z/n_H$  be the abundance of the element relative to the hydrogen abundance in the wind, and let  $C_Z^{\text{ion}}(T) = n_{\text{ion}}/n_Z$  be the ion abundance relative to its elemental abundance. Then  $n_{\text{ion}} = C_Z^{\text{ion}}(T)C_H^Z n_H$ . We define the temperature-dependent quantity, emissivity, as

$$\Lambda_\lambda(T) = C_Z^{\text{ion}}(T)C_H^Z \int_0^\infty v\sigma(v)N(v)E_\lambda \, dv, \quad (3.3)$$

with units of  $\text{ergs \AA}^{-1} \text{cm}^3 \text{s}^{-1}$ , which is the energy per wavelength times the volume that a free electron cross section can sweep through per second.

We define the emission measure at each temperature, a quantity that depends solely on the wind environment, as

$$\text{EM}(T) = \int n_e n_H \, dV, \quad (3.4)$$

with units of inverse volume. Since the free electrons mostly come from ionized hydrogen in the wind<sup>6</sup>,  $n_e \approx n_H$  which is the number density of hydrogen ions. If we assume that all ions are roughly evenly distributed throughout the wind, then the emission measure can be interpreted as a measurement of the amount of X-ray emitting plasma at a fixed temperature  $T$ . Equation 3.2 becomes

$$\eta_\lambda(T) = \text{EM}(T)\Lambda_\lambda(T). \quad (3.5)$$

---

<sup>6</sup>Almost all hydrogen atoms are ionized by the photospheric UV photons. The stellar wind is embedded in the H II region around the massive star  $\zeta$ Pup.

Since  $\Lambda_\lambda(T)/C_H^Z$  is independent of the local wind environment, it is pre-calculated from ATOMDB (the atomic database for X-ray plasma modeling) (Foster et al. 2012) and stored as a tabulation in *bvapec* to be readily applied to the wind of any star. In Figure 3.1 taken from Cohen et al. (2021), we show the quantity

$$\int_0^\infty \Lambda_\lambda(T) d\lambda \quad (3.6)$$

for emission lines observed in the *Chandra* or *XMM* spectra, with  $C_H^Z$  representing the solar abundances. We further make unit conversion from energy times volume per second to photons times volume per second by  $E = hc/\lambda$ . Note that although the integration in equation 3.6 is from zero to infinity,  $\Lambda_\lambda$  is nonzero only within a short wavelength range for a given emission line.

The shock-heated plasma in the wind of  $\zeta$  Pup should demonstrate a continuous temperature distribution (i.e., a continuous emission measure with respect to  $T$ ) which is difficult to model given limited observational data. Figure 3.1 designates a sample of discrete temperatures to approximate the continuous temperature distribution: we pick six temperatures ( $kT = 0.110, 0.187, 0.318, 0.540, 0.919, 1.56$  keV corresponding to  $T = 10^6$  K to  $18 \times 10^6$  K) at evenly spaced (0.23 dex) logarithmic intervals, indicated by the vertical dashed lines, that intersect almost all peaks of the emissivity curves. We then apply six isothermal *bvapec* models at these fixed temperatures and fit for their individual emission measure to model the emission portion of the spectrum. This six-temperature modeling of emission is both a good approximation for the continuum temperature distribution, and also more flexible than any presumed functional form, for example a power-law, of emission measure with respect to temperature.

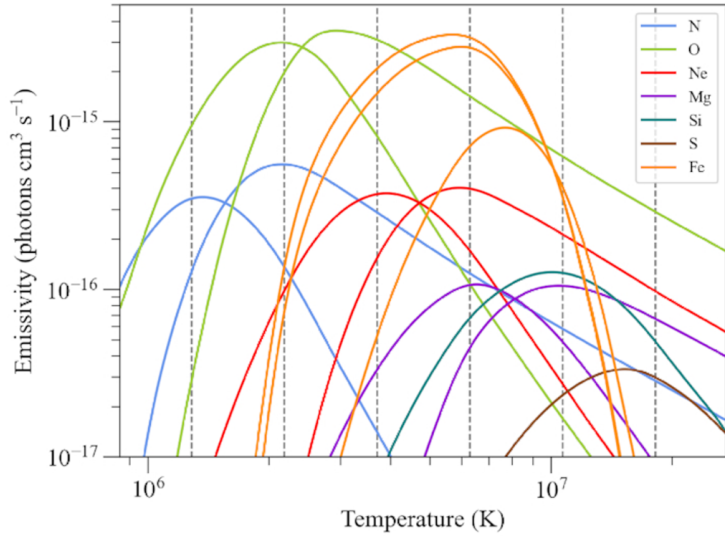


Figure 3.1: Quantity in equation 3.6 as a function of temperature of multiple ions calculated from ATOMDB. The curves can be interpreted as emissivities scaled by elemental and ion abundances, where the elemental abundances are assumed to be solar. Only line emission is taken into account. The vertical dashed lines intersecting almost all peaks of the emissivity curves represent the six temperatures we chose to approximate the shock-heated plasma.(Cohen et al. 2021, Figure 3)

We now give a brief summary of the parameters in *bvapec*. Each *bvapec* model is based on a fixed temperature, and has parameters of elemental abundances  $C_H^Z$  for He, C, N, O, Ne, Mg, Al, Si, S, Ar, Ca, Fe, and Ni. Additionally, it has a redshift parameter  $z$  that corrects proper distance to luminosity distance<sup>7</sup>, and a line width parameter  $\sigma$  that characterizes the Gaussian emission line width due to velocity broadening<sup>8, 9</sup>. Finally, the observed emission

<sup>7</sup>For a distant light source at redshift  $z$ , the actual distance that light travels  $d_L$  (the luminosity distance) and the current physical separation between the Earth and the light source  $d$  (the current proper distance) satisfies  $d_L = d(1+z)$ , assuming the universe is geometrically flat. For stars within our own Galaxy like ζ Pup,  $z = 0$ .

<sup>8</sup>When modeling the broadband emission, we make the approximation that the emission lines are Gaussian instead of asymmetric as indicated by the line profile model in Chapter 1. If the characteristic wind optical depth  $\tau_*$  is modest, the line profile is well approximated by a blueshifted, Gaussian broadened profile.

<sup>9</sup>The  $\sigma$  parameter accounts for the velocity broadening, and the  $z$  parameter effectively takes the blueshift into account, despite its formal definition as the cosmological redshift.

measure (emission measure corrected by the luminosity distance based on the inverse square law) is represented by the parameter “norm”, mathematically expressed as

$$\text{norm} = \frac{10^{-14}}{4\pi d^2(1+z)^2} \int n_e n_H dV = \frac{10^{-14}}{4\pi d^2(1+z)^2} \text{EM}(T), \quad (3.7)$$

where  $d$  is the physical separation between the Earth and the star.

### 3.2.2 THE ABSORPTION MODEL *vwindtab*

We aim to derive a unitless transmission factor  $T(\lambda)$  at each wavelength, whose value is between zero and one, to be multiplied by the intrinsic X-ray emission  $\eta_\lambda$  to reproduce the entire observed spectrum. Transmission  $T$  is defined simply as the fraction of emitted light that is transmitted to the observer, while  $1 - T$  is the fraction absorbed. The derivation presented below is outlined in [Leutenegger et al. \(2010\)](#).

We first remind the reader of the assumptions we make for stellar winds with X-rays generated through embedded wind shocks (EWS): the X-ray emission begins at some onset radius  $R_o \approx 1.5R_*$ , and the X-ray emitting plasma is distributed throughout the wind beyond  $R_o$ , demonstrating proportionality to  $\rho(r)^2$  with spherical symmetry. From equation 1.2, the observed X-ray luminosity at a given wavelength satisfies

$$L_\lambda \propto \int_0^{2\pi} \int_{R_*}^{\infty} \rho(r)^2 e^{-\tau(r,\theta)} r^2 \sin \theta dr d\theta, \quad (3.8)$$

where  $(r, \phi, \theta)$  represents the spherical polar coordinates centered on the star,  $\rho(r)$  is the local wind mass density, and  $\tau(r, \theta)$  is the wind optical depth as defined in Section 1.2.2.

At each point in the wind,  $\tau(p, z)$ , where  $p \equiv r \sin \theta$  and  $z \equiv r \cos \theta$ , is given by equation

1.5. We define a scaled optical depth

$$t(p, z) \equiv \int_z^\infty \frac{dz'}{(p^2 + z'^2)(1 - R_*/\sqrt{p^2 + z'^2})^\beta} \quad (3.9)$$

so that  $\tau(p, z) = \tau_* t(p, z)$  outside the wind occultation region. Recall that  $\tau_* = \kappa_\lambda \dot{M} / 4\pi v_\infty R_*$ , and we define new constant characteristic wind mass column density  $\Sigma_* = \dot{M} / 4\pi v_\infty R_*$ , with units  $\text{g cm}^{-2}$ , so that

$$\tau_* = \frac{\kappa_\lambda \dot{M}}{4\pi v_\infty R_*} = \kappa_\lambda \Sigma_*. \quad (3.10)$$

Note that  $\Sigma_*$  is independent of wavelength. We introduce a new coordinate  $\mu \equiv \cos \theta = z/r$  that will become useful later, so that we can transform  $t(p, z)$  to  $t(r, \mu)$  by

$$p = r\sqrt{1 - \mu^2}, \quad z = r\mu. \quad (3.11)$$

Since we aim to model the broadband absorption and thus can relax on the details concerning differential Doppler shift within each emission line, we define an angle-averaged transmission  $\bar{T}(r)$  at each radius  $r$ . Note that as  $\theta$  goes from 0 to  $\pi$ ,  $\mu$  goes from 1 to  $-1$ . Thus the angle-averaged transmission is defined as

$$\bar{T}(r, \Sigma_*) \equiv \frac{\int_1^{-\mu_{\text{crit}}} e^{-\kappa_\lambda \Sigma_* t(r, \mu)} d\mu}{\int_1^{-1} d\mu} = \frac{1}{2} \int_{-\mu_{\text{crit}}}^1 e^{-\kappa_\lambda \Sigma_* t(r, \mu)} d\mu, \quad (3.12)$$

where  $\mu_{\text{crit}}$  is a positive value that represents the wind occultation boundary,

$$\mu_{\text{crit}} \equiv \sqrt{1 - \frac{R_*^2}{r^2}}. \quad (3.13)$$

The net transmission  $T(\tau_*)$  then becomes the transmitted flux divided by the emitted flux integrated over the whole volume,

$$T(\Sigma_*) = \frac{\int_{R_o}^{\infty} \rho(r)^2 \bar{T}(r, \Sigma_*) r^2 dr}{\int_{R_o}^{\infty} \rho(r)^2 r^2 dr}. \quad (3.14)$$

Note that the bound of the radial integration goes from the onset radius  $R_o$ , rather than the stellar radius, to infinity. In *windtabs* or its variation *vwindtab*,  $R_o$  is not a free parameter and is set to  $1.5 R_*$  based on the results from hydrodynamical simulations (see Section 0.3.1). If we use the inverse radius coordinate  $u \equiv R_*/r$  to speed up numerical integration, and substitute in the mass continuity equation  $\rho(r) \propto v(r)^{-1} r^{-2}$  as well as the  $\beta$ -velocity  $v(u) \propto (1 - u)^\beta$ , equation 3.14 becomes

$$T(\Sigma_*) = \frac{\int_0^{u_o} (1 - u)^{-2\beta} \bar{T}(u, \Sigma_*) du}{\int_0^{u_o} (1 - u)^{-2\beta} du}. \quad (3.15)$$

Equation 3.15 is our final expression for transmission. In summary, when calculating  $T(\Sigma_*)$  numerically, we first integrate equation 3.12 to get the angle-averaged transmission at each radius  $r$  based on a pre-calculated  $\kappa_\lambda$  tabulation, then perform the radial integration in equation 3.15 to get the net transmission as a function of wavelength, where the wavelength dependence comes from the opacity  $\kappa_\lambda$ .

The transmission is calculated based on the assumption that the shock-heated emitting gas is embedded within the absorbing, cool bulk of the wind. As stated in [Leutenegger et al. \(2010\)](#), this treatment of absorption is more realistic than the previously developed slab model, where the absorbing medium is assumed to be in between a single X-ray emitting source and the observer, and the absorption follows the  $e^{-\tau}$  formalism. And it is more

exact than the exospheric model (Owocki & Cohen 1999), where  $T = 0$  below some radius of optical depth unity, and  $T = 1$  above it. Figure 3.2, taken from Leutenegger et al. (2010), compares the three absorption models at different  $\tau_* = \kappa_\lambda \Sigma_*$  values. We observe that the transmission from equation 3.15, or the *windtabs* model, decreases less rapidly than that from the slab model ( $e^{-\tau}$ ) and is nonzero at large  $\tau_*$  because of the extended distribution of the X-ray emitting plasma.

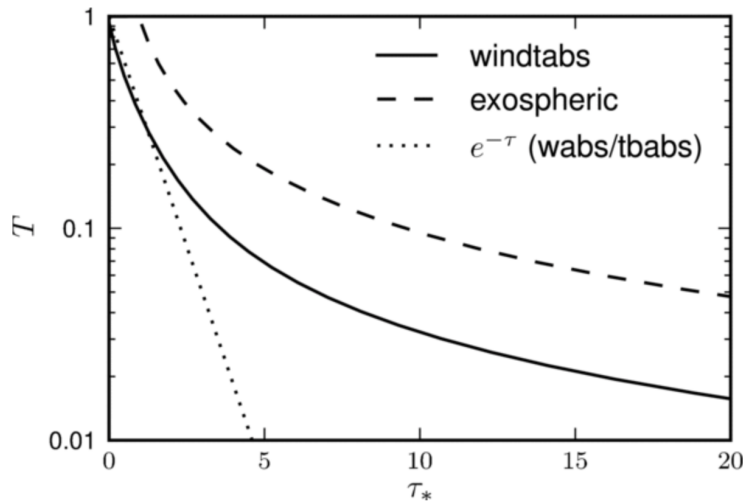


Figure 3.2: Transmission curves derived from the *windtabs* model according to equation 3.15 (black solid line), the exospheric model (dashed line), and the slab model (dotted line). Values of  $\beta = 1$  and  $R_o = 1.5R_*$  are adopted (Leutenegger et al. 2010, Figure 5).

The difference between *vwindtab* and *windtabs* lies in the opacity  $\kappa_\lambda$ . Since a perturbed ionization balance affects only the edges of the opacity curve (see Figure 2) by a slight amount,  $\kappa_\lambda$  is always calculated with a presumed, fixed ionization balance for O stars. Therefore,  $\kappa_\lambda$  is purely determined by elemental abundances. The *windtabs* model assumes solar elemental abundances, and *vwindtab* allows user-defined abundances for He, C, N, O, Ne, Mg, Al, Si, S, Ar, Ca, Fe, and Ni (exactly those that are free to vary in the *bvapec* model). Among these

elements, C, N, and O are known to be non-solar (Martins et al. 2015) and the observed Ne emission lines are weaker than expected in  $\zeta$ Pup’s spectra. So when we model the broadband spectrum, the elemental abundances of C, N, O, and Ne from *vwindtab* and *bvapec* are tied together and fitted simultaneously, while the other abundances are frozen at solar values.

A new feature added to *vwindtab* specific to this project is the consideration of fully ionized helium atoms ( $\text{He}^{++}$ ) recombining into He II atoms ( $\text{He}^+$ ) beyond around  $5 R_*$ . The helium atoms are fully ionized by photospheric UV radiation, and are known to recombine in the outer stellar wind regions in sufficiently dense and cool winds (Puls et al. 2006). The photoionization threshold for He II is at 228 Å in the UV band. But the high abundance of helium atoms renders a strong peak in the opacity curve with a  $\kappa_\lambda \propto \lambda^3$  fall-off shortward of 228 Å that extends into the soft X-ray band (see Section 0.3.3 for discussions about photoionization absorption mechanism and the behavior of  $\kappa_\lambda$ ). As the *XMM* spectra extend out to above 35 Å, the absorption effect due to He II ions is no longer negligible. In Figure 3.3, we compare the two  $\kappa_\lambda$  curves, based on the solar abundances and the best-fit elemental abundances for  $\zeta$ Pup (with enhanced nitrogen and depleted carbon and oxygen) respectively, with and without an additive He II opacity function. We observe a significant increase in  $\kappa_\lambda$  at wavelengths longer than around 15 Å for both the solar and the best-fit abundances. We also note that the depletion of oxygen and the enhancement of nitrogen in the best-fit  $\kappa_\lambda$  curves have large impacts on photoionization edges of oxygen and nitrogen, at around 20 Å and 25 Å, respectively.

When taking He II photoionization into account in *vwindtab*, we use the  $\kappa_\lambda$  tabulation without He II absorption for  $\bar{T}(r, \Sigma_*)$  at  $r < 5 R_*$  (see equation 3.12), and with He II absorption added for  $\bar{T}(r, \Sigma_*)$  at  $r \geq 5 R_*$ . That is, the adopted  $\kappa_\lambda$  is adjusted from the solid

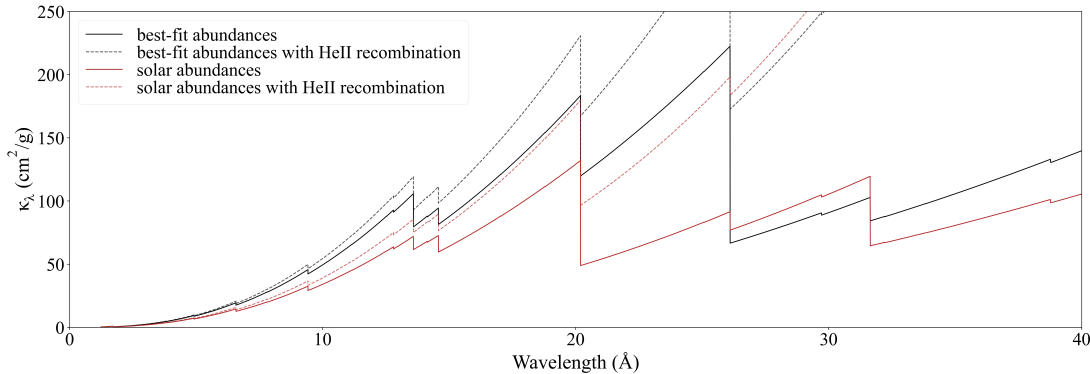


Figure 3.3: The opacity  $\kappa_\lambda$  with He II photoionization taken into account, assuming  $\zeta$ Pup's best-fit elemental abundances with enhanced nitrogen and depleted carbon and oxygen (in dashed black line), and solar abundances (in dashed red line). The solid lines show the corresponding  $\kappa_\lambda$  without He II photoionization, and are identical to the lines shown in Figure 2.

curve in Figure 3.3 to its corresponding dashed curve at  $5 R_*$  with a third order Butterworth filter, as we perform the radial integration in the numerator of equation 3.15.

### 3.3 GROUPING AND FITTING THE DATA

Observations and data from the *XMM-Newton Observatory* are described in Section 2.2. To recapitulate, *XMM* carried out 28 observations listed in Table 2.1, each with an RGS1 and an RGS2 spectra. The discussed systematic shifts on the wavelength scale that obscures the emission line shapes hardly affect the broadband fitting of the spectra. To effectively smooth the continuum and increase the spectral signal-to-noise ratio, we adaptively group the RGS1 and RGS2 spectra individually using GRPPHA<sup>10</sup>, requiring at least 40 counts in each bin. We then group together the forbidden and intercombination lines of each helium-like complex

<sup>10</sup>GRPPHA is a task within the HEASARC, available at <https://heasarc.gsfc.nasa.gov/lheasoft/ftools/heasarc.html>.

by changing the grouping flags in the PHA files. This is because the *bvape*c model computes the combined flux of the forbidden and intercombination lines correctly, but not their line flux ratio<sup>11</sup> (Cohen et al. 2021). Figure 3.4 shows the RGS1 and RGS2 spectra of the first *XMM* observation (ObsID 0095810301) as an example.

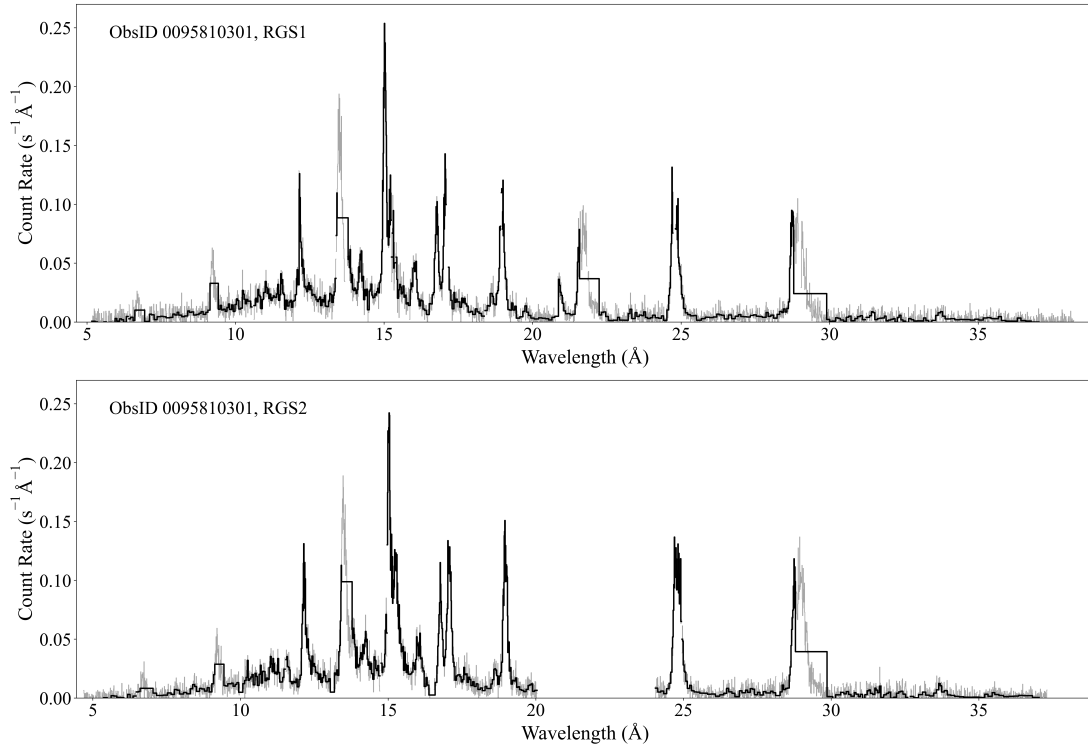


Figure 3.4: The grouped RGS1 (top panel) and RGS2 (bottom panel) spectra of the first *XMM* observation (ObsID 0095810301). The effect of groupings can be observed by comparing the ungrouped spectra (light grey) with the grouped spectra (black). The gap in the RGS2 spectrum is due to degradation in the CCD assembly (see Section 2.3).

<sup>11</sup> Helium-like complex refers to the closely spaced but observationally distinguishable line triplets - the resonance, intercombination, and forbidden lines - from any helium-like ions. Bound electrons from the ground level are collisionally excited to the  $n = 2$  levels  $^1P_1$  (resonance),  $^3P_{0,1,2}$  (intercombination), or  $^3S_1$  (forbidden). Electrons from the metastable  $^3S_1$  level can further be excited to the  $^3P_{0,1,2}$  levels through UV photoexcitation. Thus examining the flux ratio between the intercombination and forbidden emission lines indicates the distance of the X-ray emitting plasma from the star. Details are discussed in Porquet et al. (2010).

We fit the 5 Å – 37 Å RGS1 and RGS2 spectra from each observation simultaneously with the emission model *bvapec* combined with the multiplicative wind absorption model *vwindtab* and a fixed ISM absorption model *TBabs*. The *vwindtab* model assumes an X-ray onset radius  $R_o = 1.5 R_*$  and a wind acceleration parameter  $\beta = 1$ . Because of the weak Ne emission lines, and because  $\zeta$  Pup is known to demonstrate super-solar N abundance and sub-solar O abundance in UV spectroscopy (Martins et al. 2015), and its wind is chemically enriched by materials from the stellar core undergoing CNO nucleosynthesis (Kahn et al. 2001), we allow the abundances of C, N, O, and Ne to be free parameters fitted jointly through *bvapec* and *vwindtab*. The other elemental abundances are fixed at solar values.

We summarize the free parameters: C, N, O, and Ne abundances; norm (equation 3.7) for each of the six chosen temperatures in *bvapec*; redshift  $z$  and emission line width  $\sigma$  in *bvapec*; and  $\Sigma_*$  in *vwindtab*. We note that the values of  $\sigma$  and  $z$  are trivial since both are affected by wavelength calibration errors and the asymmetric emission line shapes, and the cosmological redshift of  $\zeta$  Pup is effectively zero. The parameter  $\Sigma_*$ , however, should be carefully analyzed as it indicates  $\zeta$  Pup’s mass-loss rate through equation 3.10.

The best-fit parameter values are found by minimizing the Churazov-weighted  $\chi^2$  (Churazov et al. 1996)<sup>12</sup>. We do not achieve formally good statistical fits (reduced  $\chi^2$  values are around 2 to 3 for all observations) mainly due to errors in the atomic models as well as the Gaussian approximation of the line profiles (Cohen et al. 2021).

---

<sup>12</sup>The Churazov weighting assigns weight to a given bin based on its counts in a smoothed spectrum. In this case, the smoothing of the spectrum is performed through adaptive grouping. We use the Churazov weighting since it takes into account not only the counts in the given bin, but also those in the surrounding bins, in alignment with the spreading of the photon-energy-to-channel mapping. The implementation of the Churazov weighting is described at <https://heasarc.gsfc.nasa.gov/xanadu/xspec/manual/nodel19.html>.

### 3.4 RESULTS

We show in Figure 3.5 the RGS1 spectral fits for observations with the highest total flux (ObsID 0561380101), with the lowest total flux (ObsID 0810870201), closest to the *Chandra* cycle 1 observation (ObsID 0095810301), within the *Chandra* cycle 19 observation period (ObsID 0810870101), with the highest best-fit  $\Sigma_*$  (ObsID 0157161101), and with the lowest best-fit  $\Sigma_*$  (ObsID 0159360701). The best-fit parameters and the fit statistics are listed in Table 3.1.

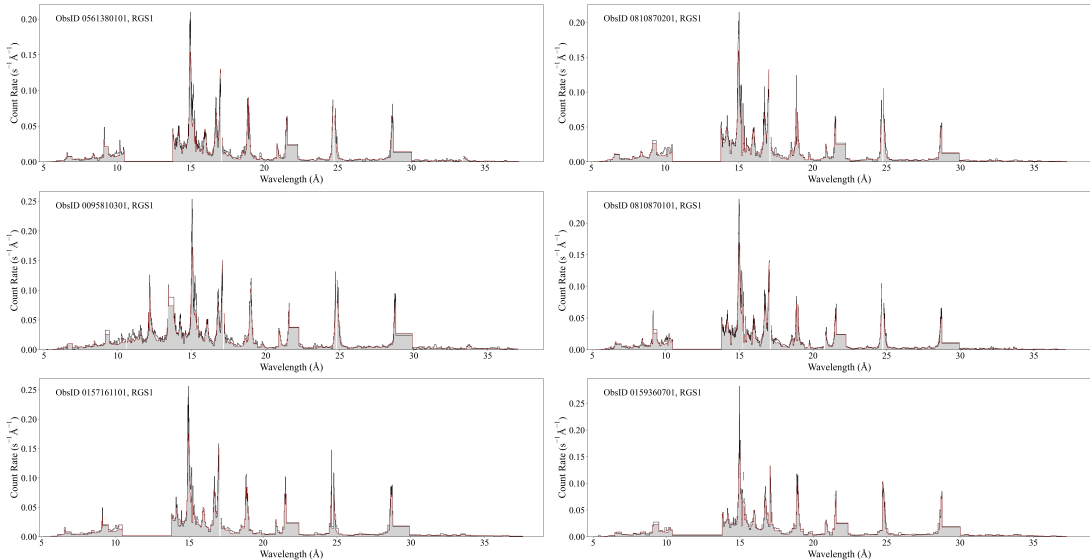


Figure 3.5: Broadband spectral modeling of *XMM* RGS1 spectra with ObsID 0561380101 (top left), 0810870201 (top right), 0095810301 (middle left), 0810870101 (middle right), 0157161101 (bottom left), 0159360701 (bottom right). Black curves show the data, and red curves enhanced by grey shadings show the models.

Table 3.1: Broadband best-fit model parameters

ObsID	$\Sigma_*$	$\dot{M}$	C	N	O	Ne	norm <sub>1</sub>	norm <sub>2</sub>	norm <sub>3</sub>	norm <sub>4</sub>	norm <sub>5</sub>	redshift	line width	$\chi^2$	$N_{\text{data}}$
0095810301	5.31	3.13	0.28	10.12	0.74	2.27	851	466	521	154	89	4.47	899	2511	1062
0095810401	4.49	2.65	0.42	11.98	0.84	2.46	628	335	507	154	69	-19.5	853	1788	693
0157160401	4.28	2.52	0.39	10.83	0.82	2.13	614	340	487	110	77	-28.7	877	1918	698
0157160501	4.78	2.82	0.42	12.35	0.86	2.30	634	409	503	200	66	-29.5	908	1734	706
0157160901	4.54	2.68	0.36	11.76	0.86	2.47	614	381	485	182	63	-33.3	872	2264	759
0157161101	5.73	3.38	0.37	9.73	0.69	2.15	956	538	544	171	92	-34.8	895	1331	505
0159360101	5.17	3.05	0.33	9.67	0.70	2.07	858	536	478	168	67	-2.35	892	2647	1061
0163360201	4.62	2.72	0.38	10.33	0.80	2.04	677	429	438	120	79	-36.5	881	1577	562
0159360301	5.33	3.14	0.28	9.92	0.68	2.32	894	600	461	184	62	-14.0	902	1011	510
0159360501	5.16	3.04	0.30	10.00	0.75	2.21	838	429	449	131	93	-17.8	863	1342	587
0159360701	3.93	2.32	0.40	11.13	0.80	1.73	572	322	438	110	71	-20.4	952	1191	475
0159360901	4.62	2.72	0.30	10.62	0.79	2.11	661	382	487	126	78	-34.7	885	2279	809
0159361101	4.96	2.92	0.35	10.65	0.77	2.22	716	469	430	162	57	-14.7	860	1633	672
0414400101	5.30	3.12	0.35	10.47	0.77	2.14	776	463	494	164	78	-18.1	870	2328	916
0159361301	4.66	2.75	0.31	10.51	0.79	2.19	615	359	453	155	58	-17.9	847	2395	908
0561380101	4.33	2.55	0.40	10.89	0.80	2.48	572	316	374	142	49	-26.8	864	2407	899
0561380201	4.88	2.88	0.36	10.98	0.75	2.16	657	441	425	159	71	-14.1	873	2902	1058
0561380301	4.24	2.50	0.38	11.60	0.84	2.41	521	354	402	174	57	-27.4	861	2684	941
0561380501	4.50	2.65	0.32	11.99	0.86	2.36	482	349	407	154	71	-28.5	884	2349	833
0561380601	4.79	2.82	0.32	10.17	0.70	2.25	606	444	383	146	70	-16.4	899	2486	914
0561380701	5.14	3.03	0.39	10.41	0.78	2.17	708	417	466	166	66	-15.4	915	1946	788
0561380901	4.46	2.63	0.31	10.97	0.82	2.35	517	343	402	149	65	-20.9	902	2618	913
0561381001	4.38	2.58	0.39	11.45	0.89	2.45	477	329	378	176	62	-18.4	878	2103	827
0561381101	5.37	3.17	0.33	10.23	0.72	2.26	676	522	462	176	95	-23.3	958	2348	888
0810870101	5.15	3.04	0.31	10.37	0.71	2.25	596	514	449	199	78	-23.1	913	2933	1150
0810870201	5.50	3.24	0.34	10.93	0.75	2.17	619	568	458	219	98	-20.5	919	1560	666
0810871301	5.58	3.29	0.32	10.45	0.70	2.35	686	601	468	219	85	-24.7	914	2308	916
0810871401	5.69	3.35	0.29	9.87	0.69	2.23	757	608	441	205	105	-22.3	955	2361	906

The wind mass column density  $\Sigma_*$  is in  $10^{-2} \text{ g cm}^{-2}$ , and the mass loss rate is in  $10^{-6} \text{ M}_\odot \text{ yr}^{-1}$ , calculated from  $\Sigma_* = \dot{M}/4\pi v_\infty R_*$  where  $v_\infty = 2250 \text{ km s}^{-1}$  is the wind terminal velocity and  $R_* = 18.9 R_\odot$  is the stellar radius (for consistency with the analysis in Chapter 1). The elemental abundances are relative to solar (Asplund et al. 2009), which are essentially  $C_H^Z/(C_H^Z)_{\text{solar}}$ . The norms at  $kT = 0.110, 0.187, 0.318, 0.540, 0.919 \text{ keV}$  have units of  $10^{-10} \text{ cm}^{-3}/4\pi d^2(1+z)^2$ , where  $d = 332 \text{ pc} = 1.02 \times 10^{21} \text{ cm}$  is the distance of  $\zeta \text{ Pup}$ . The norms can be converted to the physical quantity emission measure (EM) through equation 3.7. The unitless redshift  $z$  is in factors of  $10^{-4}$ . We find  $\text{norm}_6$  at  $kT = 1.56 \text{ keV}$  to be consistently zero for all observations. The Gaussian line width of emission lines are in  $\text{km s}^{-1}$ . We also list the number of fitted bins in each observation as well as the fit statistics  $\chi^2$  in the last two columns.

### 3.4.1 THE DIFFERENTIAL EMISSION MEASURE AND ELEMENTAL ABUNDANCES

We find a consistent behavior of the temperature distribution over the 28 observations. Figure 3.6 shows emission measure as a function of plasma temperature, with the first two emission measures averaged due to a known degeneracy between the two low-temperature components Cohen et al. (2021), and the emission measure at the highest temperature found to be consistently zero. The emission measure, or the volume of the X-ray emitting plasma, concentrates in between one and five million Kelvin, and decreases quite drastically at higher temperatures. In particular, the first two low-temperature wind plasma (at  $kT = 0.110$  and  $0.187$  keV) contribute around 62% of the total emission measure, and the first three (with  $kT = 0.318$  keV) contribute around 87% of the total emission measure.

The elemental abundances in the wind are reassuringly consistent over the 28 observations. The mean abundances relative to solar, weighted by each observation's exposure time, are 0.34, 10.71, 0.77, and 2.25 for C, N, O, and Ne, respectively. The C, N, and O abundances are less extreme than the values reported in Martins et al. (2015), which are 0.015, 18.64, and 0.28, respectively<sup>13</sup>. Since we do not expect the abundances to change over the timescale of 20 years, the next step of this project is to freeze the abundances to their weighted means and fit for the temperature distribution and the mass-loss rate for each observation, so that we can perform error analysis with more constraint.

---

<sup>13</sup>The values in Table 1 of Martins et al. (2015) are absolute abundances  $C_H^Z$ . We divide them by the solar abundances  $(C_H^Z)_{\text{solar}}$  in Table 1 of Asplund et al. (2009) to compare with our derived values in Table 3.1.

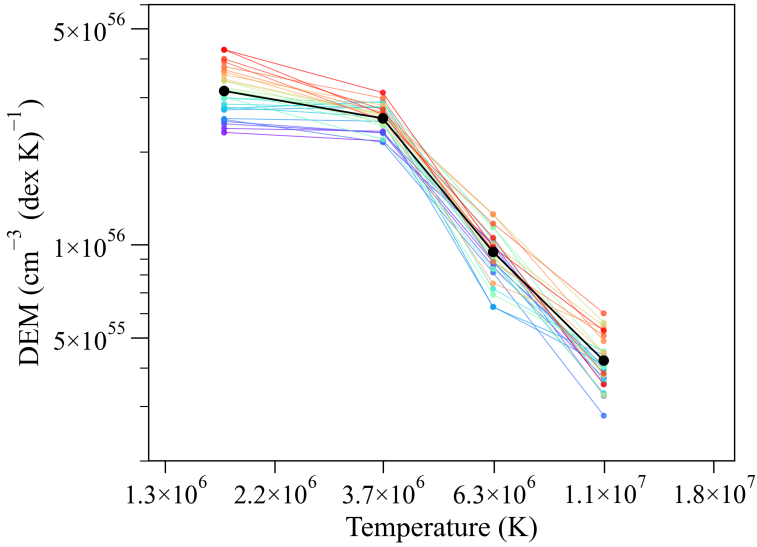


Figure 3.6: Emission measure as a function of plasma temperature for the 28 observations (each in a different color) and their mean weighted by the observations' exposure times (in black). The emission measures at the two low-temperature components have been averaged together due to degeneracy between the two temperature components, and those at the highest temperature component are omitted since they are found to be consistently zero. The temperatures are evenly spaced at 0.23 dex logarithmic intervals ( $\Delta \log T = 0.23$ ), and the differential emission measures have units of per dex K.

#### 3.4.2 TIME VARIABILITY ON MASS-LOSS RATE AND RELATED CORRELATIONS

We plot the mass-loss rate and the total emission measure against observation times in Figure 3.7 (see Figure 2.3 for a similar plot for the total flux). We see similar time variability in both quantities, as expected due to their correlation which we show in the next paragraph. The mass-loss rate in the first observation (ObsID 0095810301; 2000 Jun 8) slightly after the cycle 1 *Chandra* observation is nearly identical to that in the observation (ObsID 0810870101; 2019 Apr 14) within the cycle 19 *Chandra* observation band. However, a maximum (peak-to-peak) amount of 37% mass-loss rate variation exists between observations 0157161101

(2002 Dec 15) and 0159360701 (2005 Oct 15), and the mass-loss rate seems to be able to change drastically within months. The standard deviation of the mass-loss rate is around 10% of the mean at  $2.89 \times 10^{-6} M_{\odot} \text{ yr}^{-1}$ . A maximum (peak-to-peak) amount of 47% total emission measure variation exists between observations 0157161101 (2002 Dec 15) and 0561381001 (2017 Apr 4). The standard deviation of the total emission measure is around 13% of the mean at  $2.35 \times 10^{56} \text{ cm}^{-3}$ . Neither the total emission measure nor the mass-loss rate show an overall increasing or decreasing long-term trend.

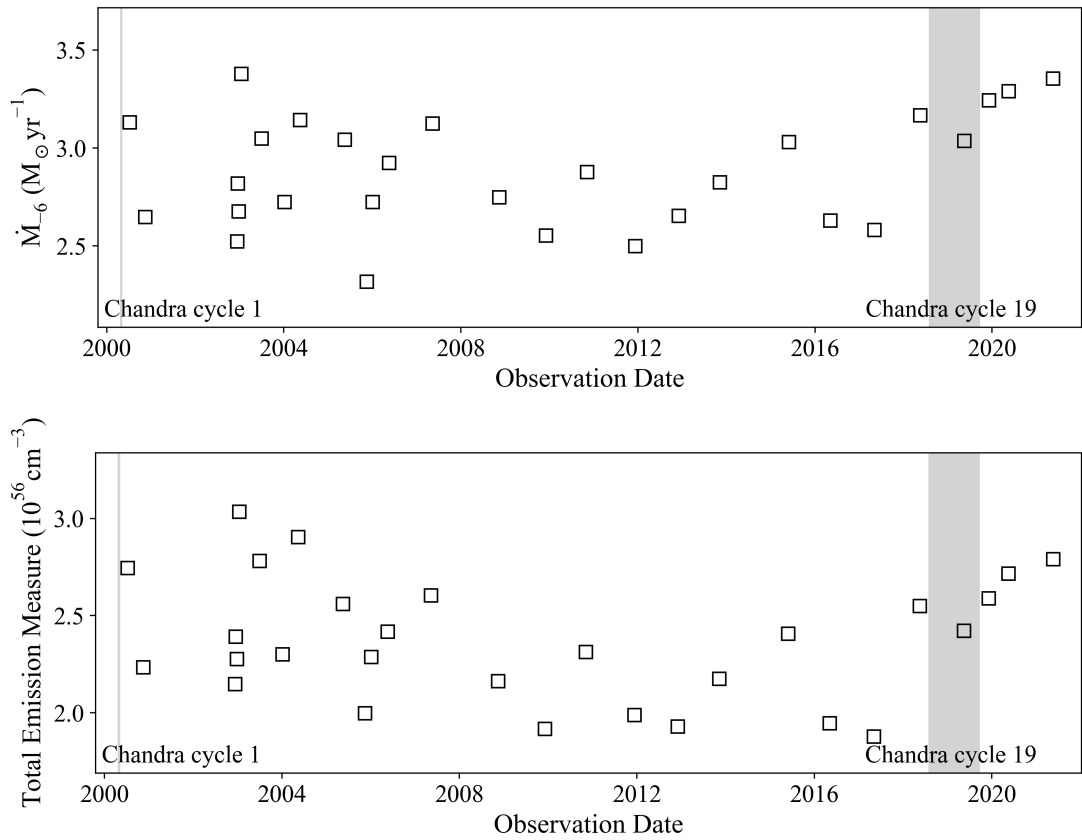


Figure 3.7: Time variability of mass-loss rate (top panel) and total emission measure (bottom panel). Each data point represent an *XMM* observation. Grey bands indicate the periods when the *Chandra* cycle 1 and cycle 19 data were taken.

We show the correlations between the mass-loss rate, the total emission measure, and the total flux over the Berghöfer energy band (as calculated in Chapter 2) in Figure 3.8. We observe a strong correlation ( $r = 0.90$ ) between the mass-loss rate and the total emission measure, which could be partially explained by the parameter degeneracy between  $\Sigma_*$  and norms (equation 3.7) when modeling the spectra: a high total norm implies strong emission mostly in the low-temperature plasma that contribute to long-wavelength emission, which can be counteracted by large wind absorption. We show in Figure 3.9 the emission due to each isothermal wind component, as modeled in *bvapec*. Flux and mass-loss rate show no correlation ( $r = 0.13$ ), and flux and total emission measure have a moderate correlation ( $r = 0.32$ ).

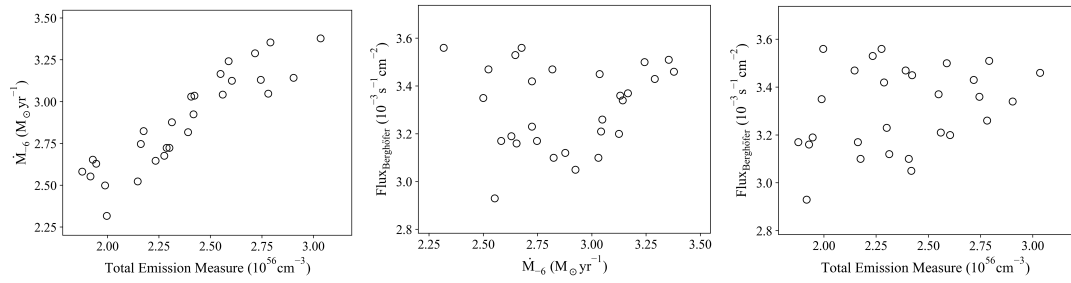


Figure 3.8: The correlations between the mass-loss rate and the total emission measure (left panel), the mass-loss rate and the total flux (middle panel), and the total flux and the total emission measure (right panel). The Pearson correlation coefficients from left to right are 0.90, 0.13, and 0.32, respectively.

### 3.5 DISCUSSION AND CONCLUSIONS

We acquire reasonable, but not formally good, fit statistics in all observations. The overall spectrum shape and most of the line strengths are successfully modeled. The measured Mg xi helium-like complex at 9.169 Å are above the model in some observations and are well-produced in others. Other poorly-modeled lines are discussed in Cohen et al. (2021): Fe xvii

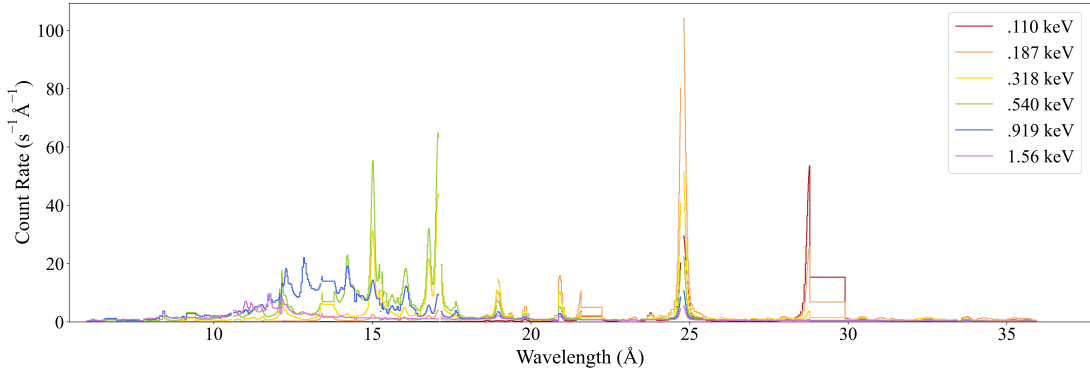


Figure 3.9: Pseudo-spectrum produced from isothermal *bvapc* models at the six chosen temperatures, assuming solar elemental abundances, norms of unity, and no wind absorption. We note that emission at long wavelengths comes from relatively low-temperature plasma.

lines are known to have disagreements in their predicted and observed resonance line cross sections and are thus not well-modeled in the spectra (Brown et al. 2006); dielectronic satellite lines<sup>14</sup> from Fe XVI (mostly between 15.01 and 15.26 Å) are not incorporated into *apec* but are known to exist in plasma at several million Kelvin (Beiersdorfer et al. 2018). Nevertheless, performing the same analysis on the spectra but eliminating data from 16.5 to 17.5 Å (where several iron lines are) results in no statistically significant difference in fits and DEM shapes. The assumption that all emission lines are Gaussian rather than asymmetric is also a source of systematic error. The addition of He II opacity above  $5 R_*$  has a noticeable impact on the modeling of the long-wavelength spectra and significantly improves the fit statistics.

We find rather consistent C, N, O, and Ne abundances over the 28 *XMM* observations. The overall metallicity for  $\zeta$ Pup is  $C_H^C + C_H^N + C_H^O + C_H^{Ne} = n_{C+N+O+Ne}/n_H = 13.8 \times 10^{-4}$ , which is 52% above its corresponding solar value,  $9.1 \times 10^{-4}$  (Asplund et al. 2009). However,

---

<sup>14</sup>As a free electron recombines with an ion to an excited state, it may excite a bound electron and the excited ion may de-excite. This creates a dielectronic satellite photon at a wavelength slightly longer than the corresponding energy level transition due to the recombined, excited electron.

this result is only tentative and the confidence intervals of the metallicities, dominated by errors in the *apec* model, might overlap.

We find consistent temperature distribution over the 28 *XMM* observations. The differential emission measure, which is shown in Figure 3.6, is consistent both in shape and in its total value with those found from the *Chandra* cycle 1 and cycle 19 observations (see left panel of Figure 3.10, from G. Rak’s 2022 KNAC symposium poster<sup>15</sup> and D. H. Cohen’s talk at the 19th HEAD meeting of the AAS in Pittsburgh<sup>16</sup>). Furthermore, the overall shape is similar to those observed in other massive stars, such as  $\varepsilon$  Ori,  $\zeta$  Ori, and  $\xi$  Per (see right panel of Figure 3.10, from Cohen et al. (2021)), which imply universal line-deshadowing instability (LDI) and shock strength distribution in radiation-driven winds.

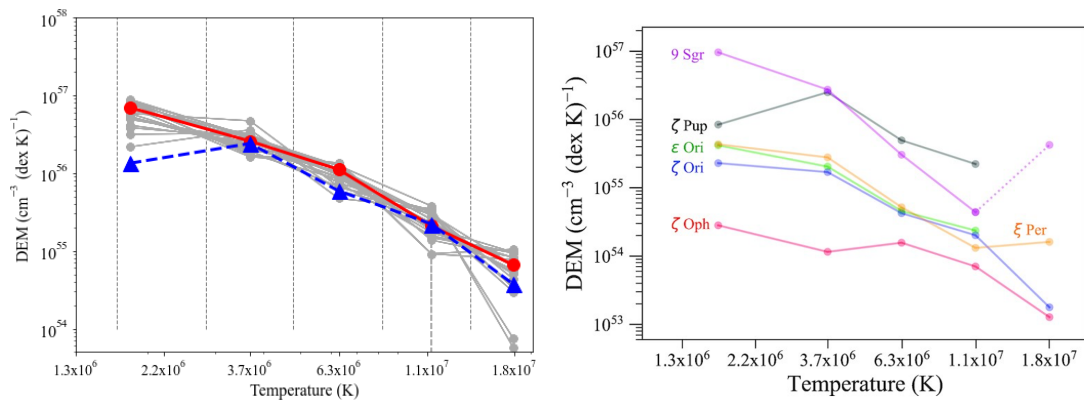


Figure 3.10: Differential emission measures (DEM) from the *Chandra* cycle 1 (blue) and cycle 19 (red) observations on  $\zeta$  Pup (left panel, from G. Rak’s 2022 KNAC symposium poster), and from *Chandra* observations on a set of O and early B stars (right panel, from Cohen et al. (2021, Figure 4)).

<sup>15</sup>G. Rak’s 2022 KNAC symposium poster and poster abstract is available at <https://sites.google.com/haverford.edu/knac2021/posters?authuser=0>.

<sup>16</sup>D. H. Cohen’s talk at the 19th HEAD meeting of the AAS in Pittsburgh is available at [https://astro.swarthmore.edu/~cohen/videos/Cohen\\_HEAD19\\_zetaPupChandra\\_17mar22.mp4](https://astro.swarthmore.edu/~cohen/videos/Cohen_HEAD19_zetaPupChandra_17mar22.mp4), and the talk abstract is available at <https://submissions.mirasmart.com/HEAD19/itinerary/PresentationDetail.aspx?evdid=51>.

The total emission measure and the mass-loss rate of  $\zeta$ Pup demonstrate strong correlation, which can be partially explained by the parameter degeneracy between  $\Sigma_*$  (quantifying absorption) and norms (quantifying emission), as discussed earlier. Nevertheless, such strong correlation is still exciting, as we can differentiate the effect of emission and absorption. An increase in the overall emission measure, with every norm increasing by the same amount, does not affect the short- and long-wavelength line ratio, although we have argued that the absolute amount of flux increase towards longer wavelengths is higher. But an increase in  $\Sigma_*$  leads to a greater fraction of emission absorbed at longer wavelengths. To see this, we consider the absorption coefficient  $e^{-\tau}$  at a given point in the wind, where  $\tau = \kappa_\lambda \Sigma_* t(r, \mu)$ , and  $t(r, \mu)$  is greater than zero and is coordinate-dependent (see equation 3.9). If  $\Sigma_*$  increases by a factor of  $\alpha$ , then the absorption coefficient increases by a factor of  $e^{-(\alpha-1)\Sigma_* \kappa_\lambda t}$  where  $\alpha > 1$ . And this factor increases as  $\kappa_\lambda$  increases towards longer wavelengths. Thus, an increase in  $\Sigma_*$  will change the short- and long-wavelength line ratio, as opposed to an equal increase in the emission measure at each temperature.

From Figure 3.6, we observe similar DEM shapes in all observations, suggesting that the emission measure at each temperature varies by similar amount. As the line ratios are adequately modeled, we expect a physically meaningful, rather than mathematically trivial, correlation between the total emission and the mass-loss rate: the mass-loss rate is linearly proportional to the wind density by the mass continuity equation, and the emission measure at each temperature by equation 3.4 is proportional to the wind density squared.

We note that the results presented in this chapter are preliminary, and additional modeling and error analysis needs to be done. The next step of this project is to freeze the elemental abundances at their weighted mean values, then fit for and perform error analysis on the

mass-loss rate and the emission measures for each of the 28 *XMM* observations. Careful error analysis can be done by calculating a probability density distribution on each modeled parameter, using the method presented in Section 1.4.3. Putting error bars on the mass-loss rate and the total emission measure in Figure 3.8 will allow us to fit the data points with a linear model, whose slope will either confirm or invalidate their strong correlation.

# 4

## Conclusions

### 4.1 RESULTS

As a general conclusion, we find that we can successfully infer various wind properties from the X-ray data. This thesis uses large data sets, about 3780 ks of total exposure, from cycle 1 and cycle 19 *Chandra* HETGS, as well as 28 *XMM* RGS observations taken over the past 20 years, with many of the later observations not yet having been analyzed or published in the

literature. Exposure times span from 10 to 100 ks, enabling us to examine the temporal and spatial average of the clumping and shock structures in the wind. The results are summarized below.

- (i) We analyze emission line profiles from *Chandra* cycle 19 observations taken during 2018 and 2019 and find the wind mass-loss rate of  $\zeta$ Pup to be  $\dot{M} = 2.47_{-0.09}^{+0.09} \times 10^{-6} M_{\odot} \text{ yr}^{-1}$ , which represents a surprising 40% increase at more than  $4\sigma$  significance compared to the published  $1.76_{-0.12}^{+0.13} \times 10^{-6} M_{\odot} \text{ yr}^{-1}$ , derived from *Chandra* cycle 1 observation in 2000. In deriving the mass-loss rate, we use a newly developed likelihood statistics that, when applied to the cycle 1 observation, indicates a mass-loss rate of  $1.88_{-0.14}^{+0.13} \times 10^{-6} M_{\odot} \text{ yr}^{-1}$  that is within the confidence interval of the published value and significantly lower than the cycle 19 value.
- (ii) We find a 13% emission line flux increase from the *Chandra* cycle 1 and cycle 19 data, accompanying the 40% mass-loss rate increase. The increase is more noticeable at shorter wavelengths that are subject to less wind absorption.
- (iii) We produce a model-independent light curve in the Berghöfer energy band (0.9 – 2 keV) from the 28 *XMM* observations taken from 2000 to 2021, and discover a 19% peak-to-peak flux variation. Linear fit statistics show no increasing or decreasing trend in the light curve, and Kuiper statistics show no year-timescale periodicity. We thus conclude that the flux variation of  $\zeta$ Pup over many years is random.
- (iv) With broadband spectral modeling, we find a 37% peak-to-peak mass-loss rate variation over the *XMM* observations, and find that the mass-loss rate is able to change significantly within several months. The weighted mean mass-loss rate is  $\dot{M} = 2.89 \times 10^{-6} M_{\odot} \text{ yr}^{-1}$ .
- (v) There exists a strong, potentially interesting correlation ( $r = 0.9$ ) between the mass-loss rate and the total emission measure. The peak-to-peak total emission measure variation

is 47%, and neither the total emission measure nor the mass-loss rate show overall increasing or decreasing trend over the past 20 years. In addition, we find essentially no correlation ( $r = 0.13$ ) between the mass-loss rate and the total flux in the Berghöfer energy band, which agrees with our prediction that a high mass-loss rate leads to more emission but also more absorption.

(vi) In terms of temperature distribution and elemental abundances, the wind of  $\zeta$ Pup appears consistent over the 28 *XMM* observations. The differential emission measures (DEM) have similar shapes, and indicate that over 80% of the total emission measure is concentrated between one and five million Kelvins. The weighted mean C, N, O, and Ne abundances are 0.34, 10.71, 0.77, and 2.25 relative to solar, adding up to a super-solar metallicity ( $n_{C+N+O+Ne}/n_H$  is 1.52 relative to solar) in the wind.

## 4.2 DISCUSSION

### 4.2.1 THE VARIABLE MASS-LOSS RATE

The observed significant fluctuation in the mass-loss rate of  $\zeta$ Pup is surprising, as the mass-loss rates of hot-star winds are not expected to change at all. As summarized in Owocki & Cohen (1999), the standard radiation-driven wind theory developed by Castor et al. (1975) predicts the following scaling relation between the mass-loss rate  $\dot{M}$ , the stellar bolometric luminosity  $L_{\text{Bol}}$  (total luminosity across all wavelength), and the effective stellar mass  $M_{\text{eff}} \equiv M_*(1 - \Gamma)$ ,<sup>1</sup>

$$\dot{M} \sim L_{\text{Bol}}^{1/\alpha'} M_{\text{eff}}^{1-1/\alpha'}, \quad (4.1)$$

---

<sup>1</sup>The effective stellar mass, according to its definition, is the fraction of the stellar mass in charge of gravitation. See Section 0.2.1 for a discussion about the Eddington factor,  $\Gamma = F_{\text{rad}}/F_{\text{grav}}$ .

where  $\alpha'$  is a constant<sup>2</sup> that equals 0.57 for O supergiants like  $\zeta$ Pup (Puls et al. 1996). Thus, a 40% increase in the mass-loss rate might indicate an approximate 20% increase in the bolometric luminosity or a change in the parameter  $\alpha'$ . Nevertheless, there exists no published variation in these quantities.

We note however that the bolometric luminosity of  $\zeta$ Pup could change by 20% without being observed. With an effective temperature of around 40,000 K,  $\zeta$ Pup is a blackbody that radiates mainly in the UV band, with a peak at 700 Å. Calculations show that the near-ultraviolet and optical bands (from 3,000 to 17,000 Å) only share around 0.6% of the bolometric radiation. So even if the overall flux increases by around 20%, the absolute amount of flux increase within the observing band of the telescopes (such as the *Hubble Space Telescope* or the *BRITE-Constellation* nanosatellites) that have previously been used to observe  $\zeta$ Pup will be minimal, and could be obscured by instrumental calibrations and noise.

The reasons behind the mass-loss rate fluctuation remain unclear. Several day-timescale periods associated with  $\zeta$ Pup have been identified, among which a 1.78-day period in the optical band is conjectured to be the rotation period of the star (Howarth & Stevens 2014; Nichols et al. 2021). However, such short-timescale, small-amplitude variation will not cause the mass-loss rate to differ at a 40% level (David-Uraz et al. 2017; Sundqvist et al. 2018). Other candidates include surface pulsations or large structures in the co-rotating regions near the base of the wind. The results in this thesis motivate long-term multiwavelength monitoring of changes in the mass-loss rate and the bolometric luminosity, as well as theoretical investigations.

---

<sup>2</sup>As described in Owocki & Cohen (1999),  $\alpha' = \alpha - \delta$  where the two constants  $\alpha$  and  $\delta$  represent the distribution of line opacity and its dependence on ionization level, respectively.

#### 4.2.2 THE CORRELATION BETWEEN MASS-LOSS RATE, EMISSION MEASURE, AND X-RAY FLUX

The tentative strong correlation between the mass-loss rate and the total emission measure is exciting, and aligns well with the simple explanation that the mass-loss rate is proportional to the wind density, and the wind density squared is proportional to the emission measure, assuming that the fraction of the wind shock heated to temperatures high enough to emit X-rays stays relatively constant. But due to the differential absorption across the spectrum, the observed X-ray flux has a much smaller and wavelength-dependent correlation with the mass-loss rate, which is perhaps too weak to be detected.

While comparing the two mass-loss rate results derived independently in Chapters 1 and 3, we note that the emission line diagnostic leads to a lower value than the broadband modeling, with a 16% disagreement. This disagreement is amplified when we realize our use of the solar opacity model in the emission line profile diagnostic: a more realistic opacity model is evidently super-solar, which will lead to an even smaller mass-loss rate. The different systematic errors in our two diagnostics may lead to the disparity in the mass-loss rate. Once we re-perform the broadband modeling of the *XMM* RGS spectra with frozen elemental abundances to constrain the uncertainties on the mass-loss rates, we can determine the level of disparity.

Although  $\zeta$  Pup is the only subject of this thesis, the models and statistical analyses described can be applied to other O and early B supergiants with radiation-driven winds to examine their wind properties, and especially to see if their mass-loss rates show variations on years timescales.

# References

- Asplund, M., Grevesse, N., Sauval, A. J., & Scott, P. (2009). The Chemical Composition of the Sun. *ARA&A*, 47(1), 481–522.
- Baade, D. (1991). Regular Variability of Optical Lines in  $\zeta$  Pup. In *European Southern Observatory Conference and Workshop Proceedings*, volume 36 of *European Southern Observatory Conference and Workshop Proceedings* (pp. 21).
- Beiersdorfer, P., Hell, N., & Lepson, J. K. (2018). Temperature Measurements Using the Dielectronic Satellite Lines of Fe XVII. *ApJ*, 864(1), 24.
- Berghoefer, T. W., Baade, D., Schmitt, J. H. M. M., Kudritzki, R. P., Puls, J., Hillier, D. J., & Pauldrach, A. W. A. (1996). Correlated variability in the X-ray and H $\alpha$  emission from the O4If supergiant  $\zeta$  Puppis. *A&A*, 306, 899.
- Blomme, R., van de Steene, G. C., Prinja, R. K., Runacres, M. C., & Clark, J. S. (2003). Radio and submillimetre observations of wind structure in zeta Puppis. *A&A*, 408, 715–727.
- Brown, G. V., Beiersdorfer, P., Chen, H., Scofield, J. H., Boyce, K. R., Kelley, R. L., Kilbourne, C. A., Porter, F. S., Gu, M. F., Kahn, S. M., & Szymkowiak, A. E. (2006). Energy-Dependent Excitation Cross Section Measurements of the Diagnostic Lines of Fe XVII. *Phys. Rev. Lett.*, 96(25), 253201.
- Canizares, C. R., Davis, J. E., Dewey, D., Flanagan, K. A., Galton, E. B., Huenemoerder, D. P., Ishibashi, K., Markert, T. H., Marshall, H. L., McGuirk, M., Schattenburg, M. L., Schulz, N. S., Smith, H. I., & Wise, M. (2005). The Chandra High-Energy Transmission Grating: Design, Fabrication, Ground Calibration, and 5 Years in Flight. *PASP*, 117(836), 1144–1171.
- Cash, W. (1979). Parameter estimation in astronomy through application of the likelihood ratio. *ApJ*, 228, 939–947.

- Cassinelli, J. P., Miller, N. A., Waldron, W. L., MacFarlane, J. J., & Cohen, D. H. (2001). Chandra Detection of Doppler-shifted X-Ray Line Profiles from the Wind of  $\zeta$ Puppis (O<sub>4</sub>F). *ApJ*, 554(1), L55–L58.
- Castor, J. I., Abbott, D. C., & Klein, R. I. (1975). Radiation-driven winds in Of stars. *ApJ*, 195, 157–174.
- Churazov, E., Gilfanov, M., Forman, W., & Jones, C. (1996). Mapping the Gas Temperature Distribution in Extended X-Ray Sources and Spectral Analysis in the Case of Low Statistics: Application to ASCA Observations of Clusters of Galaxies. *ApJ*, 471, 673.
- Cohen, D. H., Gagné, M., Leutenegger, M. A., MacArthur, J. P., Wollman, E. E., Sundqvist, J. O., Fullerton, A. W., & Owocki, S. P. (2011). Chandra X-ray spectroscopy of the very early O supergiant HD 93129A: constraints on wind shocks and the mass-loss rate. *MNRAS*, 415(4), 3354–3364.
- Cohen, D. H., Leutenegger, M. A., Wollman, E. E., Zsargó, J., Hillier, D. J., Townsend, R. H. D., & Owocki, S. P. (2010). A mass-loss rate determination for  $\zeta$ Puppis from the quantitative analysis of X-ray emission-line profiles. *MNRAS*, 405(4), 2391–2405.
- Cohen, D. H., Parts, W., Doskoch, G. M., Wang, J., Petit, V., Leutenegger, M. A., & Gagné, M. (2021). Chandra grating spectroscopy of embedded wind shock X-ray emission from O stars shows low plasma temperatures and significant wind absorption. *MNRAS*, 503(1), 715–725.
- Cohen, D. H., Wang, J., Petit, V., Leutenegger, M. A., Dakir, L., Mayhue, C., & David-Uraz, A. (2020). Chandra spectral measurements of the O supergiant  $\zeta$ Puppis indicate a surprising increase in the wind mass-loss rate over 18 yr. *MNRAS*, 499(4), 6044–6052.
- Cohen, D. H., Wollman, E. E., Leutenegger, M. A., Sundqvist, J. O., Fullerton, A. W., Zsargó, J., & Owocki, S. P. (2014). Measuring mass-loss rates and constraining shock physics using X-ray line profiles of O stars from the Chandra archive. *MNRAS*, 439(1), 908–923.
- David-Uraz, A., Owocki, S. P., Wade, G. A., Sundqvist, J. O., & Kee, N. D. (2017). Investigating the origin of cyclical wind variability in hot massive stars - II. Hydrodynamical simulations of corotating interaction regions using realistic spot parameters for the O giant  $\xi$  Persei. *MNRAS*, 470(3), 3672–3684.
- den Herder, J. W., Brinkman, A. C., Kahn, S. M., Branduardi-Raymont, G., Thomsen, K., Aarts, H., Audard, M., Bixler, J. V., den Boggende, A. J., Cottam, J., Decker, T., Dubbel-dam, L., Erd, C., Goulooze, H., Güdel, M., Guttridge, P., Hailey, C. J., Janabi, K. A., Kaas-tra, J. S., de Korte, P. A. J., van Leeuwen, B. J., Mauche, C., McCalden, A. J., Mewe, R.,

- Naber, A., Paerels, F. B., Peterson, J. R., Rasmussen, A. P., Rees, K., Sakelliou, I., Sako, M., Spodek, J., Stern, M., Tamura, T., Tandy, J., de Vries, C. P., Welch, S., & Zehnder, A. (2001). The Reflection Grating Spectrometer on board XMM-Newton. *A&A*, *365*, L7–L17.
- Dessart, L. & Owocki, S. P. (2005). 2D simulations of the line-driven instability in hot-star winds. II. Approximations for the 2D radiation force. *A&A*, *437*(2), 657–666.
- Dorman, B. & Arnaud, K. A. (2001). Redesign and Reimplementation of XSPEC. In J. Harnden, F. R., F. A. Primini, & H. E. Payne (Eds.), *Astronomical Data Analysis Software and Systems X*, volume 238 of *Astronomical Society of the Pacific Conference Series* (pp. 415).
- Eversberg, T., Lépine, S., & Moffat, A. F. J. (1998). Outmoving Clumps in the Wind of the Hot O Supergiant  $\zeta$  Puppis. *ApJ*, *494*(2), 799–805.
- Feldmeier, A., Puls, J., & Pauldrach, A. W. A. (1997). A possible origin for X-rays from O stars. *A&A*, *322*, 878–895.
- Foster, A. R., Ji, L., Smith, R. K., & Brickhouse, N. S. (2012). Updated Atomic Data and Calculations for X-Ray Spectroscopy. *ApJ*, *756*(2), 128.
- Fruscione, A., Hawkins, I., Jelinsky, P., & Wercigroch, A. (1994). The Distribution of Neutral Hydrogen in the Interstellar Medium. I. The Data. *ApJS*, *94*, 127.
- Harnden, F. R., J., Branduardi, G., Elvis, M., Gorenstein, P., Grindlay, J., Pye, J. P., Rosner, R., Topka, K., & Vaiana, G. S. (1979). Discovery of an X-ray star association in VI Cygni (Cyg OB2). *ApJ*, *234*, L51–L54.
- Harries, T. J. & Howarth, I. D. (1996). Linear spectropolarimetry of the H $\alpha$  emission line of  $\zeta$  Puppis. *A&A*, *310*, 533–546.
- Howarth, I. D., Prinja, R. K., & Massa, D. (1995). The IUE MEGA Campaign: The Rotationally Modulated Wind of zeta Puppis. *ApJ*, *452*, L65.
- Howarth, I. D. & Stevens, I. R. (2014). Time-series photometry of the O4 I(n)fp star  $\zeta$  Puppis. *MNRAS*, *445*(3), 2878–2883.
- Howarth, I. D. & van Leeuwen, F. (2019). The distance, rotation, and physical parameters of  $\zeta$  Pup. *MNRAS*, *484*(4), 5350–5361.
- Kahn, S. M., Leutenegger, M. A., Cottam, J., Rauw, G., Vreux, J. M., den Boggende, A. J. F., Mewe, R., & Güdel, M. (2001). High resolution X-ray spectroscopy of zeta Puppis with the XMM-Newton reflection grating spectrometer. *A&A*, *365*, L312–L317.

Lamers, H. J. G. L. M. & Cassinelli, J. P. (1999). *Introduction to Stellar Winds*. Cambridge University Press.

Leutenegger, M. A., Cohen, D. H., Sundqvist, J. O., & Owocki, S. P. (2013). Constraints on Porosity and Mass Loss in O-star Winds from the Modeling of X-Ray Emission Line Profile Shapes. *ApJ*, 770(1), 80.

Leutenegger, M. A., Cohen, D. H., Zsargó, J., Martell, E. M., MacArthur, J. P., Owocki, S. P., Gagné, M., & Hillier, D. J. (2010). Modeling Broadband X-ray Absorption of Massive Star Winds. *ApJ*, 719(2), 1767–1774.

Lucy, L. B. & White, R. L. (1980). X-ray emission from the winds of hot stars. *ApJ*, 241, 300–305.

Macfarlane, J. J., Cohen, D. H., & Wang, P. (1994). X-Ray-induced Ionization in the Winds of Near-Main-Sequence O and B Stars. *ApJ*, 437, 351.

Marshall, H. L., Tennant, A., Grant, C. E., Hitchcock, A. P., O'Dell, S. L., & Plucinsky, P. P. (2004). Composition of the Chandra ACIS contaminant. In K. A. Flanagan & O. H. W. Siegmund (Eds.), *X-Ray and Gamma-Ray Instrumentation for Astronomy XIII*, volume 5165 of *Society of Photo-Optical Instrumentation Engineers (SPIE) Conference Series* (pp. 497–508).

Martins, F., Hervé, A., Bouret, J. C., Marcolino, W., Wade, G. A., Neiner, C., Alecian, E., Grunhut, J., & Petit, V. (2015). The MiMeS survey of magnetism in massive stars: CNO surface abundances of Galactic O stars. *A&A*, 575, A34.

Najarro, F., Hanson, M. M., & Puls, J. (2011). L-band spectroscopy of Galactic OB-stars. *A&A*, 535, A32.

Nazé, Y., Oskinova, L. M., & Gosset, E. (2013). A Detailed X-Ray Investigation of  $\zeta$  Puppis. II. The Variability on Short and Long Timescales. *ApJ*, 763(2), 143.

Nazé, Y., Ramiaramanantsoa, T., Stevens, I. R., Howarth, I. D., & Moffat, A. F. J. (2018). A detailed X-ray investigation of  $\zeta$  Puppis. IV. Further characterization of the variability. *A&A*, 609, A81.

Nichols, J. S., Nazé, Y., Huenemoerder, D. P., Moffat, A. F. J., Miller, N. A., Lauer, J., Ignace, R., Gayley, K., Ramiaramanantsoa, T., Oskinova, L., Hamann, W.-R., Richardson, N. D., Waldron, W. L., & Dahmer, M. (2021). Correlated X-Ray and Optical Variability in the O-type Supergiant  $\zeta$  Puppis. *ApJ*, 906(2), 89.

- Owocki, S. P., Castor, J. I., & Rybicki, G. B. (1988). Time-dependent Models of Radiatively Driven Stellar Winds. I. Nonlinear Evolution of Instabilities for a Pure Absorption Model. *ApJ*, 335, 914.
- Owocki, S. P. & Cohen, D. H. (1999). A Simple Scaling Analysis of X-Ray Emission and Absorption in Hot-Star Winds. *ApJ*, 520(2), 833–840.
- Owocki, S. P. & Cohen, D. H. (2001). X-Ray Line Profiles from Parameterized Emission within an Accelerating Stellar Wind. *ApJ*, 559(2), 1108–1116.
- Paltani, S. (2004). Searching for periods in X-ray observations using Kuiper's test. Application to the ROSAT PSPC archive. *A&A*, 420, 789–797.
- Porquet, D., Dubau, J., & Grosso, N. (2010). He-like Ions as Practical Astrophysical Plasma Diagnostics: From Stellar Coronae to Active Galactic Nuclei. *Space Sci. Rev.*, 157(1-4), 103–134.
- Prinja, R. K. & Howarth, I. D. (1986). Narrow Absorption Components and Variability in Ultraviolet P Cygni Profiles of Early-Type Stars. *ApJS*, 61, 357.
- Puls, J., Kudritzki, R. P., Herrero, A., Pauldrach, A. W. A., Haser, S. M., Lennon, D. J., Gabler, R., Voels, S. A., Vilchez, J. M., Wachter, S., & Feldmeier, A. (1996). O-star mass-loss and wind momentum rates in the Galaxy and the Magellanic Clouds Observations and theoretical predictions. *A&A*, 305, 171.
- Puls, J., Markova, N., Scuderi, S., Stanghellini, C., Taranova, O. G., Burnley, A. W., & Howarth, I. D. (2006). Bright OB stars in the Galaxy. III. Constraints on the radial stratification of the clumping factor in hot star winds from a combined  $H_{\alpha}$ , IR and radio analysis. *A&A*, 454(2), 625–651.
- Reid, A. H. N. & Howarth, I. D. (1996). Optical time-series spectroscopy of the O4 supergiant  $\zeta$  Puppis. *A&A*, 311, 616–630.
- Runacres, M. C. & Owocki, S. P. (2002). The outer evolution of instability-generated structure in radiatively driven stellar winds. *A&A*, 381, 1015–1025.
- Sota, A., Maíz Apellániz, J., Morrell, N. I., Barbá, R. H., Walborn, N. R., Gamen, R. C., Arias, J. I., & Alfaro, E. J. (2014). The Galactic O-Star Spectroscopic Survey (GOSSS). II. Bright Southern Stars. *ApJS*, 211(1), 10.
- Stevens, I. R., Blondin, J. M., & Pollock, A. M. T. (1992). Colliding Winds from Early-Type Stars in Binary Systems. *ApJ*, 386, 265.

Sundqvist, J. O., Owocki, S. P., & Puls, J. (2018). 2D wind clumping in hot, massive stars from hydrodynamical line-driven instability simulations using a pseudo-planar approach. *A&A*, 611, A17.

ud-Doula, A. & Owocki, S. P. (2002). Dynamical Simulations of Magnetically Channeled Line-driven Stellar Winds. I. Isothermal, Nonrotating, Radially Driven Flow. *ApJ*, 576(1), 413–428.

van Leeuwen, F. (2007). Validation of the new Hipparcos reduction. *A&A*, 474(2), 653–664.

Walborn, N. R., Nichols, J. S., & Waldron, W. L. (2009). The Correlation Between X-Ray Line Ionization and Optical Spectral Types of the OB Stars. *ApJ*, 703(1), 633–641.

Wilms, J., Allen, A., & McCray, R. (2000). On the Absorption of X-Rays in the Interstellar Medium. *ApJ*, 542(2), 914–924.